UNIVERSITY OF SOUTHAMPTON

FACULTY OF ENGINEERING, SCIENCE & MATHEMATICS

School of Engineering Sciences

Quench Propagation in Conduction Cooled HTS Pancake Coils

by

Adam Paul Johnstone

Thesis for the degree of Doctor of Philosophy

June 2005

UNIVERSITY OF SOUTHAMPTON

ABSTRACT

FACULTY OF ENGINEERING, SCIENCE & MATHEMATICS

SCHOOL OF ENGINEERING SCIENCES

Doctor of Philosophy

QUENCH PROPAGATION IN CONDUCTION COOLED HTS PANCAKE COILS

By Adam Paul Johnstone

The formation and propagation of normal zones in a conduction cooled (BiPb)2223 Ag alloy sheathed pancake coil has been investigated both experimentally and through simulation. To provide stable operating conditions for the coils a conduction cooling system, incorporating a single stage cryocooler, and current leads were designed and manufactured. The apparatus was tested up to a maximum operating current of 300A at which only a 0.7K drift in the coldhead temperature was observed. A minimum operating temperature at the coil boundaries of 35K was achieved.

Highly instrumented pancake coils were wound with a (BiPb)2223 tape conductor. The current-voltage characteristics were measured and the response to a steady overcurrent observed. The quench energy was measured as a function of operating temperature by applying transient disturbances of varying sizes to the coil. A similar dependence of the quench energy on operating temperature was obtained from a simplified finite element model.

A method of determining the temperature profile of a minimum propagating zone was proposed. The size and shape of the MPZ was measured as a function of operating temperature. It was observed that the shape of the temperature profiles was significantly affected by the operating temperature. The normal zone propagation velocity was determined as a function of operating temperature by examining the propagating temperature profiles. The results obtained will be of use to the magnet designer when determining the stability of coils at various operating temperature and when designing protection systems for HTS magnets.

Contents

List of Figures

Chapter 1:

Chapter 2:

Chapter 3:

Chapter 4:

Chapter 5:

Chapter 6:

List of Tables

List of Equations

Acknowledgements

I am greatly indebted to the staff and students with whom I have worked closely for ensuring the time spent during my studies was enjoyable. Thanks must go to Carlo Beduz and Yifeng Yang for their guidance and encouragement during the course of my studies. Also the technical help provided by Mike Webb and Iain Mears when machining and assembly parts of the apparatus was invaluable. I would like to thank the University of Southampton and the Institute of Physics for grants that enabled me to attend the 20th International Cryogenic Engineering Conference. Finally, thanks to my family for putting up with me and Orlanda for tea and cakes.

Chapter 1 : Fundamentals and applications of superconductivity

1.1 Introduction and historical overview

The field of superconductivity was initiated in 1911 when H. Kamerlingh Onnes discovered that the electrical resistance of Mercury dropped to zero below 4.15K [1]. This perfect conductivity is the first distinguishing characteristic of a superconductor [2]. The second distinguishing characteristic was identified in 1933 when Meissner and Ochsenfeld found that if a superconducting sphere is cooled below its transition temperature in a magnetic field it will exclude magnetic flux from its interior [3]. It was the realisation that superconductivity was destroyed when low fields were applied that meant the technological applications of superconductivity, such as high field electromagnets, could not be exploited. It was the many years of work on superconductors during the 1950's by Hulm, Matthias and their co-workers that led to the discovery of magnet grade superconductors such as Nb_3Sn and NbTi. These materials operate near to the temperature of liquid Helium and are therefore known as low temperature superconductors (LTS). Nb_3Sn and NbTi become superconducting when cooled below 18.3K and 9.2K respectively [4].

The development of superconductors with high critical fields meant that high-field magnets could be constructed. Magnets manufactured from the early conductors were found to fail due to instabilities that resulted in a catastrophic loss of field known as a quench. Due to years of research LTS magnets are now designed firstly to prevent a quench from initiating, and secondly to quench safely if a quench occurs. LTS have been in use in high field electromagnet applications for the past 30 years [4]. Nuclear magnetic resonance (NMR, magnetic resonance imaging (MRI) and fusion research are examples of only some of the fields in which LTS are utilised. However, LTS devices are cooled by liquid helium and therefore they require careful thermal design and construction as well as the need for expensive infrastructure in place to provide the coolant.

In 1986 Bednorz and Muller reported superconductivity in La-Ba-Cu-O at 30K [5], this was followed by the discovery of superconductivity at 93K in the Y-Ba-Cu-O compound

system by Wu, Ashburn and Torng [6]. These discoveries sparked off the development of the ceramic oxide superconductors which, because of their high critical temperatures, could be cooled with cheap and readily available liquid nitrogen. The development of oxide superconductors brought about the discovery of superconductivity below 110K in the Bi-Sr-Ca-Cu-O system by Maeda and co-workers at the Tsukuba laboratories in Japan [7]. Continued development of the high temperature superconductors (HTS) over the past 15 years has lead to the production of prototype HTS devices as discussed in section 1.4.

1.2 Superconductor fundamentals

1.2.1 Critical surface

A superconductor is a material that exhibits two characteristic properties, zero electrical resistance and perfect diamagnetism [2] below a critical transition temperature (T_C). In addition to T_C [K], the critical field H_C [T] and critical current density J_C [A.m^{-2}] are two other parameters that define a critical surface below which the superconducting phase can exist [4]. The abrupt change from normal conduction to the superconducting state occurs at a thermodynamic phase transition.

1.2.2 Perfect diamagnetism

There are two aspects to perfect diamagnetism in superconductors. These are flux exclusion and flux expulsion. When a superconductor is cooled in zero magnetic field to below T_C and a magnetic field is applied the field will be excluded from the material. Flux expulsion occurs when a superconductor is cooled in a magnetic field. The field will be expelled from the material at temperatures below T_C, a phenomenon known as the Meissner effect.

1.2.3 Type I and II superconductivity

Type I superconductors, such as Mercury and Lead, were the first superconductors to be discovered. The critical field (H_C) of the Type I superconductors is very low, typically less than 0.2T. This limitation means that Type I superconductors cannot be used in high field magnet applications. Type II superconductors are usually alloys or compounds [8] and can remain superconducting up to fields in excess of 10T. This means they can be used in high

field magnet applications. The effect of an external field on the internal field in a type I and type II bulk superconductor is shown in Figure 1.1 [9].

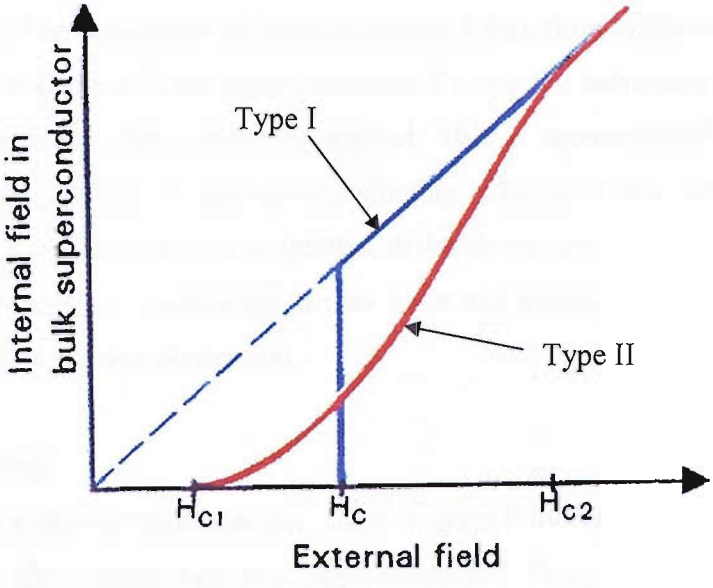

Figure 1.1: Magnetization of Type I and Type II superconductors

Up to a certain critical field, H_{C1} [T], type I and type II superconductors behave alike, they both exhibit perfect diamagnetism. At magnetic fields above H_{C1} type II superconductors are able to admit flux while still remaining in the superconducting state. This is accomplished by confining the field to an internal array of normal state flux tubes known as vortices [8]. In a homogeneous crystal these vortices are arranged in a triangular lattice known as a Abrikosov lattice after Alexei Abrikosov [10] who first proposed the theory. As the applied magnetic field increases, the density of the vortices increases and they begin to overlap [2]. At the upper critical field H_{C2} [T], the normal cores overlap completely and the specimen becomes entirely normal [11]. When the superconductor is subjected to fields between H_{C1} and H_{C2} it is said to be in the mixed state.

1.2.4 Pinning and flux flow

If a transport current is applied to a superconductor the interaction between the transport current density, J [A.m^{-2}], and magnetic field confined in the vortices, B [T], produces a

Lorentz force per unit volume, F_L [N.m^{-3}], which acts on the vortices. The Lorentz force per unit volume is calculated as shown in Equation 1.1.

$$\underline{F_L} = \underline{J} \times \underline{B} \quad [N.m^{-3}] \qquad \textbf{Equation 1.1}$$

Very small currents will cause the vortices to move because they are only retarded by viscous damping. The movement of vortices causes a flux flow resistance to be developed that causes heat dissipation in the superconductor. To stop the movement of vortices a force equivalent to the lorentz force must be applied. This is accomplished by "pinning" the vortices to inhomogeneities in the superconducting material. These inhomogeneities can take the form of grain boundaries, precipitates, dislocations, and defects caused by radiation [12]. At a certain transport current the lorentz force will exceed the pinning force and flux flow will occur thus causing dissipation.

1.2.5 Flux jumping

Flux jumping is a phenomenon that can cause a quench due the interaction between flux motion and the temperature rise in a superconductor. Flux motion generates heat that subsequently causes a temperature rise therefore resulting in further flux motion. This cycle tends to reinforce itself leading to an unbounded temperature increase and resulting in a quench. Flux jumping can be eliminated by reducing the size of the superconductor below a critical value. In practice this means finely dividing the superconductor into a multi-filamentary conductor. When this is done the superconducting filaments must be twisted to decouple them so that the critical size is not exceeded.

1.2.6 Critical state model

The situation where pinning is strong enough to prevent any substantial vortex motion will be considered. Motion of individual vortices is largely prevented by their mutual repulsion and as a result flux tends to move in "bundles" when the lorentz force exceeds the pinning force [13]. It is therefore appropriate to adopt a more macroscopic view of the superconductor. Bean [14] proposed a model in which a hard superconductor is capable of sustaining lossless macroscopic current up to a critical current density, J_C. All regions of the superconductor are either carrying their critical current or zero current and therefore it can be said that the superconductor is in the "critical state". The Bean critical state model

assumes J_C to be independent of field although J_C decreases with field in real superconductors. Figure 1.2 shows a virgin slab of hard superconductor subject to an applied field. Although it has been proven that the magnetic flux enters the superconductor in normal state flux tubes it is convenient to visualise the magnetic flux penetration into the slab as a succession of lamina as proposed by Goodman [15]. As the field is increased screening currents will flow at the surface of the superconductor with $J>J_C$. The screening current will decay resistively and the field will penetrate the interior of the superconductor until $J=J_C$. The field profiles shown in Figure 1.2 are produced by applying an external field to a thin slab of width D [m]. The magnetic field is increased from zero, to the penetration field H^* [T] and then to a value twice the penetration field [14]. It can be seen that the J_C distribution does not change when the slab is fully penetrated.

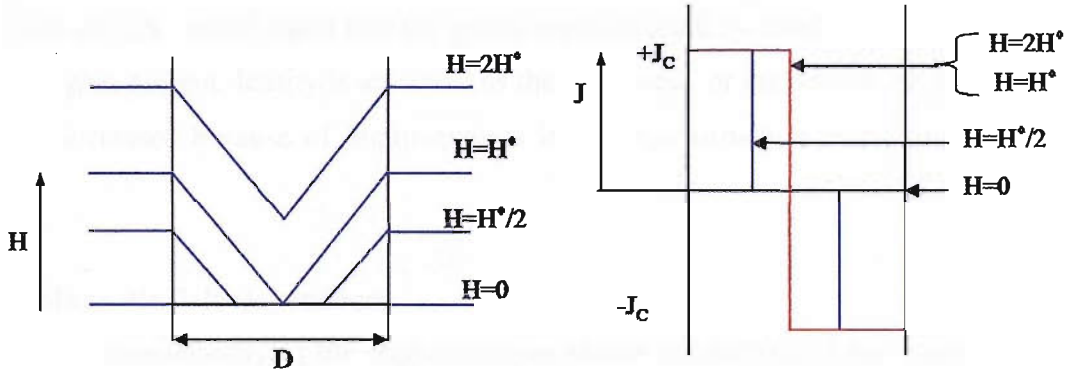

Figure 1.2: The Bean critical state model

1.3 BSCCO superconductors

1.3.1 Structure

The BSCCO superconductors are highly anisotropic materials consisting of copper-oxygen planes separated by intermediate layers containing Bismuth, Strontium and Calcium. The anisotropic structure affects both the microscopic and macroscopic properties of the material. Supercurrents flow relatively freely within the separated copper-oxygen planes but with difficulty perpendicular to them [16]. The BSCCO superconductors have a pronounced grain growth anisotropy leading to plate-like grains with a large aspect ratio.

The dimensions perpendicular to the copper-oxygen planes (c-axis) are typically a few micrometers and the dimensions parallel to the copper-oxygen planes (a-b axis) are typically tens of micrometers [17].

1.3.2 Current flow

Boundaries between the plate-like grains present barriers to the passage of current and act as weak links. Weak link behaviour is a term used to describe what happens to a supercurrent as it crosses a non-superconductor region [16]. The ability of the (BiPb)2223 system to form grain boundaries with a relatively high current carrying capacity allows long length conductors to be produced starting with powder metallurgical methods [17]. Various theories of how the current flows through a BSCCO superconductor have been proposed [18,19]. In all theories the current percolates through the granular structure. The 'railway switch' model states that the grains are connected by small angle grain boundaries [19]. Higher current density is achieved as the alignment, or texture, of the grains in the c-axis is increased because of improvements in the microstructure at the grain boundaries [17].

1.3.3 Magnetic field dependence

The two-dimensionality of the copper-oxygen planes in (BiPb)2223 has a profound effect on flux pinning and hence the effect of magnetic field on the superconductor. When field is applied perpendicular to the copper-oxygen planes, the lorentz force is parallel to the planes where there is very little restraint for vortex motion; dissipation therefore occurs at relatively low currents. Field applied parallel to the copper-oxygen planes produces a lorentz force perpendicular to the planes where it is more difficult for the vortices to move and therefore dissipation occurs at higher currents. The situation in real tapes is more complex because the grains in the tape are not perfectly aligned with the tape axis; due to the grain misalignment a field applied parallel to the tape surface will generate a field component perpendicular to the copper-oxygen planes. Consequently, if (BiPb)2223 tapes are poorly textured the critical current will be severely affected by fields applied parallel to the tape surface. An example of the how the transport current of a (BiPb)2223 tape is affected by the magnitude and direction of the applied field is shown below in Figure 1.3.

As Hensel reported [19], the measured field dependence normal to the tape surface (B//c [T]) is characteristic of the material, while the field dependence parallel to the tape surface (B//ab [T]) is determined by the microstructure of each sample.

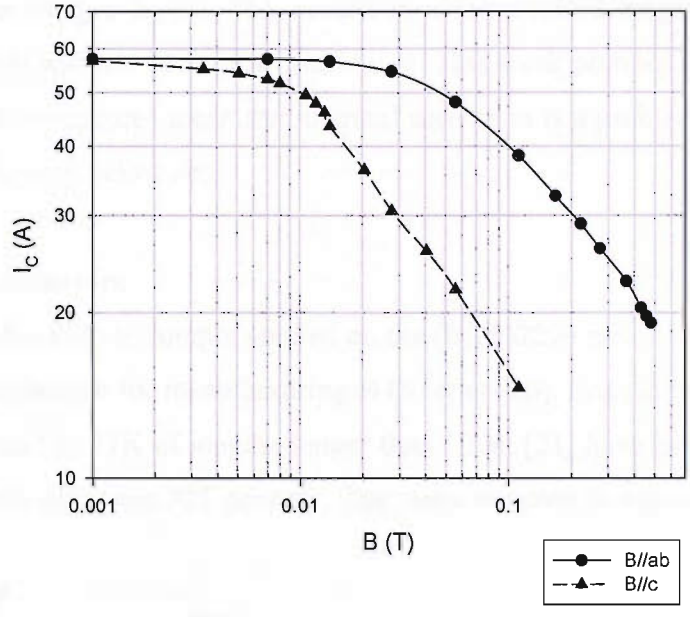

Figure 1.3: Dependence of the transport current on the magnitude and direction of the applied field on a Ag alloy sheathed (BiPb)2223 tape at 77K

1.3.4 Thermal activation

At finite temperatures thermal energy may allow vortices and bundles of vortices to jump from one pinning point to another in response to the driving force of the flux-density gradient. Vortices hop from one pinning site to another, and in some cases this can occur at a measurable rate [13]. This effect is known as flux creep. If flux is trapped in a hollow cylinder, or in a superconducting solenoid in the persistent current mode, there may be an observable decrease of this trapped field with time [13]. The low operating temperature and high pinning in LTS means that the effect of thermal activation is low. The field at which the flux vortices are no longer pinned at a certain temperature is known as the irreversibility field, H_{irr} [T]. For LTS because the effect of thermal activation is low H_{irr} is almost the same as H_{C2}. In HTS the effect of thermal activation is much greater which leads to easier flux line motion at fields below H_{C2} [16]. Above H_{irr}, J_C is zero or very small.

The flux creep model may not be applicable to HTS because of the way in which the vortices form in these anisotropic superconductors. The vortices are similar to stacks of pancakes and thermal motion can shake the stacked pancake vortices and decouple vortices in adjacent copper-oxygen layers. This results in a complicated magnetic phase diagram, the details of which will not be further considered. This weak pinning along with generally higher operating temperatures mean that thermal activation is a problem in HTS leading to dissipation significantly below *Jc*.

1.3.5 Practical conductors

The powder-in-tube (PIT) technique applied on the (BiPb)2223 material has been by far the most successful technique for manufacturing HTS tapes [20]. Engineering current densities exceeding 15kA.cm^{-2} at 77K of lengths longer than 100m [21] have been demonstrated for tapes manufactured using the PIT process. The steps required to manufacture (BiPb)2223

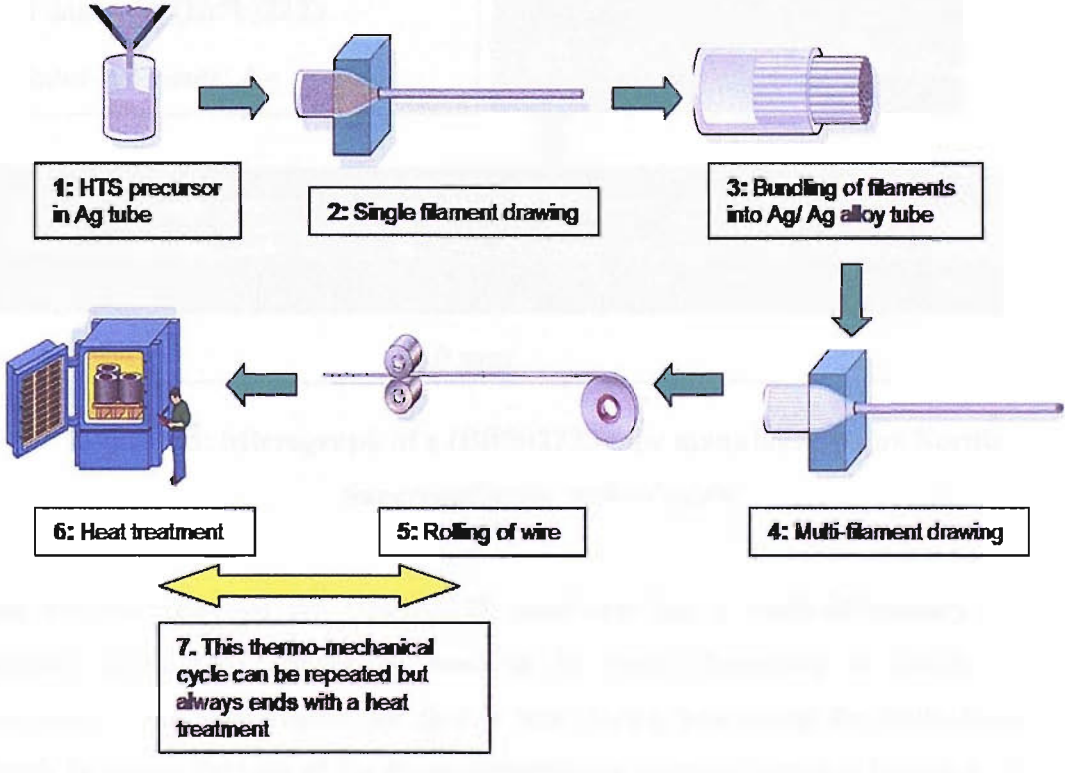

Figure 1.4: Manufacture of multi-filamentary (BiPb)2223 tapes [20,21]. Graphic is copyright of American Superconductor Corporation.

multi-filamentary tapes are demonstrated in Figure 1.4. The details of the manufacturing process will differ between individual manufacturers depending on how their individual conductors are optimised.

A micrograph of the 'Zerome Hercules' (BiPb)2223 conductor produced by Nordic Superconductor Technologies (NST) is shown in Figure 1.5. Ag and Ag alloys are used as sheath materials because Ag does not react with the precursor material and it allows oxygen release through the sheath during heat treatment. The low resistivity and high thermal conductivity of the Ag sheath also improves the thermal stability of the conductor. A 0.1MgNi-Ag alloy is used for the outer sheath due to its superior mechanical properties over pure Ag. In applications where good mechanical properties are essential the tape conductor can be laminated with stainless steel.

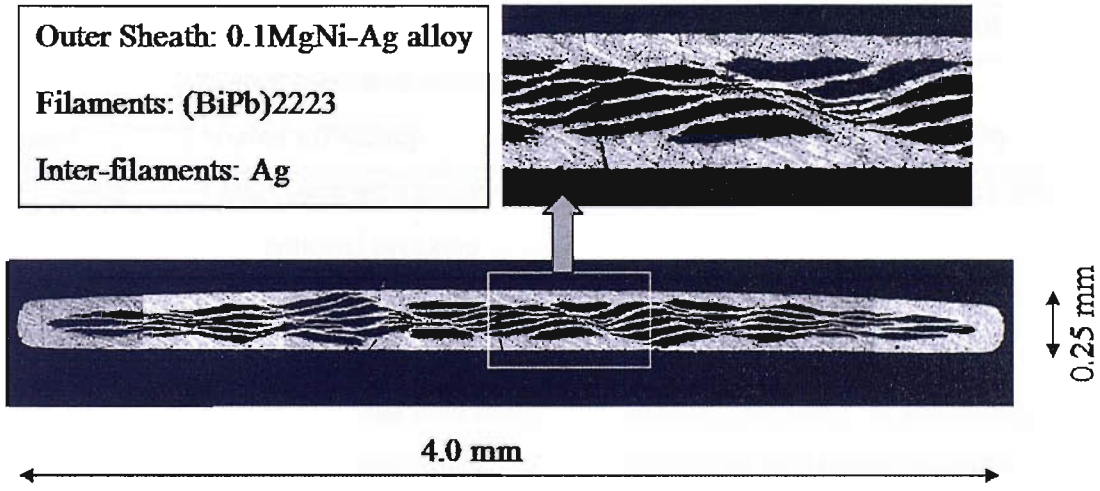

Figure 1.5: Micrograph of a (BiPb)2223 tape manufactured by Nordic Superconductor technologies

It can be observed that the (BiPb)2223 conductor has a multi-filamentary structure. Practically (BiPb)2223 conductors need to be multi-filamentary to obtain the best performance. One such reason for this is that during processing the multi-filamentary structure increases the area of the Ag-superconductor interface which is known to improve texture and phase development of the 2223 superconducting phase [22,23]. Additional

benefits arising from the multi-filamentary structure include improved heat transfer from the individual filaments resulting in an increase the thermal stability of the conductor. The mechanical properties of the conductor are also enhanced because bending induced cracking at the surface of the tape does not spread to the whole tape, but is kept within the outer filaments [20, 24].

1.4 HTS applications

Table 1.1 summarises some of the applications of HTS technology and the benefits over existing technology. Examples and details of developed devices for each application are presented. The application and examples list is in no way exhaustive, there are many other companies and university laboratories that have produced working HTS devices.

Application	Benefits	Developer and details
Motors/ generator	Lower mass and volume Higher efficiency	American Superconductor Corporation [21]; 5MW/230rpm
Fault Current Limiters (FCL)	Faster switching times than conventional breakers	Siemens [25]; 1MVA YBCO film
NMR insert coils	Extends field strength beyond that produced by Nb_3Sn	OST*/ NHFML**; Bi(2212) tape adds 5T to 20T background field [26]
Current leads	Lower heat leak than non-superconducting leads	Pirelli/ University of Southampton 600A-13kA, (BiPb)2223 tapes [27]
Transmission cables	Higher transmission capacity	InnoPower [28]; 30m, 35kV, 2kA

*Oxford Instruments Superconducting Technology

**National High Field Magnet Laboratory

Table 1.1: HTS applications

1.5 Material properties

Superconducting coils are operated at temperatures at which the properties of the materials that constitute the coils are strongly affected by temperature. The stability and protection theories are dependent on knowledge of the coil material properties. A thorough understanding of the variation of the material properties with temperature, especially the stabilising sheath, is therefore essential.

1.5.1 Specific heat

Most of the thermal energy of a solid is associated with the vibrations of the atoms. This is known as the phonon or lattice specific heat. In metals that are electrical conductors the free electrons also contribute to the specific heat. At room temperature the electron specific heat is only around 1% of the lattice specific heat [29]. At low temperatures the electron contribution becomes important because it varies linearly with temperature where as the phonon contribution varies with the cube of temperature. The reduced values of specific heat at low temperatures mean that even very small additions of energy to a material can produce a large temperature rise. This is one of the underlying reasons for the poor stability of LTS. Specific heat is defined as the energy required to raise the temperature of a unit mass by 1K, given in SI units by J $kg^{-1}K^{-1}$. Heat capacity is defined as the energy required to raise the temperature of a body by 1K, given in SI units by J K^{-1}.

1.5.2 Electrical and thermal conductivity

In metals both heat and charge is mainly transported by the conduction electrons [30]. Phonon conduction is suppressed because the phonons are scattered by the large number of free electrons.

Thermal conductivity

The thermal conductivity due to the electron contribution is made up of two parts, the thermal conductivity due to the scattering of electrons by impurities and dislocations, and the scattering of electrons by phonons. The balance between the scattering by impurities/dislocations and scattering by phonons gives an optimum thermal conductivity

that occurs at around 20-40K [29]. The thermal conductivity is sensitive to impurities in the metal lattice and to mechanical deformation that will produce dislocations in the metal lattice. In alloys the presence of even 1% impurity atoms can decrease the electron mean free path, by a factor of 10 or more, below the value of the relatively pure metal [31]. The effect of the increased impurity scattering is a flattening of the peak in thermal conductivity. Care must also be taken not to produce dislocations in the metal during manufacturing operations.

Resistivity

Matthiessen's rule states that the electrical resistivity of a metal, ρ [Ω.m], can be considered as the sum of the resistivities due to the lattice contribution, ρ_L, and contribution from the impurities and dislocations, ρ_i, [17] as shown in Equation 2.1. ρ_L is dependent on temperature where as ρ_i is a constant depending on the level of impurity or degree of work hardening. Below approximately 20K the electrical resistivity is dominated by ρ_i which is then the residual resistivity [17].

$$\rho = \rho_i + \rho_L \qquad [\Omega.m] \qquad \textbf{Equation 1.2}$$

Wiedemann-Franz law

The Wiedemann-Franz law states that the thermal conductivity, k [$W.m^{-1}.K^{-1}$], and electrical resistivity, ρ, are inversely related by Equation 2.2.

$$k.\rho = L_0.T \qquad \textbf{Equation 1.3}$$

Where L_0 [$W.\Omega.K^{-2}$] is the Lorentz number and T is the temperature. In current lead design, both the heat conduction due to the thermal conductivity, and the heat generation due to the resistivity must be minimised. However, due to the Wiedemann-Franz relationship there is a minimum heat leak for a given current [11]. This is obtained by calculating the optimum geometry of the current lead.

1.5.3 Thermal and electrical properties of (BiPb)2223 conductors and coil composites

The thermal and electrical properties of the stabilising matrix and the thermal properties of the entire coil winding influence the stability and protection of HTS coils. The conductor

that is used in subsequent chapters is the 'Zerome Hercules' (BiPb)2223 conductor produced by Nordic Superconductor Technologies (NST). This conductor has a 0.1MgNi-Ag alloy outer sheath with Ag between the filaments. The thermal conductivity along the length of the conductor, $K_{longitudinal}$, is shown in Figure 1.6. For temperatures over 20K this data was obtained from measured results for this specific conductor [20]. For temperatures below 20K the values of Ag with a residual resistivity ratio (RRR) of 100 were used [32], this data was seen to match the measured data above 20K. Figure 1.6 also shows the radial thermal conductivity, K_{radial}, across a section of coil winding comprising of conductor, fibreglass and epoxy resin. This data was obtained from measurements as detailed in section 6.3. Figure 1.7 shows the data used for the combined resistivity of the Ag/ Ag alloy sheath and the specific heat of the coil winding. The data used for the resistivity is for Ag with a RRR of 100 [32] and the specific heat is obtained from measurements as detailed in section 6.3.

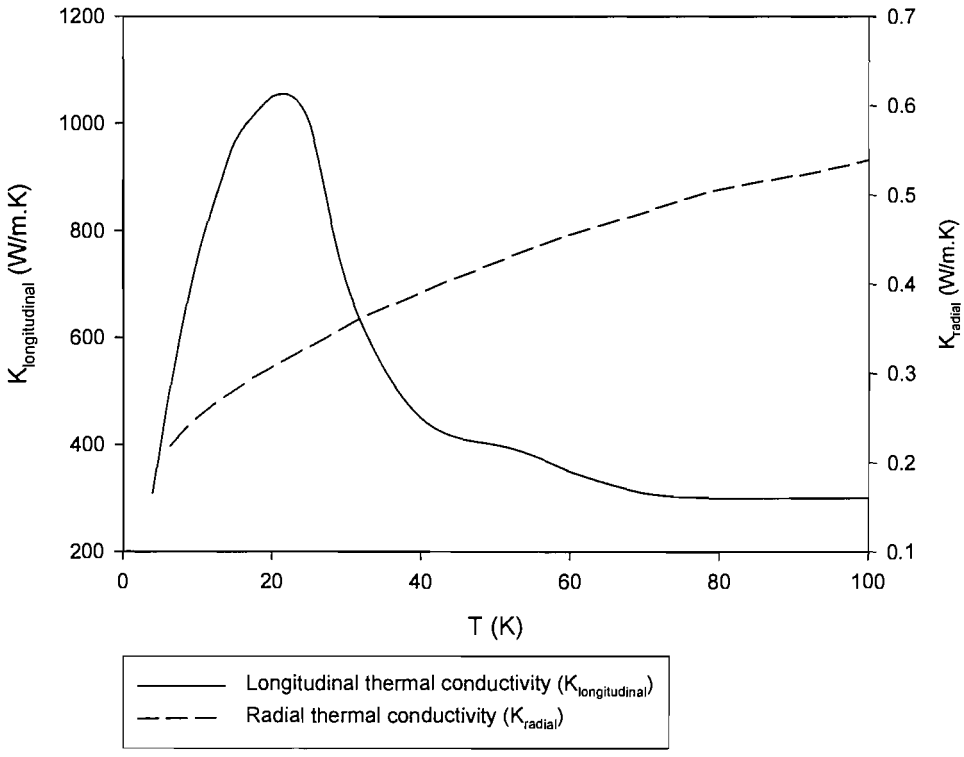

Figure 1.6: Thermal conductivities along the conductor and radially across a section of the coil winding

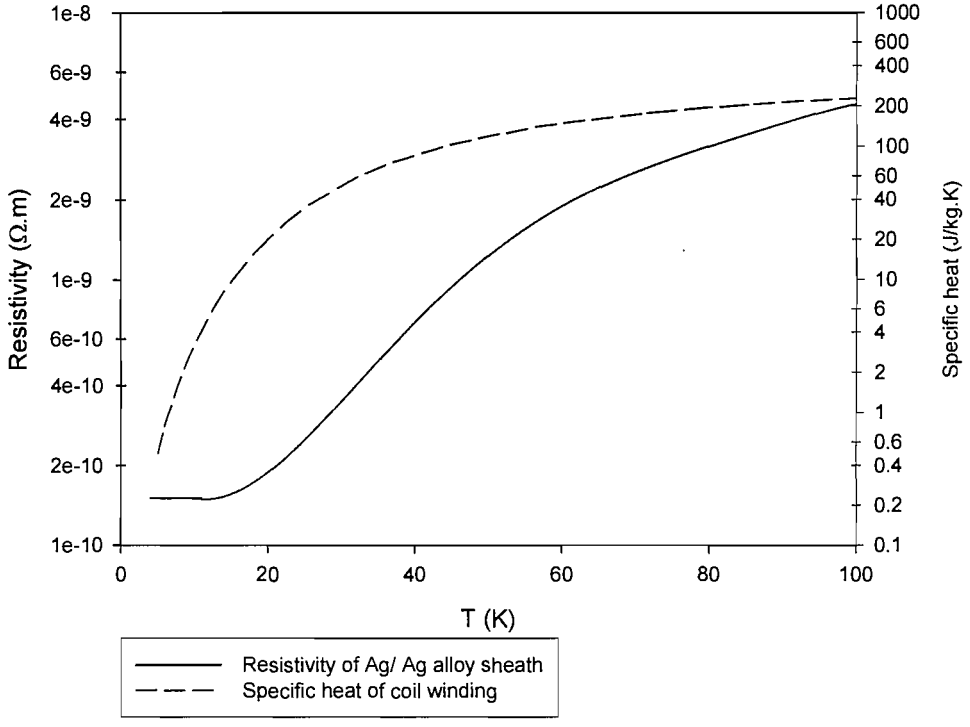

Figure 1.7: Resistivity of Ag/ Ag alloy sheath and specific heat of coil winding

1.6 References

[1] Onnes, H.K., ***Leiden Commun.***, 1911, 120b, 122b, 124c

[2] Poole, C.P., Farach, H.A., Creswick, R.J., **Superconductivity**, Academic Press, 1995

[3] Meissner, W., Oschenfeld, R., ***Naturwissenschaft***, 1933, vol. 21, pp. 787

[4] Iwasa, Y., **Case studies in superconducting magnets, design and operational issues**, Plenum Press, 1994

[5] Bednorz, J.G., Műller, K.A. 1986, ***Z. Phys. B***, vol. 64, pp.189-193

[6] Wu, M.K, Ashburn, J.R., Torng, C.J., ***Physical Review Letters***, 1987, vol. 58, no. 9, pp.908-910

[7] Maeda, H., Tanaka, Y., Fukutomi, M., Asano, T., ***Japanese Joural of Applied Physics***, 1988, vol. 27, no. 2, p.209-210

[8] Doss, J.D., **Engineer's guide to high-temperature superconductivity**, John Wiley & Sons Inc., 1989

[9] Goren, S., ***Advanced Studies on Superconducting Engineering 2004***, Lecture notes

[10] Abrikosov, A.A, ***Sov. Phys. JETP***, 1957, vol. 5, pp. 1174 (In Russian)

[11] Wilson, M.N., **Superconducting magnets**, Oxford University press, 1983

[12] Shu-Ang, Z., **Electrodynamic theory of superconductors**, Peregrinus, 1991

[13] Tinkham, M., **Introduction to Superconductivity**, McGraw-Hill, 1975

[14] Bean, C.P., ***Physical Review Letters***, 1962, vol. 8, p.250

[15] Goodman, B.B., ***Physical Review Letters***, 1961, vol. 6, p. 597

[16] Sheahen, T.P., **Introduction to high temperature superconductivity**, Plenum Press 1994

[17] Seeber B., **Handbook of applied superconductivity**, vol. 1, Institute of Physics, 1998

[18] Bulaevei, L.N., ***Physcal Review B***, 1992, vol. 45, pp. 2545

[19] Hensel, B., Grivel, J.C., Jeremie, A., Perin, A., Pollini, A., Flukiger, R., ***Physica C***, 1993, vol. 205, pp.329-337

[20]Vase, P., Flukiger, R., Leghissa, M., Glowacki, B., ***Superconductor Science and Technology***, 2000, vol. 13, pp. 71-84

[21] American Superconductor Corporation, ***www.amsuper.com***,

[22] R. Flukiger, ***IEEE Transactions on Magnetics***, 1991, vol. 27, no. 2, pp.1258-1263

[23] Mao, C., ***Physica C***, 1997, vol. 281, no. 2-3, pp. 159-175

[24] Yau, J., Savvides, N., ***Applied Physics Letters***, vol. 65, no. 11, p.1454-1456

[25] Komarek, P., ***Advanced Studies on Superconducting Engineering 2004***, Lecture notes

[26] Weijers, H.W., Trociewitz, U.P., Marken, K., Meinesz, M., Miao, H., Schwartz, J., ***Superconductor science and technology***, 2004, vol. 17, pp. 634-644

[27] Spiller, D.M, Beduz, C., Al-Mosawi, M.K., Friend, C.M., Thacker, P., Ballarino, A., ***Superconductor science and technology***, 2001, vol. 14, pp. 168-172

[28] Innopower, ***www.innopower.com***

[29] Hands, B.A., **Cryogenic Engineering**, Academic Press, 1986

[30] Wigley, D.A., **Materials for low-temperature use**, Engineering design guides 26, Oxford University Press, 1978

[31] Scurlock, R.G., **Low temperature behaviour of solids: An introduction**, Routledge and Kegan Paul, 1966

[32] Smith, D.R., Fickett, F.R., ***Journal of Research of the National Institute of Standards and Technology***, 1995, vol. 100, pp. 119

Chapter 2 : Thermal stability and protection of superconducting windings

2.1 Introduction

During operation superconducting windings are subject to disturbances that supply energy to the winding. The temperature rise associated with this energy input may cause a section of the superconductor in the winding to operate outside of its critical surface. When this occurs the resistivity of the superconductor will increase to that of its normal state; the volume of the winding that is in the normal state is called the normal zone. Joule heating in the superconductor will cause the normal zone temperature to rise and unless stabilised temperatures will increase without bound; this is known as a quench. During a quench energy is dissipated in the normal zone of the winding which is often a fraction of the winding volume. The high volumetric heat generation coupled with a reduced heat capacity at low temperatures can produce a large temperature increase. The high inductance of superconducting windings dictates that even when the transport current is removed the stored magnetic energy is dissipated in the normal zone causing the temperature to continue to rise. Quenching can cause overstressing, arcing and overheating in a winding. If this is not controlled it can lead to 'burn-out' or structural failure of the winding. Early magnets manufactured in the 1960's exhibited premature quenches at a fraction of their intended operating currents, a phenomenon known as degradation. The mechanisms behind the stability of LTS windings are now more fully understood but must be considered at every stage of the magnet design and manufacturing process to obtain a thermally stable magnet.

One potential application of devices based on high temperature superconductors (HTS) is their use in many parts of the electrical power network from generators to power transmission lines. Benefits can be gained from low power loss, low environmental footprint [1] and device size reduction. Operational reliability is a huge boundary to the implementation of HTS technologies and therefore it is important to understand the factors that affect the quench characteristics of HTS windings.

2.2 Disturbances

2.2.1 The disturbance spectrum

Energy is introduced into superconducting windings by disturbances that produce a temperature rise in a section or all of the winding. Wipf [2] introduced the concept of a disturbance spectrum to class the types of disturbances to which a winding was subjected. Disturbances are classed as point or distributed disturbances relating to their spatial distribution and as continuous or transient disturbances relating to their temporal distribution. Both point and distributed continuous disturbances cause a constant heat input to the winding and examples include resistive joints in the winding, heat leak caused by poor insulation and excessive losses from operation with alternating current. These types of disturbances are well understood and are therefore avoided with good cryostat and winding design.

Transient disturbances release a sudden pulse of energy into the winding that can initiate a quench. Examples of transient disturbances include flux jumping, eddy current heating and mechanical disturbances such as epoxy cracking events and local yielding of the conductor. As discussed in Chapter 1 flux jumping is well understood and can be eliminated by correct conductor design. Mechanical disturbances are more difficult to quantify and locate in a winding but it is thought they are strongly interlinked with the initiation of quench in coils. This has been demonstrated using voltage detection methods combined with acoustic emission techniques [3,4] and by using techniques that can locate the point of quench initiation by measuring the change in field produced by current sharing in the conductor [5]. The minimum energy of a transient point disturbance that is needed to initiate a quench in a winding is known as the minimum quench energy (MQE [J]).

2.2.2 Reducing disturbances in a superconducting winding

One method of fabricating coils is to wind them 'dry' whereby the winding tension and frictional forces between turns hold the winding together. If the Lorentz force on a turn in the winding is greater than the frictional force holding it in place then the turn will slip thus dissipating energy into the winding. To combat the problem of winding motion an

impregnate can be used to hold the turns of the winding in place. An impregnate must have sufficient strength to endure the stresses present in the winding, must be easily applicable and maintain turn-to-turn insulation properties. In modern high performance windings epoxy resin is mainly used due to its superior mechanical properties. Epoxy can however crack when stressed causing stored strain energy to be converted to a local heat pulse that can initiate a quench.

2.3 Composite superconductors and current sharing

To produce stable superconducting wires and tapes the superconducting filaments are processed with a stabilising matrix that has a high thermal conductivity and low resistivity. To demonstrate the purpose of the matrix a bath cooled composite conductor in which a normal zone has been created will be considered as shown in Figure 2.1. Current flowing in the superconductor, I_{SC} [A], is shunted around the highly resistive normal zone through the low resistance matrix, I_M [A], therefore limiting the heat generated in the superconductor; a process known as current sharing. Joule heat generated in the stabilising matrix is removed by cooling at the surface of the conductor and if the cooling is adequate temperatures will fall to a level such that superconductivity is recovered. If the joule heat generated by the matrix exceeds the cooling then temperatures will rise and a quench will occur.

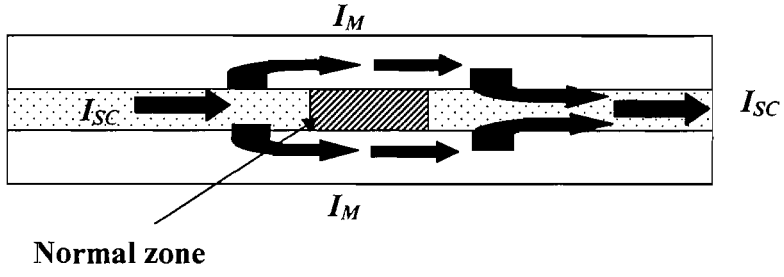

Figure 2.1: Current sharing around a normal zone in a stabilised superconductor

2.4 Cryostability

Stekly and Zar [6] demonstrated that a stabilised superconductor can be designed to be unconditionally stable against disturbances of all magnitudes by ensuring that the joule heat generated in the matrix is at all times lower than the cooling provided at the conductor surface by a cryogen. This principle is demonstrated diagrammatically in Figure 2.2 [9] for a NbTi conductor bath cooled in liquid helium. The solid line and dashed line are the heat generation per unit cooled surface [$W.m^{-2}$] and cooling per unit cooled surface [$W.m^{-2}$] respectively. It must be noted that there is no heat transfer from the ends of the resistive section only from the surface of the conductor.

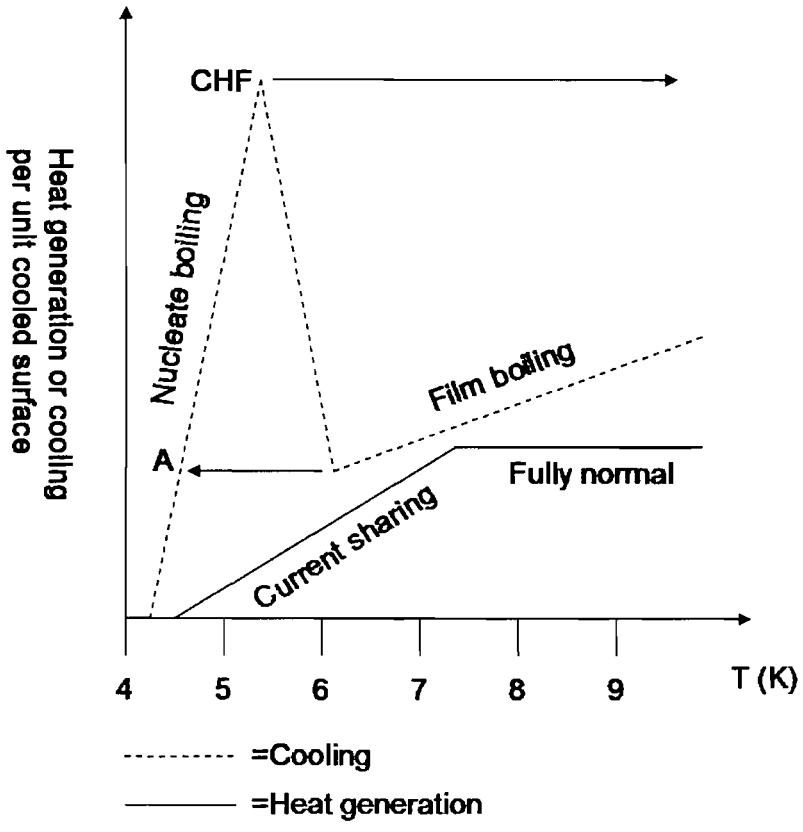

Figure 2.2: Heat generation and cooling in a cryostable conductor

The cooling curve is characteristic of boiling heat transfer from a surface. In the nucleate boiling region the liquid cryogen remains in contact with the surface and a high heat transfer coefficient is observed. In the film boiling region a vapour film coats the entire

surface resulting in a poor heat transfer coefficient. The boiling characteristic exhibits hysteresis as demonstrated by the arrows in Figure 2.2. If the critical heat flux (CHF) is exceeded the temperature jumps approximately 30K [8] to the point on the film boiling region at that heat flux. When the heat flux is reduced the temperature of the surface follows the film boiling region and then jumps to point A in the nucleate boiling regime. Below a certain temperature, shown as 4.5K in Figure 2.2, the superconductor carries all of the current and therefore no heat is generated in the conductor. Above this temperature the voltage of the superconductor starts to rise and current is shared with the stabilising matrix of the conductor. When the superconductor is fully normal the stabilising matrix carries all of the current and a constant heat generation is observed due to the constant resistivity of the sheath material below 20K.

The ratio of the heat generated per unit cooled surface to the cooling per unit cooled surface is denoted as $\alpha(T)$ [dimensionless] and given by Equation 2.1 [6]. Where G [$W.m^{-3}$] is the volumetric heat generation, A [m^2] is the cross sectional area of the conductor, L [m] is the conductor length, P [m] is the cooled perimeter, h [$W.m^{-2}.K$] is the heat transfer coefficient, T_C [K] is the critical temperature of the superconductor, and T [K] is the coolant bath temperature. The Stekly and Zar criterion dictates that $\alpha(T)<1$ for complete cryostability. The main disadvantage of ensuring complete cryostability is the need to reduce the current density of the conductor and include cooling channels between the windings resulting in thicker coil sections and hence an increase in the cost of the magnet. The cost increase is prohibitive on smaller bore magnets but becomes acceptable on larger bore magnets especially when the cost of a failed magnet is accounted for [8].

$$\alpha(T) = \frac{\left(G.A.L/P.L\right)}{h.(T_C - T_0)} = \frac{G.A}{P.h.(T_C - T)} \quad \text{[dimensionless]} \qquad \textbf{Equation 2.1}$$

2.5 'Equal area' criterion

The equal area criterion is a form of cryostability that accounts for the heat transfer along the conductor. It was formulated by Maddock, James, and Norris [7] who showed that unconditional stability could be achieved at higher current densities than previously expected. This principle is demonstrated in Figure 2.3 for a NbTi conductor cooled in a liquid helium bath. It can be seen that steady states exist when the whole conductor is at 4.2K and at 9K as shown by point 1 and point 3 respectively. An unstable equilibrium also exists when the whole conductor is at point 2, where any small perturbation will make the temperature of the entire conductor go to either 4.2K or 9K. Importantly it was shown that a solution exists where one end of the conductor is at T1 and another end at T3 with a stationary temperature profile between them. This occurs when area A is equal to area B. Excess heat generated in the warm section of the conductor, area B flows down the temperature gradient and balances the excess cooling towards the cool end, area A [7].

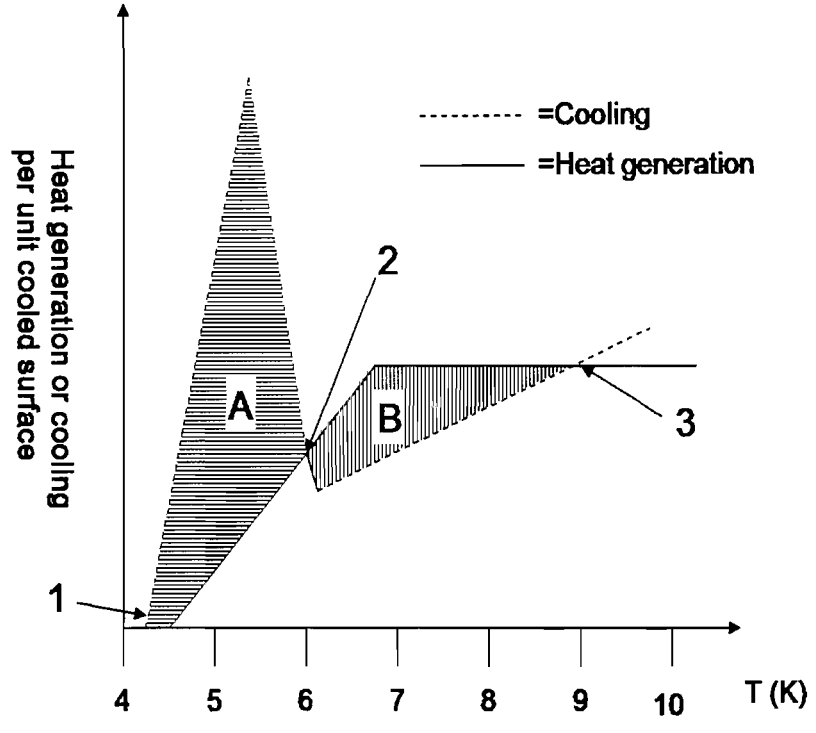

Figure 2.3: Heat generation and cooling for a conductor obeying the 'equal area' criterion

The equal area criterion allows for operation at higher current densities than the Stekly and Zar criterion. However, the current densities achievable still make smaller bore magnets designed using this criterion prohibitively expensive.

2.6 The Minimum Propagating Zone

Consider a wire of unstabilised superconductor cooled only from its ends and carrying a current density, J_{SC} [A.m^{-2}], as shown in Figure 2.4. The wire is subjected to a disturbance that drives a length, l [m], of the conductor normal. Heat is generated in the normal zone by joule heating and removed from the normal zone by conduction along the length of the conductor. There is an initial disturbance length at which the heat generation in the normal zone is equal to the heat removed by conduction. This is not a stable equilibrium, if the size of the normal zone becomes slightly smaller then more heat will be conducted away from the normal zone than is generated causing the normal zone to shrink and vice versa [8]. The size of the disturbance that represents the boundary between stable recovery and unstable growth of the normal zone is called the Minimum Propagating Zone (MPZ) [2,9]. The MPZ concept provides an estimate of the geometrical size of disturbance that is needed to initiate a quench.

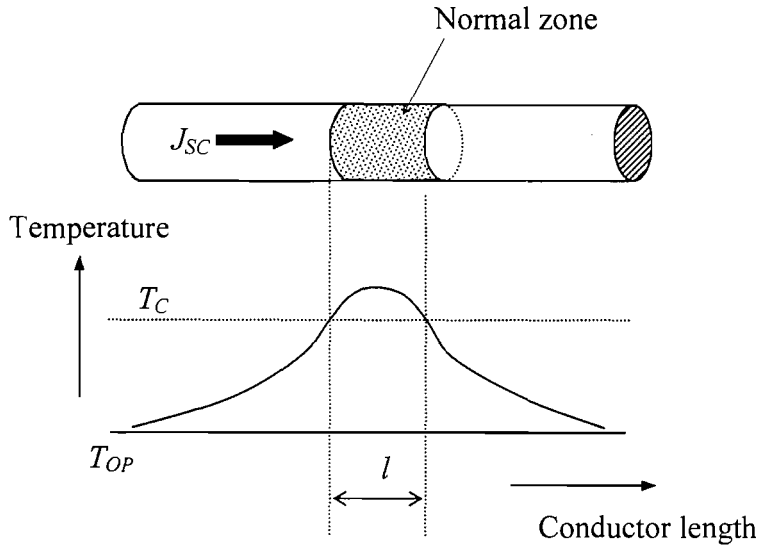

Figure 2.4: Unstabilised superconductor, MPZ derivation

2.6.1 MPZ size estimation

In the one dimensional case discussed above an expression for the MPZ length of an unstabilised conductor can be derived by equating the heat generation and cooling terms and rearranging to produce Equation 2.2. Where l_{US} [m] is the length of a unstabilised MPZ, k_{SC} [W.m^{-1}.K^{-1}] and ρ_{SC} [Ω.m] are the thermal conductivity and electrical resistivity of the superconductor respectively, T_C is the critical temperature of the superconductor, and T_{OP} [K] is the operating temperature of the superconductor. Equation 2.2 is a very basic estimate of the MPZ size in one dimension but proves useful when examining the stability of stabilised and unstabilised conductors.

$$l_{US} = \sqrt{\frac{2k_{SC}(T_C - T_{OP})}{\rho_{SC} J_{SC}^{\ 2}}} \quad [\text{m}] \qquad \textbf{Equation 2.2}$$

Because of the high resistivity and low thermal conductivity of both LTS and HTS materials the MPZ of an unstabilised conductor is very small. For example a NbTi wire carrying 500A at 4.2K and a (BiPb)2223 bulk conductor at 4.2K carrying 300A both cooled from the ends will have a MPZ of approximately 0.3μm and 5μm respectively. Disturbances that cause minute sections of the winding to go normal will therefore initiate a quench. If a composite conductor as described in section 2.3 is analysed the length of the MPZ is calculated as shown in Equation 2.3.

$$l_S = \sqrt{\frac{2k_M(T_C - T_{OP})}{\rho_M J_M^{\ 2}}} \quad [\text{m}] \qquad \textbf{Equation 2.3}$$

Where l_S [m] is the length of a stabilised MPZ and k_M [W.m^{-1}.K], ρ_M [Ω.m] and J_M [A.m^{-2}] are the thermal conductivity, resistivity and current density of the stabilising matrix respectively. The MPZ length is increased drastically because of the high thermal conductivity and low resistivity of the stabilising matrix. For the above example the MPZ would be approximately 6mm and 20mm for the LTS and HTS conductors respectively.

Consider an epoxy impregnated winding such that each conductor is in good thermal contact with the adjacent turns in the winding [8]. A MPZ formed in the winding will be ellipsoidally shaped due to the anisotropy of the thermal conductivities in the winding. The

MPZ will be longer in the direction of winding and shorter in the radial and axial directions. The radial and axial thermal conduction effectively increases the cooling and therefore an impregnated winding can sustain a larger hotter MPZ than a wire cooled at its ends.

2.6.2 Estimating the MQE using the concept of a MPZ

The MPZ concept can be used to estimate the tolerance of a winding to energy disturbances. If the energy needed to create the MPZ is taken as the energy needed to initiate a quenching normal zone then the energy needed to initiate a quench, ΔE [J], can be estimated using Equation 2.4.

$$\Delta E = V_{MZ} \int_{T_{OP}}^{T_C} C_{WD}(T) dT \qquad [\mathrm{J}] \qquad \textbf{Equation 2.4}$$

Where V_{MZ} [m^3] is the volume of the MPZ, $C_{WD(T)}$ [$J.m^{-3}.K^{-1}$] is the volumetric heat capacity of the winding at a given temperature, T_{OP} is the operating temperature of the superconductor and T_C is the critical temperature of the superconductor. The above analysis neglects the temperature profile away from the normal zone but this halo region around the normal zone can be accounted for if a more accurate prediction is needed [9]. The MQE of a coil wound with a stabilised NbTi conductor is of the order of micro-Joules where as the MQE of a coil wound with a stabilised (BiPb)2223 conductor is of the order of Joules. It is remarkable that these relatively small releases of energy can cause the dissipation of many mega-Joules of energy that can be stored in a superconducting magnet.

The MPZ concept can provide a measure of the size and magnitude of the disturbance that will initiate a quench in windings in which cooling to the conductors is provided by conduction. It is therefore useful when designing impregnated coils which can be treated as adiabatic because the effect of the cooled boundary on the normal zone during propagation is minimal.

2.7 Heat generation in a superconducting composite

2.7.1 Current sharing model

A superconducting composite can be represented by two parallel resistors one representing the superconductor and the other the stabilising matrix as shown in Figure 2.5.

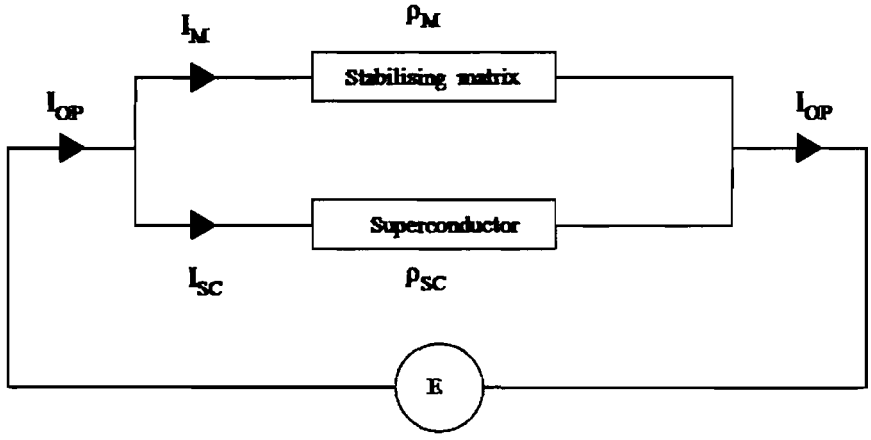

Figure 2.5: Current sharing model of a composite superconductor

The superconductor has a non-linear current-voltage characteristic whilst the matrix exhibits an ohmic resistance. By equating the operating current flowing through the conductor, I_{OP} [A], with the sum of the current flowing through the superconductor, I_{SC}, and the stabilising matrix, I_M, the current-voltage characteristic of the composite can be estimated as shown in Equation 2.5 to 2.7. Where E [V.m^{-1}] is the electric field across the conductor, E_C [V.m^{-1}] is the electric field at the critical current (1μV/cm), $n(T)$ [dimensionless] is the n-value from the power law, $\rho_M(T)$ is the resistivity of the stabilising matrix and A_M [m^2] is the area of the stabilising matrix. The temperature dependent properties must be considered when computing the current-voltage characteristics in HTS because of the highly temperature dependent material properties over the operating temperature range.

$$I_{SC} = \left(\frac{E}{E_C}\right)^{\frac{1}{n(T)}} \cdot I_C(T) \qquad \text{[A]} \qquad \textbf{Equation 2.5}$$

$$I_m = \frac{E}{\rho_m(T)} \cdot A_m \qquad [\text{A}] \qquad \textbf{Equation 2.6}$$

$$I_{OP} = \left(\frac{E}{E_C}\right)^{\frac{1}{n(T)}} \cdot I_C(T) + \frac{E}{\rho_m(T)} \cdot A_m \qquad [\text{A}] \qquad \textbf{Equation 2.7}$$

2.7.2 Prediction of the current-voltage characteristics

Equation 2.7 was used to calculate the current-voltage characteristics of a HTS tape comprising (BiPb)2223 filaments and a Ag alloy stabilising matrix. The simulated characteristics are compared to measured values in Figure 2.6. The operating temperature was set at 77K to simulate cooling in a liquid nitrogen bath. Figure 2.6 is presented in the form of operating current density, J_{OP} [A.m^{-2}], and electric field, E, to aid calculation of the heat generation as explained in section 2.7.3. There is good agreement between measurement and prediction when an n-value of 16 and a stabilising matrix resistivity of 3.9 x 10^{-9} Ω.m are used for the fitting.

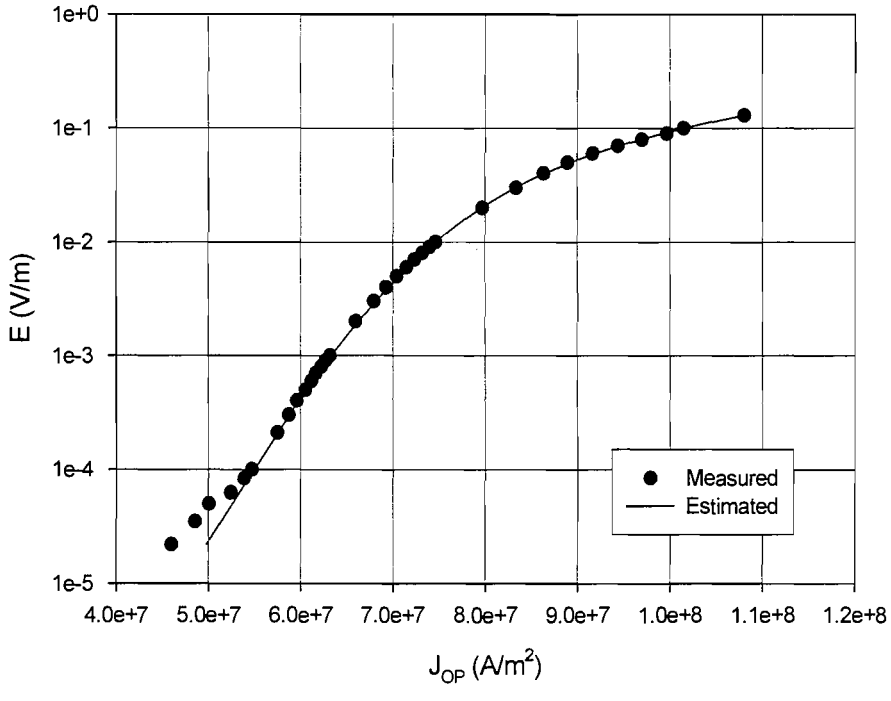

Figure 2.6: Measured and predicted E-J curve at 77K

2.7.3 Prediction of the heat generation as a function of temperature

The temperature dependent volumetric heat generation of a superconducting composite, $G=E.J$ [W.m^{-3}], can be estimated by calculating Equation 2.7 at various temperature increments. The relevant temperature dependent material properties are applied at each temperature increment. The calculation was performed for a (BiPb)2223 conductor and a NbTi conductor, as shown in Figure 2.7 and Figure 2.8 respectively. The characteristics of the two conductors are detailed in Table 2.1. As can be seen the temperature range over which current sharing occurs for the NbTi conductor is narrow due to a low critical temperature and the electric field rises steeply due to a high n-value. The temperature dependent heat generation is therefore often approximated as a step function in many quench analyses. Conversely the (BiPb)2223 conductor exhibits a wide temperature range over which current sharing occurs and the n-values are low leading to a broad sloping temperature dependent heat generation. The NbTi conductor shows a constant heat generation when the superconductor has transitioned to the normal state. This is caused by the heat generation from the sheath which is governed by the constant resistivity of copper below approximately 20K. The (BiPb)2223 conductor exhibits a temperature dependent heat generation above the superconductor's critical temperature (110K) due to the temperature dependent resistivity of the Ag alloy stabilising matrix.

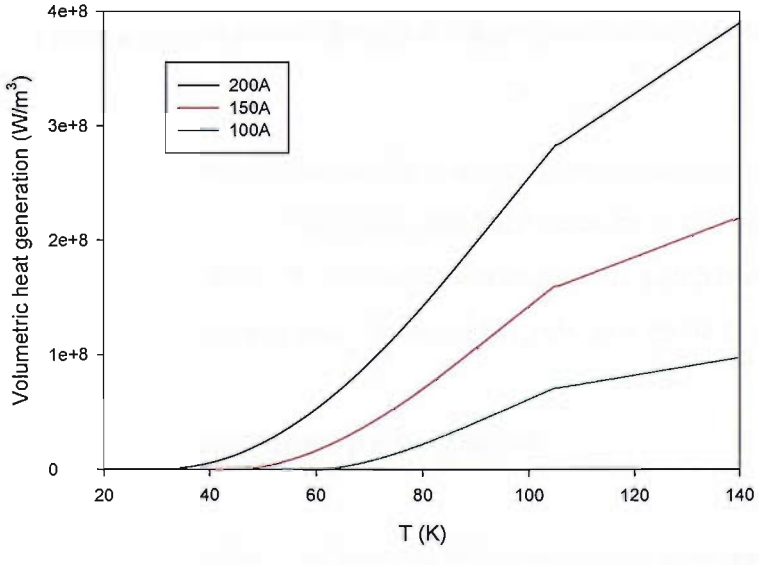

Figure 2.7: Volumetric heat generation as a function of temperature for various currents for a (BiPb)2223 conductor

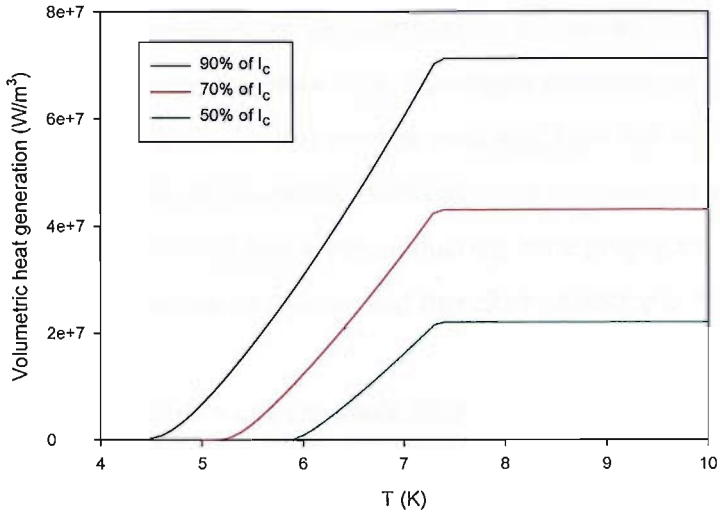

Figure 2.8: Volumetric heat generation as a function of temperature at various currents for a NbTi conductor

	(BiPb)2223	NbTi
n-value	28→17	50
I_c	60A, (self field, 77K, 1μV/cm)	940A (4T, 4.2K, 0.1μV/cm)
Stabilising matrix	Ag/ Ag alloy	Copper, RRR=125

Table 2.1: Conductor details for heat generation calculations

It is difficult to equate the approximation of a step heat generation conventionally used for LTS conductors in calculations for MPZ size and NZP velocity to the broad sloping heat generation characteristics of HTS. When the approximation of a step heat generation is used with HTS the results obtained must be treated merely as a guide to investigate trends.

2.8 Protection and normal zone propagation

The subject of 'protection' relates to how an initiated normal zone propagates through a superconducting winding and how the resulting quench can be safely controlled. A normal zone initiated in a superconducting winding will rapidly increase in temperature and grow

due to a process of joule heat generation and heat diffusion; this is known as normal zone propagation. The normal zone propagation is driven by the stored magnetic energy in the winding and the applied transport current. The maximum temperature of the normal zone will depend on the energy supplied to the normal zone and how fast heat diffuses from the normal zone. The normal zone propagation (NZP) velocity represents the rate at which the boundary between the normal zone and superconducting zone propagates. Superconducting windings have anisotropic thermal properties and therefore anisotropic NZP velocities.

In windings operated in persistent current mode high NZP velocities ensure that the stored electromagnetic energy of the winding is spread over the winding volume quickly so that the maximum temperature of the normal zone is kept below a tolerable level. Magnets that have sufficiently high NZP velocities, so as not to become damaged when they quench, are referred to as self protecting. When a winding directly connected to a power supply undergoes a quench the winding will continue to be supplied with energy. Temperatures will therefore rise to intolerable levels unless the current is ramped down in sufficient time using a protection system.

During a quench as well as a large temperature rise, large voltages are developed across the normal zone because of the high rate of current decay across this resistive zone. The large voltages can cause insulation breakdown and arcing between turns. A protection system limits the maximum temperature rise and ensures the voltages are kept below a safe level; methods of protecting magnets are detailed in Section 2.9.

2.8.1 Longitudinal NZP velocity calculation

Consider a superconductor composite in which a quench has been initiated. As shown in Figure 2.9, there is a propagating boundary between the normal and superconducting zones. Once initial transients have died away, the general approach to obtain the normal zone propagation velocity in the longitudinal direction is to assume that the velocity of the normal-superconducting boundary has reached a steady state and to use a travelling wave solution [3,10,11,12]. For NZP modelling, the coil can be considered adiabatic [13]. This assumption holds true for conduction cooled windings since a cryocooler delivers cooling

only through thermal conduction and thus the response of the cryocooler to a rapid temperature change within the coil is attenuated.

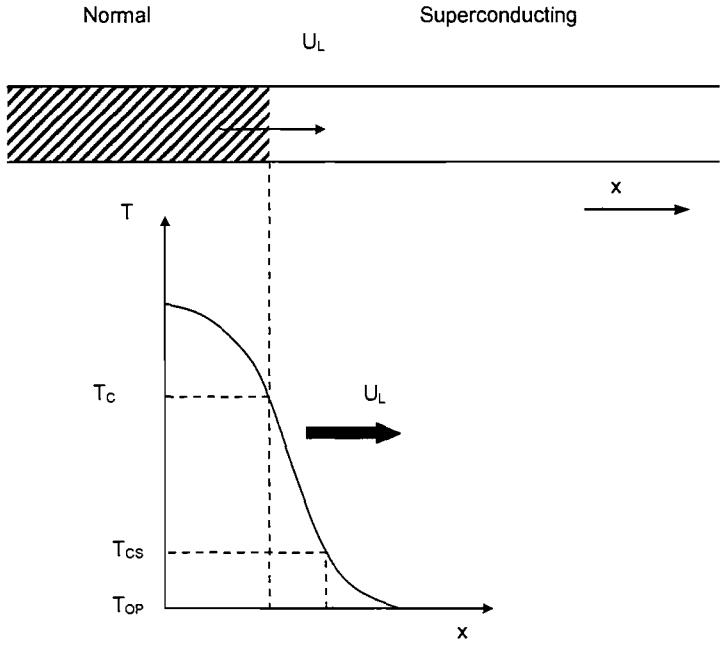

Figure 2.9: Propagating normal zone and temperature distribution along the conductor

The power density equation for the normal zone and for the superconducting zone are solved and combined [3] to give the propagation velocity in the longitudinal direction as shown by Equation 2.11. The volumetric heat generation, G, is modelled as a step function as shown in Equation 2.8 to 2.10.

Above T_T': $G = \rho_m J_m^2$ [W.m^{-3}] **Equation 2.8**

Below T_T': $G = 0$ [W.m^{-3}] **Equation 2.9**

Where: $T_T' = \frac{(T_C + T_{CS})}{2}$ [K] **Equation 2.10**

$$U_L = \frac{J_m}{\widetilde{C}_{cd}} \sqrt{\frac{\rho_m k_m}{(T_T' - T_{OP})}}$$ [m.s^{-1}] **Equation 2.11**

Where U_L [m.s^{-1}] is longitudinal normal zone propagation velocity, J_m is the current density of the stabilising matrix, $\widetilde{C}_{cd}$ [W.m^{-3}.K] is the average volumetric heat capacity of the conductor over the temperature range, ρ_m is the resistivity of the stabilising matrix, k_m is the thermal conductivity of the stabilising matrix, T_T [K] is defined in Equation 2.10, T_{OP} is the operating temperature, T_C is the critical temperature of the superconductor and T_{CS} [K] is the temperature at which current sharing starts. The assumption of a step heat generation in the derivation of Equation 2.11 is accurate for LTS but it becomes more inaccurate to use when covering a wide temperature span [3], such as with HTS. This is because the characteristics of the propagating temperature front in HTS are greatly different from LTS mainly due to the differing heat generations as shown in Figure 2.7 and Figure 2.8. Equation 2.11 can however be used to approximate the longitudinal NZP velocity of a HTS tape. Considering an Ag sheathed (BiPb)2223 conductor at 77K, with an operating current of 60A, Equation 2.11 estimates a longitudinal NZP velocity of 21mm/s which is of the same order as measured values, see Table 2.3 in section 2.10.

2.8.2 Transverse NZP velocity calculation

Joshi [11] proposed a model for estimating the transverse NZP velocity. A thermal circuit, Figure 2.10, represents two adjacent turns of a coil separated by insulation, with thermal resistance R_i [K.W^{-1}] and the volumetric heat capacity C_i [W.m^{-3}.K^{-1}]. The derivation of the

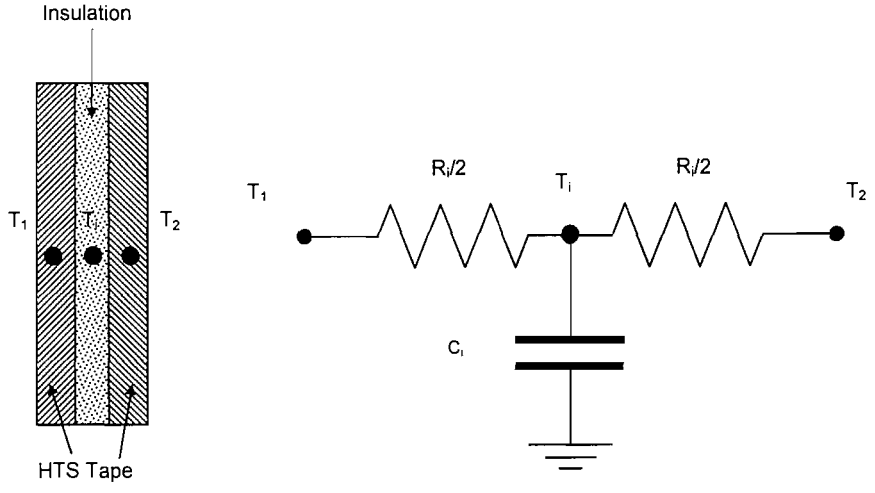

Figure 2.10: Thermal model of a section of a HTS coil

transverse NZP velocity, U_T [m.s^{-1}] is obtained by solving the equation for the normal zone transient time, τ_t [s]. Iwasa [3] proposed a simplification in which it was assumed that normal zone transient time, τ_t, is much greater than the time constant of the insulation, τ_i [s] , and this simplification is given by Equation 2.12.

$$U_T = \frac{J_m}{\widetilde{C}_{cd}} \sqrt{\frac{\rho_m k_i \delta_{cd}}{2\delta_i (T_T' - T_{OP})}} \quad [\text{m.s}^{-1}] \qquad \textbf{Equation 2.12}$$

Where U_T is the transverse NZP velocity, J_m, $\widetilde{C}_{cd}$, ρ_m, T_T' *and* T_{OP} have been defined for the longitudinal NZP velocity calculation, k_i [W.m.K] is the thermal conductivity of the insulation, and δ_i [m] and δ_{cd} [m] are the thicknesses of the insulation and conductor respectively. For a HTS coil wound with an Ag sheathed (BiPb)2223 conductor and insulated with epoxy and fibreglass, operating at 77K with a transport current of 60A, U_T can be calculated as 0.72mm/s. This is of the same order as values for U_T measured in HTS coils experimentally, see Table 2.3 below in section 2.10.

2.9 Protection systems

The aim of the protection system is to keep the temperature and voltage rise of the normal zone within tolerable limits. If it is found that temperatures are above the tolerable level a protection system must be implemented to decrease the energy dissipated per unit volume of the normal zone. There are many types of protection systems but they generally operate using either or both of two methods (1) removing the stored energy from the winding (2) increasing the volume of the normal zone using an auxiliary method.

Protection systems can also be classed as either passive or active systems. Passive protection techniques are usually cheaper, simpler and more reliable than active protection systems but dump all the energy stored in the winding into the cryostat [9] leading to excessive cryogen boil off. Active techniques such as the 'detect and dump' technique have the advantage of extracting most of the stored energy from the cryogenic environment reducing cryogen boil-off. However they rely on the reliable operation of detectors and switches and generate high voltages at the magnet terminals [9].

2.9.1 Subdivision of the winding

The superconducting winding is divided into sections and each section shunted with a resistor. When a section of the coil goes normal the shunt resistor provides an alternative path for the current to flow through, heat generation in the quenching section is therefore reduced and the normal zone temperature decreases. The inductance of each section of the winding can be chosen so that the maximum temperature of a hot spot that can form is below a set value [14]. When designing a protection system that utilises winding subdivision the mutual inductances between the coil sections must be considered. Subdivision of the winding can lead to complex quench behaviour because of inductive coupling between the sub-divided coils.

2.9.2 'Detect and dump'

The basic layout of a 'detect and dump' protection system is shown in Figure 2.11, it consists of a current supply connected to a superconducting magnet with inductance L, carrying a current I_{OP}, in which a normal zone of resistance $r(t)$ has formed. A dump resistor, R_D, and a switch, S, are connected across the magnet terminals and placed outside of the cryostat. When a quench is detected switch S is opened and a fraction of the energy

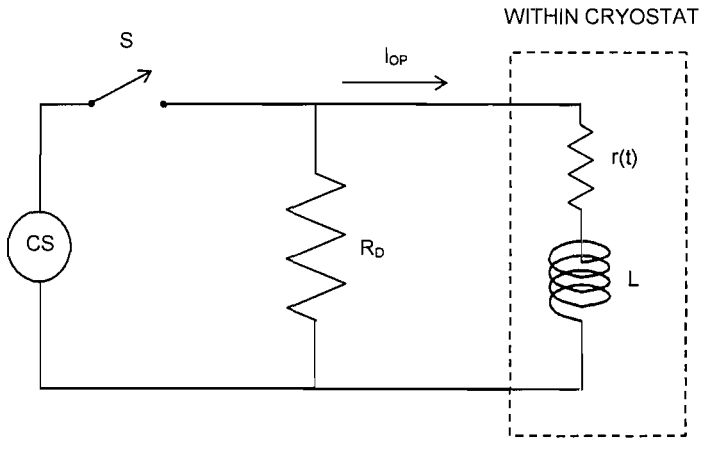

Figure 2.11: 'Detect and dump' protection system [3]

stored in the winding is dissipated in the dump resistor whilst the remainder is dissipated in the normal zone. A high resistance dump resistor creates a fast current decay and hence a lower hot spot temperature. However if the value of the dump resistor is too high arcing may occur across the current leads due to the high voltages generated during current decay [3]. Diodes can be used as a passive method to dump energy instead of resistors. The diodes develop a resistance at a set voltage and hence do not rely on detection systems or switching mechanisms.

2.9.3 Quench heaters

Heaters, such as stainless steel shim, are mounted around the coil periphery in good thermal contact with the winding. When a quench is detected the quench heaters are energised therefore initiating a propagating normal zone away from the point at which the quench originated. The normal zone volume is increased and hence coil temperatures and voltages are kept to within a tolerable level. This protection system is especially useful when protecting magnets with multiple coils that are thermally isolated; the energy in the entire magnet is then distributed over all the coils rather than only one. Certain magnets such as those used in Magnet Resonance Imaging (MRI) machines can be de-energised rapidly in an emergency. This is accomplished by activating the quench heaters therefore rapidly destroying the field by quenching the magnet.

2.9.4 Coupled secondary

A shorted secondary winding is closely coupled to a primary superconducting winding. When a quench is initiated in the superconducting winding the rapid decrease of field induces current in the coupled secondary. This removes energy from the primary superconducting winding hence reducing the hotspot temperature and voltages. The temperature of the secondary coil increases during the quench because of heating due to induced eddy currents. If the secondary coil is placed in close thermal contact with the superconducting coil it will initiate further quenching away from the normal zone. This effectively assists the spreading of the normal zone over the coil volume and hence further reduces hot spots; a phenomenon referred to as thermal quench back [15]. This technique cannot however be used to protect windings in which alternating current flows.

2.10 Stability and protection issues related to HTS

2.10.1 MQE values of HTS conductors and coils

The MQE of LTS and HTS single conductors and windings have been experimentally measured by various researchers and the results are displayed in Table 2.2. It can be seen that the MQE of the HTS coils and tapes are many orders of magnitude higher than that of the LTS. This is due to the increased temperature margin between operating temperature and critical temperature, the higher heat capacity because of a generally higher operating temperature and a lower achievable current density. It is therefore expected that mechanical disturbances will not induce quenching in HTS magnets. It must however be noted that HTS magnets still operate at low current densities compared to LTS magnets and therefore the stability of the HTS material has so far been accentuated.

Conductor	MQE (mJ)
Nb_3Sn with CuNb stabiliser [16]	0.5-2.0
NbTi epoxy fibreglass solenoid [17]	0.1-1.0
Bi-2223/Ag epoxy fibreglass pancake coil @ 65K [18]	2500-5000
Bi-2223/Ag tape @ 77K [19]	7900
Bi-2223 tape and Kapton insulation @ 10K [20]	2000-20000
Bi-2223, Ag-Mg-Au sheathed Kapton insulated coil @ 4.2K [21]	11000

Table 2.2: Measured MQE of LTS and HTS conductors and windings

2.10.2 NZP velocities in HTS conductors and coils

The NZP velocities of an initiated normal zone in both LTS and HTS have been measured by various authors and are presented in Table 2.3. It can be seen that the longitudinal and transverse NZP velocities for HTS are many orders of magnitude slower than for LTS. The main reasons for the lower NZP velocities are the higher heat capacity at the generally higher operating temperature, a larger temperature difference between the operating temperature and the critical temperature, and generally lower operating current densities.

Conductor	NZP longitudinal velocity (cm/s)	NZP radial velocity (cm/s)
Nb_3Sn epoxy impregnated coil [13]	-	8
NbTi serpentine coil [11]	100-1000	-
Ag-coated YBCO/Ni-alloy tape [22]	0.2-0.8	-
Bi-2223/ Epoxy fibreglass pancake coil [18]	-	0.12
Bi-2223 tape and Kapton insulation [20]	1.0-2.0	0.02-0.04
Bi-2223, Ag-Mg-Au sheathed Kapton insulated coil @ 4.2K [21]	0.1-0.9	

Table 2.3: Experimental values for the NZP velocities

During a quench hot spots may be generated in a HTS tape or coil due to the low NZP velocities, causing excessive heating of the conductor. Protection systems must be designed such that a localised quench can be detected and a method of protection activated to ensure the magnet quenches safely.

2.10.3 The 'Thermal quench' phenomenon

It has been observed that above a certain current a HTS winding cannot maintain thermal stability because the joule heat generated exceeds the heat removal. This current is denoted as the 'quench current' [23], 'thermal quench current' [24] or 'thermal runaway current' [25]. In this case the quench develops as a slow global increase in temperature caused by heat generation distributed over the whole coil [26] followed by a rapid thermal runaway. The coil can quench without distinctive normal zone propagation or large temperature gradients [27]. The quench current depends on the cooling geometry, heat generated by the conductor and thermal properties of the winding. Attempts have been made to predict the quench current [23,25]. Co-workers from Kyushu university and the Russian academy of sciences [24] have developed a 'Universal scaling law' for HTS devices that derives the quench current and the time until thermal runaway occurs. This scaling law was developed from the heat balance in the coil without any use of the idea of superconductivity and normal zone propagation.

2.11 References

[1] Hartikainen,T., Lehtonen L., Mikkonen R., ***Superconductor science and technology***, 2003, vol. 16, pp. 963-969

[2] Wipf, S.L., ***Los Alamos Scientific Laboratory Report***, 1978, LA2725

[3] Iwasa, Y., **Case studies in superconducting magnets, design and operational issues**, Plenum Press, 1994

[4] Iwasa, Y., ***IEEE Transactions on Magnetics***, 1992, vol. 28, no.1 , pp.113-120

[5] Ogitsu, T., et al., ***IEEE Transactions on Magnetics***, 1994, vol.30, no.4, pp.2273-2276

[6] Stekly, Z., Zar, J., ***IEEE Tranactions on Nuclear Science***, 1965, vol.12, pp. 367-372

[7] Maddock, B.J., James G.B., Norris, W.T., ***Cryogenics***, 1969, vol. 9, pp.261-273

[8] Wilson, M.N., Iwasa, Y., ***Cryogenics***, 1978, vol. 18, pp.17-25

[9] Martinelli, A.P., Wipf, S.L., ***Proc. 1972 Appl. Supercond. Conf.***, IEEE P u b l . No.72CH0682-5-TABSC, pp. 331-340

[10] Wilson, M.N., **Superconducting magnets**, Oxford University press, 1983

[11] Yoshi., C.H. Iwasa, Y., ***Cryogenics***, 1989, vol. 29, pp.157-167

[12] Cherry W.H., Gittleman, J.I., ***Solid-state Electronics***, 1960, vol. 1, pp.287-305

[13] Lim, H., Iwasa Y., Smith, J.L., ***Cryogenics***, 1995, vol. 35, pp. 367-373

[14] Xiao, L.Y., Kiyoshi, T., Ozaki., O., Wada, H., ***Cryogenics***, 1999, vol. 39, pp. 293-298

[15] Green, M.A., ***Cryogenics***, Jan 1984, pp. 3-10

[16] Kaneko, T., Seto, T., Nanbu, T., Murase, S., Shimamab S., Awaji, S., Watanabe, K., Motokawa, M., Saito, ***IEEE Transactions on Applied Superconductivity***, 2000, vol. 10, no. 1, pp. 1235-1238

[17] Superczynski. M.K., ***IEEE Transactions on Magnetics***, 1979, vol. 15, no. 1, pp.325-327

[18] Penny, M., Beduz, C., Yang, Y., Manton, S., Wroe, R., ***Applied-Superconductivity-1997-Proceedings-of-EUCAS-1997***, 1997, vol.2, pp.1551-1554

[19] Wu, C.L., Bai, Z.M., Li, J.H., Wang, J.X, ***Physica C***, 2003, vol. 386, pp.162-165

[20] Kim, S.B., Ishiyama, A., ***IEEE Transactions on Applied Superconductivity***, 1997, vol. 7, no. 2, pp. 203-206

[21] Oh, S.S, Wang, Q.L., Ha, H.S., Jang, H.M., Ha, D.W., Ryu, K.S., ***IEEE Transactions on Applied Superconductivity***., 1999, vol. 9, no.2

[22] Trillaud, F., Palanki, H., Trociewitz, U.P., Thompson, S.H., Weijers, H.W, Scwartz, J., ***Cryogenics***, 2003, vol. 43, pp.271-279

[23] A. Korpela, Lehtonen, J., Mikkonen, R., Quench, ***Superconductor science and technology***, 2003, vol. 16, pp.355-360

[24] Rakhmanov, A.L., Vysotsky, V.S., Ilyin, Yu.A., Kiss, T., Takeo., M, ***Cryogenics***, 2000, vol. 40, pp. 19-27

[25] Ishiyama, A., Asai, H., ***IEEE Transactions on Applied Superconductivity***, 2001, vol. 11, no. 1

[26] Richens, P.E., Jones, H., ***IEEE Transactions on Applied Superconductivity***, 2002, vol. 12, no.1

[27] Paasi, J., Lehtonen, J., Kalliohaka, T., Mikkonen, R., ***Superconductor science and technology***, 2000, vol.13, pp. 949-954

Chapter 3 : Design, build and test of apparatus to investigate the quench behaviour of HTS pancake coils

3.1 Introduction

Cooling to the windings of conventional superconducting devices can be provided by immersing the windings in a liquid cryogen. The use of cryogens depends on a reliable delivery infrastructure and the availability of highly trained operatives, however well controlled cryogenic temperatures can be produced using closed cycle cryocoolers. Cryocoolers are powered by an electrical supply and operate by expanding compressed helium gas to produce a decrease in temperature at an interface known as the coldhead. A cryocooler can be used in a variety of ways to provide cooling to the windings of a coil. Some commercial devices operate the magnet in a cryogen bath but use a cryocooler to recondense boil-off helium gas thus creating a zero loss cryostat. Another method that can be used to minimise the coolant required involves using a cryocooler to remove heat from a cryogenic medium that is then used to cool the magnet coils through some form of heat exchanger. This can be accomplished using heat pipes [1] and thermosyphons, or by pumping the coolant through the cooling system [2].

It is possible to purely use conductive heat transfer to remove heat from the magnet coils to the coldhead of a cryocooler. Large temperature differences can occur across the thermal links and coil windings in such a system. This can cause poor stability of NbTi windings due to the small temperature margin between the operating temperature and critical temperature of the conductor. A 0.2MJ conduction cooled magnet used for superconducting magnetic energy storage (SMES) wound with a Nb_3Sn conductor has been successfully tested [3]. The higher critical temperature of Nb_3Sn (18.3K) compared to NbTi (9.2K) means that when the temperature difference between the coil and coldhead is accounted for Nb_3Sn coils can still operate at a sufficiently high current density. HTS coils suffer less from temperature differences in the coil winding because they have the ability to operate over a wide temperature range and are therefore suited to conduction cooling. As discussed

in chapter 2 it is expected that the quench behaviour will vary greatly over the wide temperature range which HTS coils operate.

Due to the tape-like geometry of (BiPb)2223 conductors it is easier to wind coils that are only one turn thick in the axial direction known as pancake coils. Magnets can be constructed by stacking multiple pancake coils and connecting the coils in series. It is also possible, though more difficult, to wind solenoids with tape conductors. The heat transfer in a section of a long potted solenoid can be simulated by a pancake coil cooled at its inner and outer boundaries. Thermal stability and quench propagation measurements performed on a boundary cooled pancake coil are therefore relevant to both solenoids and pancake coils.

3.2 Objectives

To enable the investigation of quenching in HTS pancake coils specialist apparatus had to be designed, manufactured and tested. The requirements for the apparatus were, firstly to provide stable operating conditions for a HTS coil over a wide temperature range and, secondly to initiate and measure the formation and propagation of a quench. To meet these objectives it was decided to use a single stage cryocooler with cooling to the coil provided solely by conduction. These choices were dictated partly by the desire to gain practical experience in the area of conduction cooling and partly by imposed economic constraints. An additional requirement was for the design of the conduction cooling system to be modular so that it could easily be transferred to another cryocooler in future work.

3.3 Cryostat design and apparatus layout

The conceptual design of the apparatus is shown in Figure 3.1. The pancake coil to be tested is cooled by conduction using a single stage cryocooler and current is applied to the coil using a combination of resistive and HTS current leads. Internal liquid nitrogen vessels provide cooling to the current leads, conduction cooled shield, and act as a constant temperature source for the reference junctions of the thermocouples that are used to

measure the temperatures in the coil. The entire apparatus is enclosed in a vacuum chamber necessitating vacuum leadthroughs for the current leads and instrumentation. In Figure 3.1 only one current lead is shown for clarity but two are needed, one for current into the coil and one for current out.

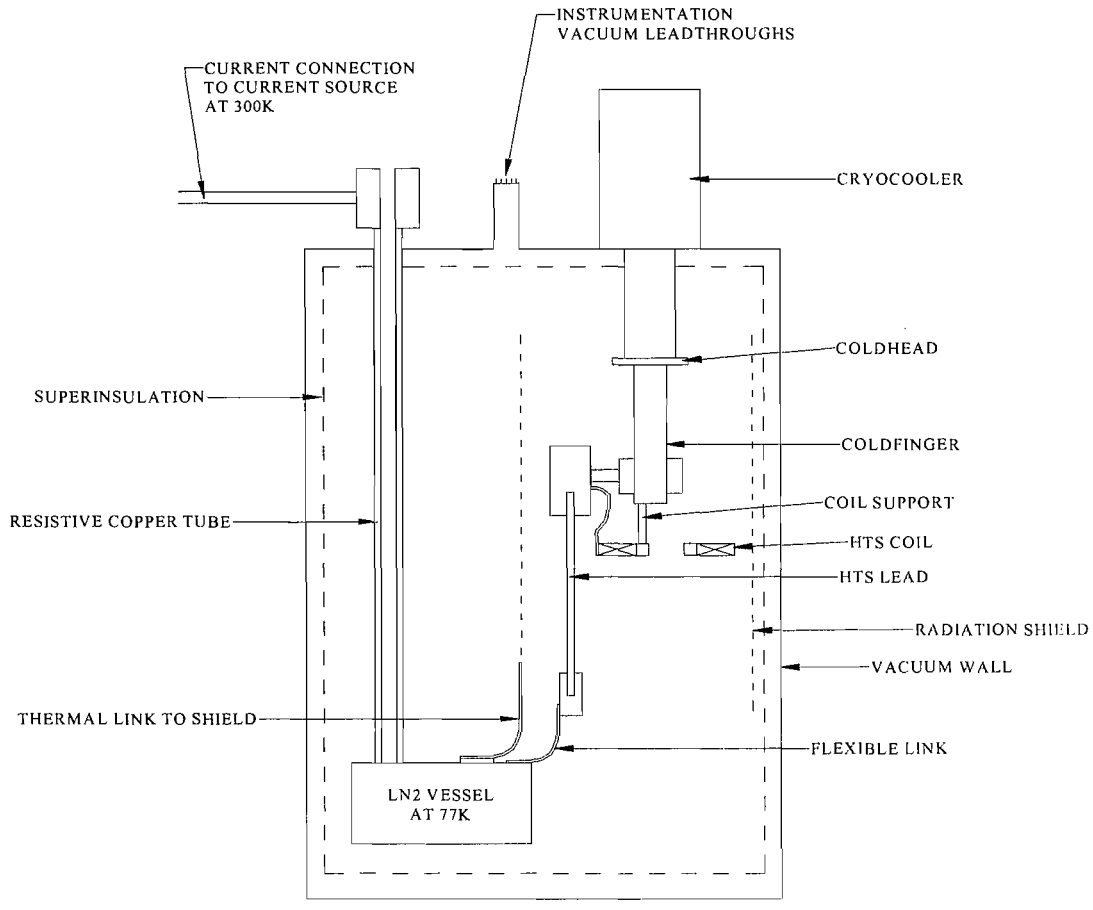

Figure 3.1: Conceptual design of the quench apparatus

3.3.1 Cryogenic design

Cryocooler

The cryostat was designed to incorporate an existing single stage cryocooler (Leybold RGS 30-T). The cryocooler must be operated in a vacuum below approximately $1x10^{-5}$ mbar to minimise freezing of gases onto the coldhead and heat transfer through the vacuum space.

Both of these mechanisms add heat loads to the coldhead of the cryocooler thereby reducing the minimum temperature that can be obtained. To achieve the desired level of vacuum all seals and fittings used on the cryostat were checked for leaks before operation of the apparatus. A copper shield was placed around the coldhead to minimise heat leak due to radiation. The shield was conduction cooled by thermal links to internal liquid nitrogen vessels and wrapped with superinsulation to reduce radiated heat leak from the cryostat outer walls. The cooling power as a function of operating temperature, known as the load curve, of the cryocooler was measured with no coil or current leads attached. A constant heater power was applied to the coldhead using a thin film heater, the coldhead was left to thermally stabilise, and the coldhead temperature was measured with a silicon diode thermometer. The temperature of the conduction cooled shield was monitored with a thin film platinum resistance thermometer during the measurement of the load curve. To observe the effect of radiation heat leak on the coldhead temperature two load curve measurements were obtained, one with the shield at 130K and one with the shield at 280K. The two load curves are shown in Figure 3.2. It can be seen that the cooled shield intercepts approximately 2.5W of radiated heat and this reduces the coldhead temperature by a further 2K.

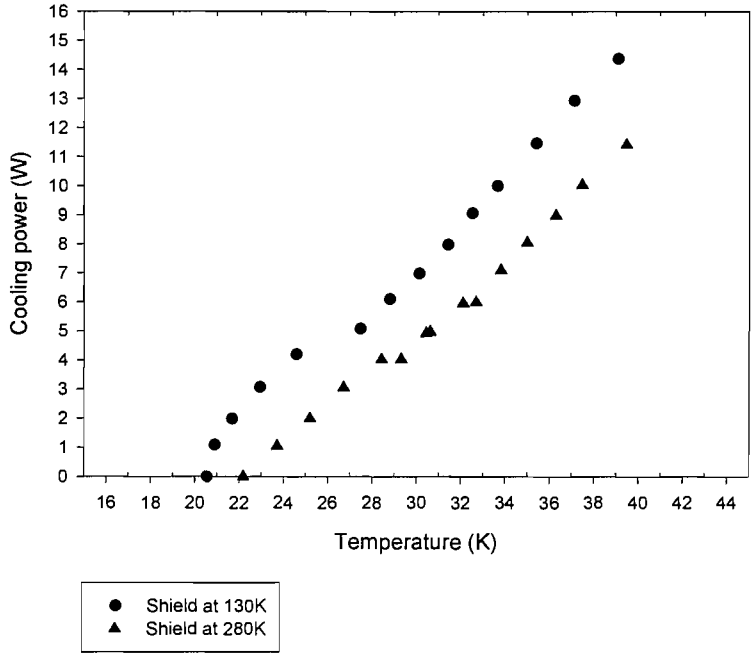

Figure 3.2: Cryocooler load curves showing the effect of the radiation shield

Internal liquid nitrogen vessels

Liquid nitrogen vessels operating at 77K are located between the resistive current leads and HTS leads. These vessels provide cooling for the resistive leads and conduction cooled radiation shield. They also maintain a stable temperature for the warm end of the HTS leads and sustain a stable reference temperature for differential thermocouple instrumentation.

Coil cooling conditions

The cooling and electrical connections to the pancake coil are combined in an attempt to simplify the coil design. This is possible because it is required that the coil is cooled from its inner and outer boundaries to simulate the heat transfer characteristics in a long potted solenoid [4].

3.3.2 Mechanical design

Thermal contraction

Differential thermal contraction produces stresses that can cause degradation of the transport properties of the HTS leads and mechanical failure of other parts of the apparatus. A flexible electrical and thermal link was incorporated between the liquid nitrogen vessels and the HTS lead to allow for differential thermal contraction. Flexibility in the design also aids assembly by allowing for a small amount of misalignment.

Coil mounting

The small mass of the coil meant it could be supported from the coldhead. In larger conduction cooled coils [3] low thermal conductivity supports are used to mount the coil directly from the cryostat. These supports are normally made of glass or carbon fibre.

3.3.3 Electrical design

The 'Zerome Hercules' (BiPb)2223 conductor produced by Nordic Superconductor technologies (NST) was used to wind the coil, the details of which are shown in Table 3.1. The maximum current that the apparatus was required to supply to the coil was calculated

using data from temperature dependent normalized critical current measurements for short conductor samples in self field [5], as shown in Figure 3.3. Also shown in Figure 3.3 are measurements taken 'in-house' [6] that correlate with the results from the literature. A coil operating temperature of 30K was designated to give an achievable temperature difference between the coldhead and the coil of approximately 8K. The maximum current required was calculated as 300A by allowing for a large overcurrent margin. The decrease in critical current due to magnetic field and winding effects was not accounted for because of uncertainties in predicting these effects at the concept stage.

Characteristic	Specification
Superconductor	(BiPb)2223
Number of filaments	37
Stabilising matrix	Interfilaments: Ag Outer sheath: 0.1MgNi-Ag alloy
SC fill factor	~27%
Tape dimensions	4.1mm x 0.25mm
I_C	60A at 77K (1μV/cm) self field

Table 3.1: Conductor specification

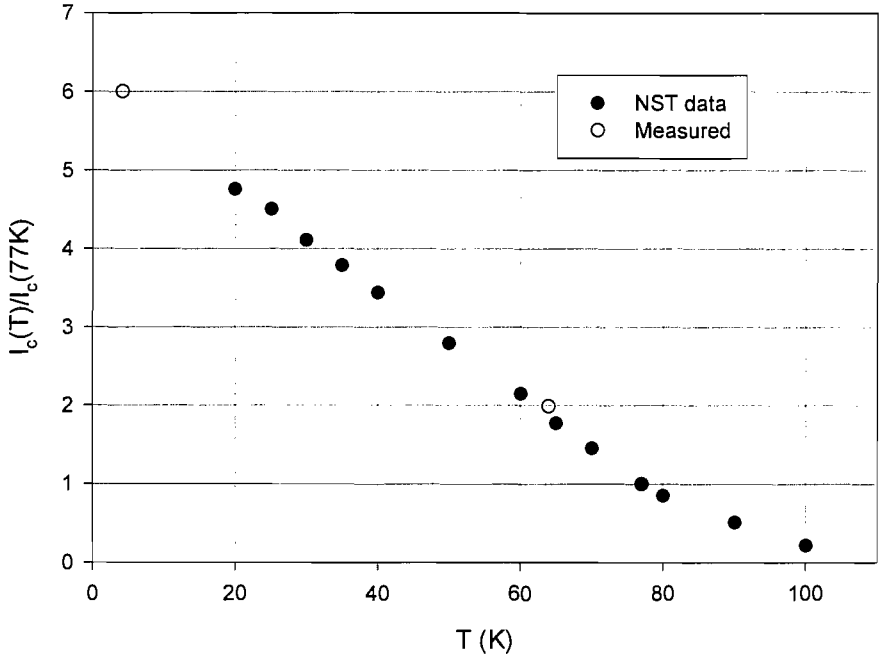

Figure 3.3: Temperature dependent critical current characteristics of the NST 'Zerome Hercules' tape

3.4 Resistive current leads

3.4.1 Optimisation

The resistive current leads transfer current from outside of the cryostat to the internal liquid nitrogen vessels. The liquid nitrogen vessels ensure a stable operating temperature for both the cold end of the resistive leads and the warm end of the HTS leads. Each resistive current lead consists of a phosphorus deoxidised copper tube that is cooled both by conduction to the liquid nitrogen vessel and by convective cooling from the nitrogen boil-off gas. As discussed in Chapter 1 the Wiedemann-Franz law dictates that there is a minimum heat leak for a given current, this can be found by optimising the current lead geometry. Equation 3.1, a 1-dimensional steady state heat balance equation, can be formed

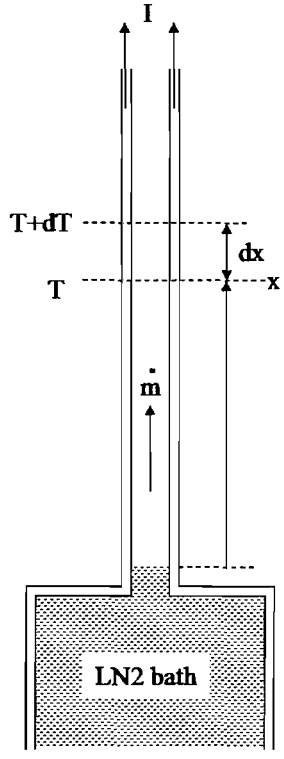

Figure 3.4: Model of current leads

Parameter	Designation
k	Thermal conductivity of current lead material [$W.m^{-1}.K^{-1}$]
A	Current lead cross-sectional area [m^2]
x	Distance from nitrogen bath [m]
T	Temperature [K]
f	Efficiency of heat transfer from boil off gas to lead [dimensionless]
$\dot{m}$	Mass flow rate of boil off gas [$kg.s^{-1}$]
C_p	Specific heat of nitrogen gas [$J.kg^{-1}.K^{-1}$]
I	Operating current [A]
ρ	Resistivity of lead material [Ω.m]

Table 3.2: Nomenclature

$$\frac{d}{dx}\left(k(T).A.\frac{dT}{dx}\right) - f.\dot{m}.C_p(T).\frac{dT}{dx} + \frac{I^2.\rho(T)}{A} = 0 \quad [J] \qquad \textbf{Equation 3.1}$$

representing the heat flow to and from the unit cell of the gas cooled current lead as shown in Figure 3.4 [7]. The first term on the left hand side of Equation 3.1 represents the net conduction heat flow into the unit cell, the middle term represents the cooling of the unit cell due to nitrogen boil off gas, and the last term is the heat generation due to resistive losses. The nomenclature for Equation 3.1 is detailed in Table 3.2.

Equation 3.1 was solved using a numerical solver that is part of the 'MathCad' software package. The solution was obtained by manually adjusting the temperature gradient at the nitrogen bath to obtain a temperature of 300K at the other end of the lead. A number of iterations were completed before a solution was converged upon; at each iteration the mass flow rate of the boil off gas was modified dependent on the heat leak to the nitrogen bath. For all calculations the current lead length was set at 0.7m and the heat transfer efficiency, f, was set to 1. The calculated heat leak into the liquid nitrogen bath as a function of the cross-sectional area of the current leads is shown in Figure 3.5 for two cases, one at the maximum operating current of 300A and another at zero operating current.

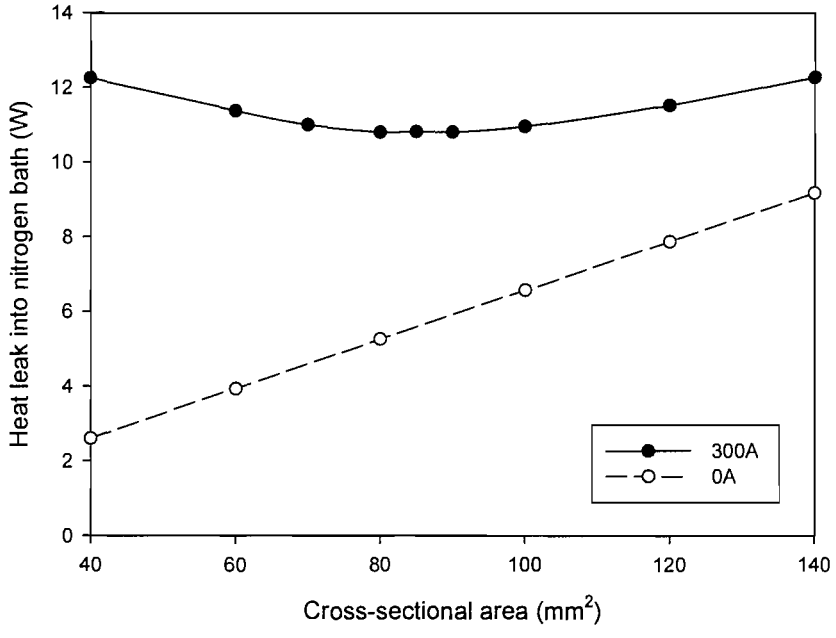

Figure 3.5: Calculated heat leak into the nitrogen bath

It can be seen that the optimum cross-sectional area for the lead length of 0.7m at 300A is 80mm^2. The apparatus only has to sustain the operating current for a short period of time. However it will spend long periods at zero operating current, for example when the apparatus is thermally stabilising after cooldown. It was therefore decided to design the current leads with a non-optimum heat leak at maximum operating current but which provided a comparably lower heat leak at zero operating current. When operating the current leads at non-optimum conditions it is important to identify the maximum temperature of the leads, the temperature profiles of 3 non-optimum designs are compared to the optimum design in Figure 3.6. A peak in the temperature profile of the non-optimised current leads occurs 0.5m from the liquid nitrogen bath, this temperature peak increases as the cross sectional area of the current leads is reduced. The maximum allowable temperature was set at 380K so as not to degrade the performance of glued support brackets attached to the leads; therefore the area of each current lead was set at 50mm^2.

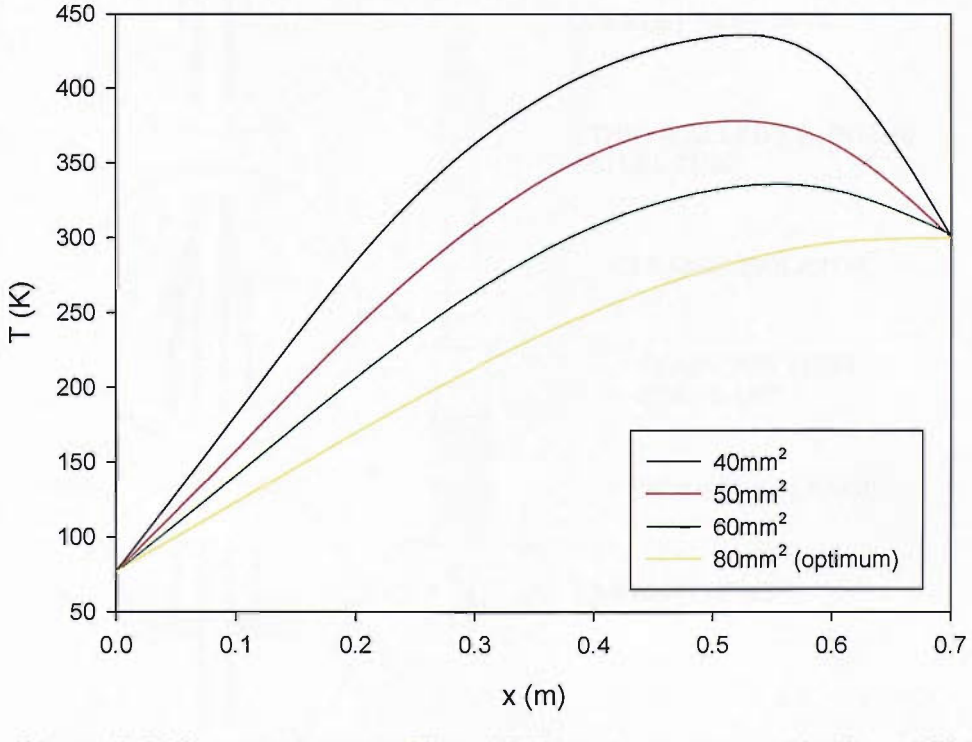

Figure 3.6: Temperature profiles of different area current leads at 300A

3.4.2 Manufacture of the resistive section

Electrical isolation and vacuum seal

The resistive sections were manufactured from copper tube enabling the liquid nitrogen vessels to be filled. The resistive current leads had to pass through the top flange whilst retaining the vacuum in the cryostat and also be electrically isolated from the cryostat; the assembly designed for this is shown in Figure 3.7. Ceramic isolators provide electrical isolation and Tufnol spacers ensure no shorting occurs between the current leads and the cryostat. To ensure the ceramic isolators were not thermally shocked during cooldown they were thermally isolated from the copper current lead by a thin walled stainless steel tube. All joints are hard soldered or welded and then leak tested, stainless steel standoffs were used to aid assembly.

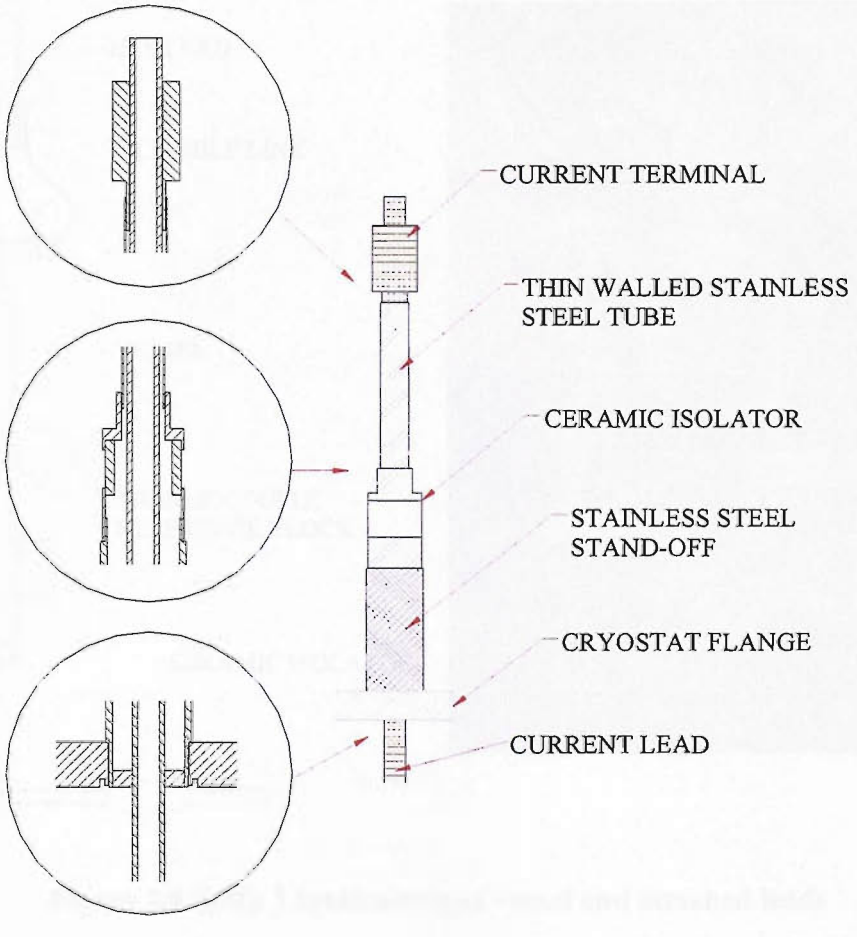

Figure 3.7: Top flange current lead transition

Internal Liquid Nitrogen vessels

The liquid nitrogen vessels that make up part of the resistive current lead assembly must each be electrically conductive but isolated from one another. The vessels were machined from copper bar with stainless steel assemblies hard soldered to the bottom of the vessels. To aid filling especially during cooldown the vessels were interlinked; the vessels could be filled through one lead and the boil off gas vented through the other. A ceramic isolator was placed in series with the interlinking tube to electrically isolate the two current carrying vessels but allow liquid nitrogen transfer. A drawing and photograph of the vessels and connecting leads are shown in Figure 3.8 and Figure 3.9 respectively. Conduction cooling links to the thermal shield are clamped around the periphery of the vessel and the thermocouple reference junction is shown as discussed in Section 3.8.2.

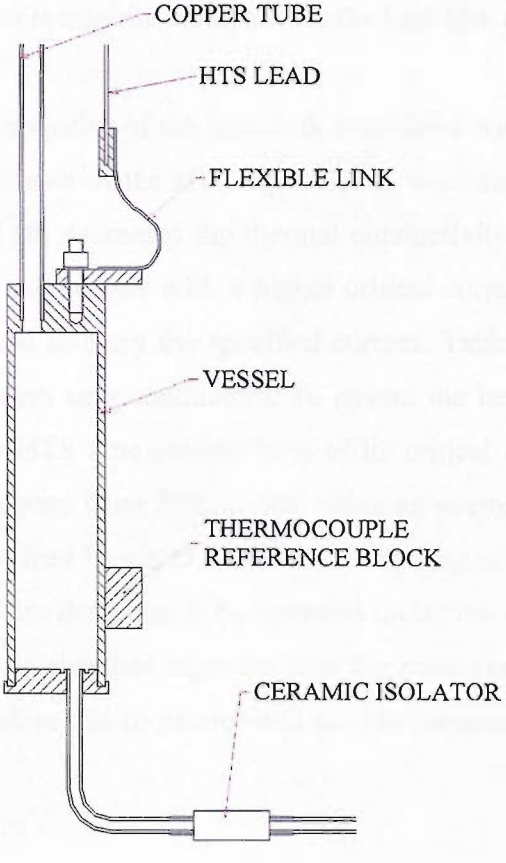

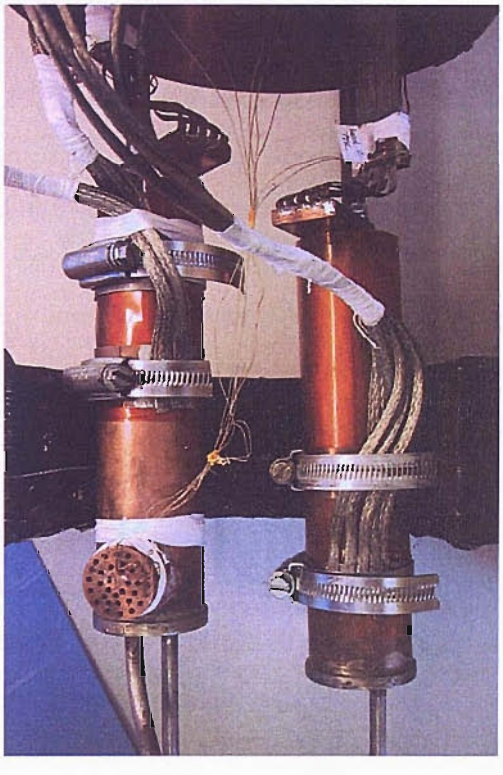

Figure 3.8 (left): Liquid nitrogen vessel and attached leads

Figure 3.9 (right): Fabricated liquid nitrogen vessel and attached leads

3.5 HTS current leads

3.5.1 Heat leak calculation

HTS current leads were used to transfer the current from the resistive section at 77K to the current lead sections at the coldhead temperature. If copper leads were used the heat leak to the coldhead would have been prohibitively large. HTS leads also have the benefit of limiting fluctuations of the coldhead temperature when the operational current is varied due to the almost zero heat generation of the conductors. The HTS leads were constructed using a proven technique developed at Southampton University that involves soldering (BiPb)2223 tapes to a stainless steel backing board that provides mechanical strength to the leads. The heat leak due to a 1mm thick stainless steel backing board is 0.03W per lead which is minimal compared to the heat leak associated with the HTS tapes.

The majority of the heat leak associated with HTS leads is due to heat conducted through the sheath of the HTS tapes. It has been shown that alloying the silver in the sheath with gold [8] decreases the thermal conductivity of the sheath material. It must also be noted that using tapes with a higher critical current can reduce heat leak because less tapes are needed to carry the specified current. Table 3.3 compares the heat leak associated with 3 different tape conductors. To ensure the leads did not quench they were designed so that each HTS tape carried 75% of its critical current at 77K. The conductive heat leak was calculated from 77K to 30K using an average thermal conductivity for the sheath material and a lead length of 0.12m. Joule heating of the HTS leads was assumed to be negligible as they are designed to be operated under the critical current. It was found that the NST Ag-Au 4% sheathed tapes transfer the rated current of 300A with the minimum heat leak and therefore this conductor was used to construct the HTS leads.

Tape	I_C* (A)	No. tapes for 300A**	Area of sheath (mm^2)	Average thermal conductivity 77K to 30K (W/m.K)	Conduction heat leak 77K to 30K per lead
NST Ag alloy sheath	60	7	0.7	400 [9]	0.80
NST Ag-Au 4%	40	10	0.7	100 [9]	0.27
ASC reinforced	115	4	0.7	400	0.46

* At 77K in self field
** Rounded up to the nearest integer

Table 3.3: Heat leak estimation for HTS leads

3.5.2 HTS lead fabrication

Each HTS lead consists of 10 lengths of 4%Au-Ag sheathed HTS tape soldered onto both sides of a pre-tinned stainless steel backing plate. This was done by first painting the tapes with Indalloy #5RA liquid soldering flux [10]. This flux becomes sticky on application and so the tapes can be stuck to the backing plate in the correct position. The flux is non-corrosive, non conductive and non-hydroscopic and therefore does not need to be cleaned off. The ends of the tapes were spot-soldered to the backing plate, the whole lead wrapped tightly with PTFE tape, and then placed in a furnace at 250°C for approximately 10minutes. The manufactured HTS lead can be seen in Figure 3.10, the 140mm length shown is to allow for current connections at each end.

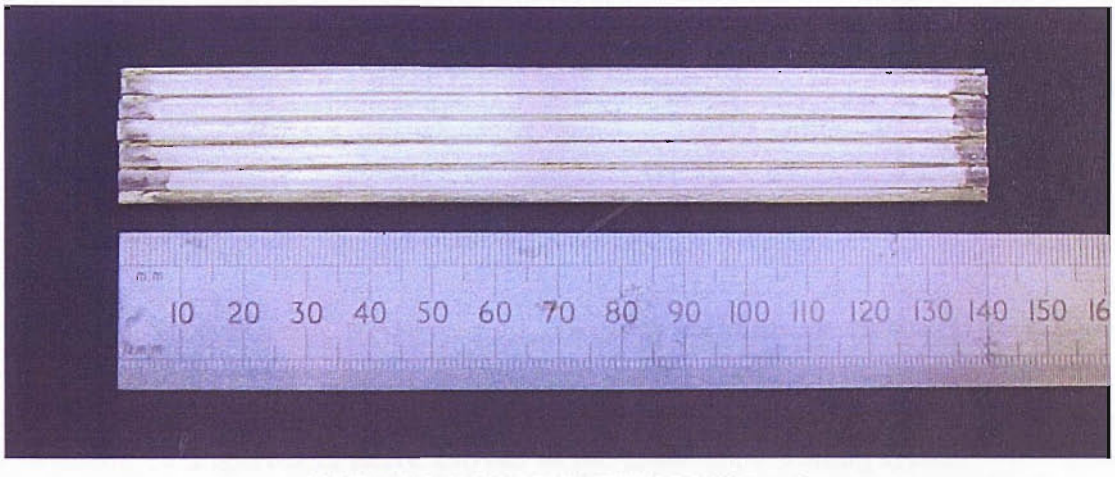

Figure 3.10: Manufactured HTS lead

3.6 Conduction cooling

The aim of the conduction cooling system was to maintain the boundaries of the coil at a stable temperature and to minimise the temperature drop between the coil and coldhead. It is important to minimise all heat loads and also to apply the heat loads directly to the coldhead, any heat loads applied to the coil or thermal links will cause a temperature difference between the coil and coldhead. The HTS leads were thermally anchored to the coldhead so that heat leak from the 77K section is intercepted before it affects the coil boundaries. The conduction cooling system designed is shown in Figure 3.11 only the links to the inner coil are shown for clarity. A thermal circuit representation of the system is shown in Figure 3.12; the symbols used are defined in Table 3.4. The apparatus was designed to be modular so that each module can be fabricated separately and then bolted together. This approach avoided complicated in-situ soldering but added additional thermal and electrical contact resistances at the bolted joints. The heat leaks and calculated temperature differences associated with the system are analysed below.

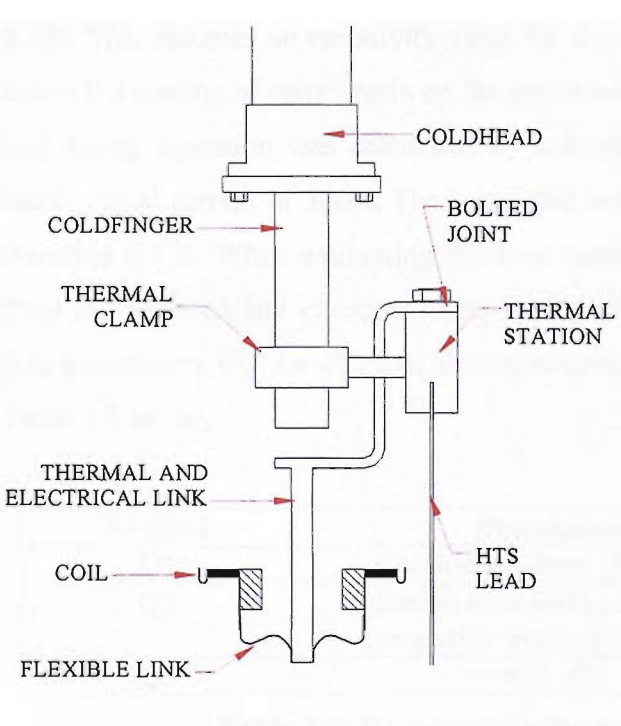

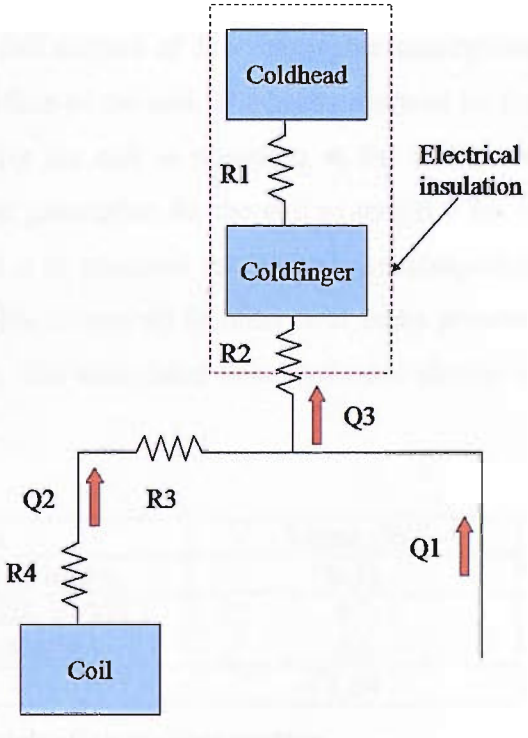

Figure 3.11 (left): Layout of the conduction cooling system

Figure 3.12 (right): Thermal circuit representation of the conduction cooling system

Symbol	Type	Description
R1	Thermal resistance	Coldhead to coldfinger
R2	Thermal resistance	Across electrical insulation
R3	Thermal resistance	Across bolted joints
R4	Thermal resistance	Across thermal links to the coil
Q1	Heat load	Conduction from HTS leads
Q2	Heat load	Radiation onto coil Heat generation in coil
Q3	Heat load	=Q1+Q2

Table 3.4: Thermal circuit symbol description

3.6.1 Heat loads to the conduction cooling system

The heat load on the coldhead due to conduction heat leak from the HTS leads (Q1) was calculated in Section 3.5.1 and found to be 0.54W for a pair of leads. The heat load into the coil during operation (Q2) comprises of the radiation heat leak onto the coil surface and the heat generated by the coil when operating near the critical current. The radiation heat leak onto the coil surface from the 135K shield with the coil operating at 30K is calculated as 0.2W. This assumes an emissivity value for the coil surface of 1, a reasonable assumption due to the coating of epoxy resin on the entire surface of the coil. The heat generated by the coil during operation was calculated by assuming the coil is operating at the maximum rated critical current of 300A. The calculated heat generation for the coil of length 9.8m is therefore 0.3W. When estimating the heat loads it is assumed that the power dissipation from the soldered and clamped joints is negligible compared to other heat leaks present, this assumption will be checked during testing. The calculated heat loads are shown in Table 3.5 below.

Symbol	Description	Value (W)
Q1	Conduction from HTS leads	0.54
Q2	Radiation onto coil (135K to 30K) Generation in coil (300A at I_C)	0.2 0.3
Q3	=Q1+Q2	1.04

Table 3.5: Heat loads to the conduction cooling system

3.6.2 Temperature difference across the thermal link (R4)

The links between the thermal station and the coil boundaries are used to provide both cooling and current to the coil. Two links are needed, one to the coil inner boundary and one to the coil outer boundary. The two links had to be routed around other parts of the apparatus, be easy to connect to the coil, and incorporate a flexible link to account for differential thermal contraction. Flexible braids were first considered as a suitable thermal link, however it was found that a 5mm by 0.7mm ($3.5mm^2$) braid only has an area for conduction of 2 mm^2 [11] due to the woven construction. It was estimated that a total of 100 braids would be required to give a temperature difference of 1K over the 200mm length required; an impractical proposition for assembly. A more practical option was to route a solid copper bar from each thermal station to near the inner and outer boundaries of the coil. The solid thermal links were annealed after cold working operations so as not to degrade the thermal conductivity of the material. A short braided section, consisting of 20 braids 50mm long, connected the copper bar with the coil allowing for flexibility during assembly and operation. The temperature drop across both the thermal links is calculated in Table 3.6, and it can be seen that the braids contribute towards the majority of the temperature drop. The fabricated thermal links to the inner and outer boundaries are shown in Figure 3.13 and Figure 3.14 respectively. The braids are left long to aid mounting of the coil into the apparatus.

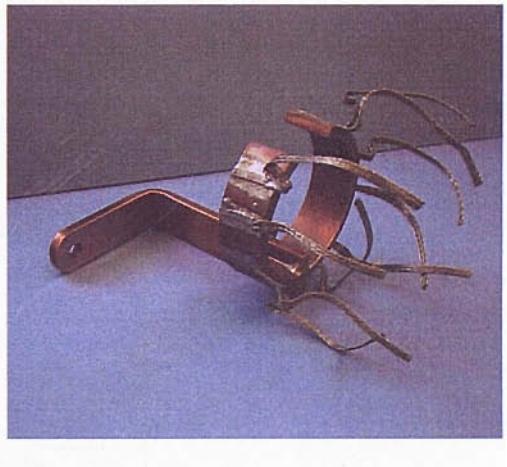

Figure 3.13 (left): Inner connection to the coil

Figure 3.14 (right): Outer connection to the coil

Item	Total Area (mm^2)	Q (W)	Length (m)	K_{av} (W/m.K)	ΔT (K)
Solid links	250	0.5	0.15	600	0.5
Flexible links	40	0.5	0.05	200	3.1
					TOTAL: 3.6K

Table 3.6: Temperature drop across thermal links

3.6.3 Temperature differences due to thermal contact resistances

The unevenness of real surfaces is the basic cause of a thermal contact (or boundary) resistance at the interface between two surfaces [12]. Firstly, heat flow is restricted macroscopically to the areas of the surface that are in contact and it is therefore important to ensure contacting surfaces are flat. Secondly heat flow is restricted microscopically to the point contacts of the peaks characteristic of the surface roughness. The thermal contact resistance can therefore be reduced by polishing the surfaces to reduce their surface roughness and by adding a medium between the surfaces, such as Apezion-N grease, to fill the gaps caused by the surface roughness. Thick oxide layers on the contacting surfaces can significantly increase the thermal contact resistance due to the additional thermal barrier imposed at the interface, whilst even thin oxide layers can increase the electrical contact resistance of the joint appreciably. Each clamped joint is evaluated below and the temperature drop across the interface estimated.

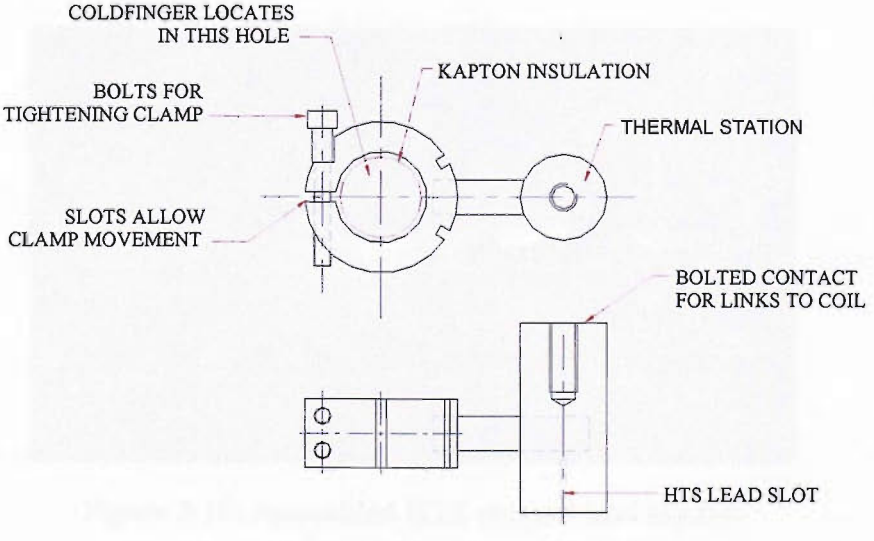

Figure 3.15: Conduction cooled clamp

Coldhead to coldfinger (R1)

A copper to copper interface filled with Apezion-N grease exists between the coldhead and coldfinger with the surfaces clamped together using stainless steel bolts. Invar washers are placed under the bolt heads to compensate for the differential contraction between the stainless steel bolts and copper flanges during cooldown. This is to ensure the bolts are always kept in tension and therefore the surfaces are clamped together at all operating temperatures.

Electrically isolated thermal clamp (R2)

To electrically isolate the cryocooler from the conduction cooling system a Kapton sheath is placed around the coldfinger. A clamp is then located over the coldfinger and tightened. The clamp incorporates a thermal 'station' into which the cold end of the HTS lead is soldered, and onto which a bolted contact provides a terminal for connecting both thermal and electrical links to the coil. A drawing of the clamp and attached thermal station is shown in Figure 3.15 and the assembled HTS lead and clamp module is shown in Figure 3.16. The Kapton adds an additional thermal resistance across which heat must flow; this additional temperature drop is considered in the temperature drop calculation as shown in Table 3.7 below. Apezion-N grease is applied to all surfaces to decrease the thermal contact resistance at the interface.

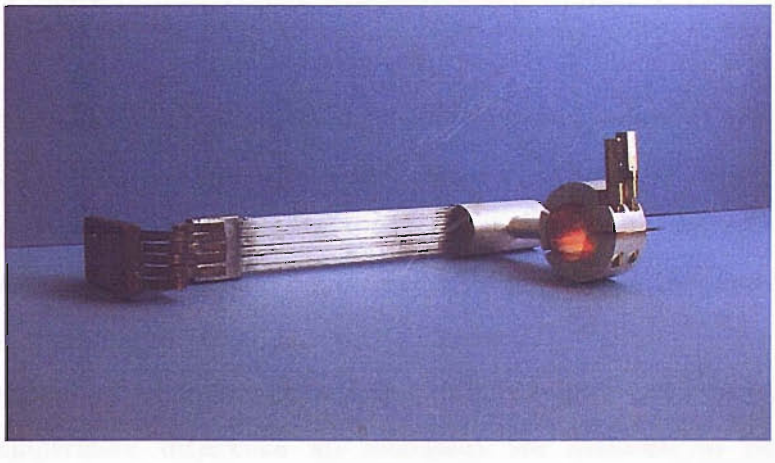

Figure 3.16: Assembled HTS current lead module

Bolted contact on the thermal station (R3)

This interface consists of two contacting copper surfaces that connect both the thermal and electrical links. Apiezon-N grease was not used because this may have adversely affected the electrical resistivity of the joint by coating both surfaces with grease. The contact resistance was minimised by ensuring all joints were polished flat and free of an oxide layer before installation. It was difficult to remove the oxide layer on the surface of the thermal station after it was fabricated so the contact was plated with silver to reduce oxidisation. The thermal contact resistance of dry contacts may vary by a factor of 100 according to the surface preparation [12] and therefore care was taken to be consistent with the surface preparation of both sets of contacts.

3.6.4 Estimated temperature drop due to thermal contact resistances

The thermal boundary resistance R_H per unit area of the contact [$m^2.K.W^{-1}$] is defined as the ratio of the temperature discontinuity at the interface and the heat power per unit area flowing across the interface [12] as shown in Equation 3.2. Where ΔT [K] is the discontinuous temperature difference at the interface of the two materials and Q [W] is the heat flow across the area A_C [m^2] of the contacting interface.

$$R_H = \Delta T \Big/ \left(\frac{Q}{A_C} \right) \quad [m^2.K.W^{-1}] \qquad \textbf{Equation 3.2}$$

The temperature difference across each interface was calculated using Equation 3.2 and reported values for R_H [12] as shown in Table 3.7. Upper and lower limits for ΔT are quoted to encompass the differences that can occur due to surface preparation. The maximum temperature difference was of interest and therefore the heat flow produced by the coil when operating at 300A, as shown in Table 3.5, was used in the calculations. The thermal contact resistance increases as temperature decreases and therefore to calculate the maximum temperature difference all interfaces are assumed to be at a minimum temperature of 30K. For the interface at the electrically insulating clamp (R2) a Cu/

Apezion-N/ Cu joint is considered with an additional thermal path in series consisting of a layer of 70μm Kapton.

It can be seen that the total temperature drop across the joints is dominated by the temperature drop across the bolted contact and that a high degree of uncertainty exists over the temperature drop across this bolted interface. The maximum total estimated difference between the coldhead and coil is obtained by summing the temperature drops across the thermal links and the temperature drops due to the thermal contact resistances. A total temperature drop of between 4.6K and 12.2K was estimated. Accounting for heat loads in Table 3.5, and referring to the cryocooler load curve in Figure 3.2, the minimum estimated temperature of the coil boundaries is expected to be between 26K and 33K.

Designation	Interface	R_H [12] (m^2.K/W)	A_C (m^2)	Q (W)	ΔT (K)
R1 Coldhead to coldfinger	Cu/ Apezion-N/Cu	0.25e-3 to 2.5e-3	4.4e-3	1.04	0.06→0.6
R2 Electrical insulation	Cu/ Apezion-N/Cu + Kapton, 70μm thick	0.25e-3 to 2.5e-3	1.6e-3	0.52	0.08→0.8 + 0.2
R3 Bolted contact	Cu/Ag plate/Cu	1.3e-3 to 12.5e-3	4.4e-4	0.25	0.7 →7.0

Table 3.7: ΔT calculation

3.7 Final apparatus assembly

The assembled apparatus is shown in Figure 3.17. For clarity the right hand current tube, the vacuum port, and the thermal links to the conduction cooled shield are not shown on the drawing.

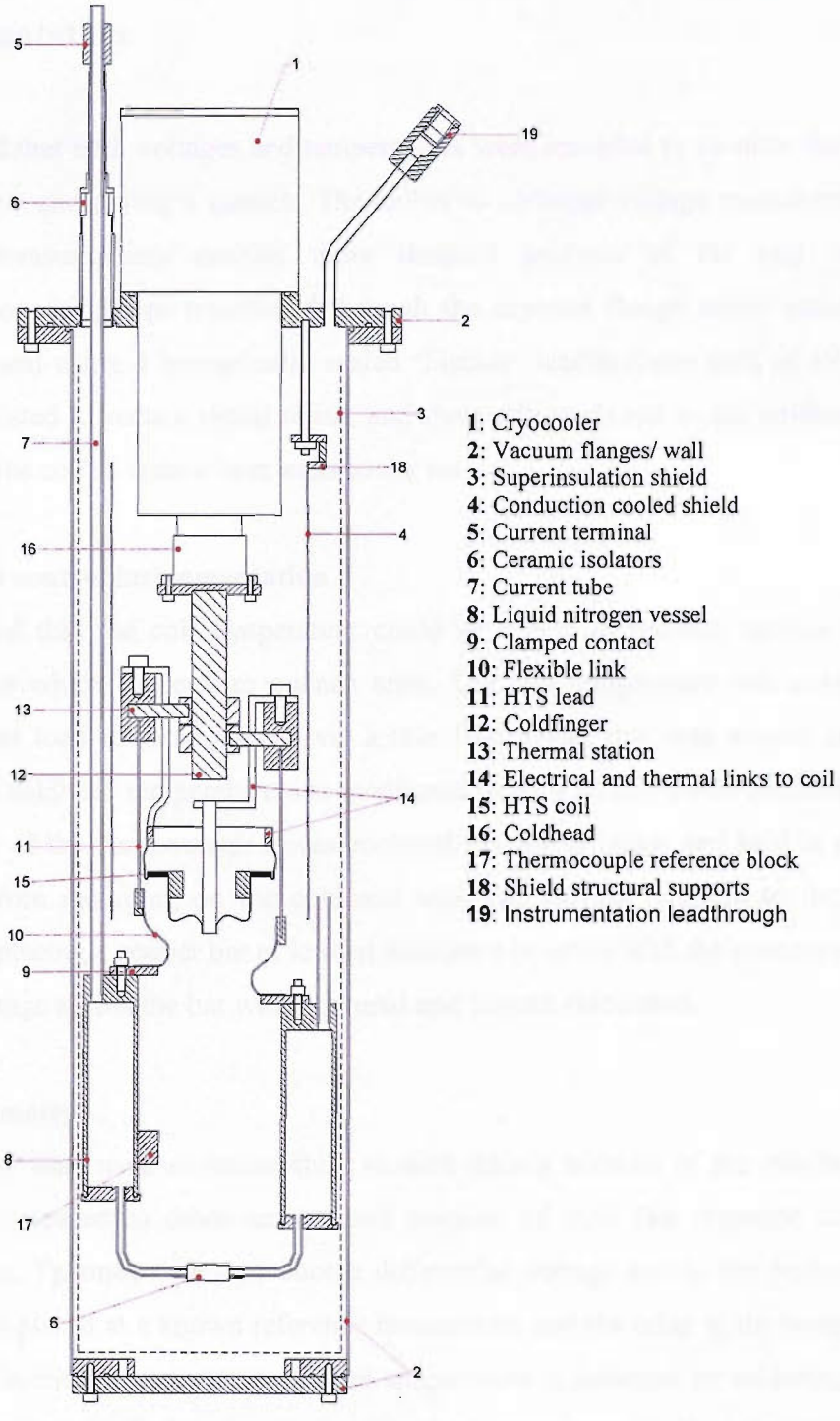

Figure 3.17: Apparatus final assembly

3.8 Instrumentation

It was required that both voltages and temperatures were recorded to monitor the coil both during operation and during a quench. The ability to correlate voltage measurements with temperature measurements enables more detailed analysis of the coil behaviour. Instrumentation wiring was transferred through the cryostat flange whilst maintaining a vacuum tight seal using 4 hermetically sealed 'Fischer' leadthroughs each of 19 pins. All wiring was twisted to reduce signal noise, and thermally anchored to the coldhead before connecting to the coil to reduce heat leaks to the coil.

3.8.1 Cryostat control instrumentation

It was essential that the coil temperature could be varied to provide various operating temperatures at which to perform quench tests. The coil temperature was controlled by applying a heat load to the coldhead via a thin film heater that was wound around the coldhead. The coldhead temperature was monitored using a silicon diode thermometer, due to the fragility of the thermometer it was enclosed in a silver jacket and held in place with 'Ecobond' before mounting on the coldhead with GE varnish. Current to the coil was monitored by placing a copper bar of known resistance in series with the connecting current leads. The voltage across the bar was measured and current calculated.

3.8.2 Thermometry

Thermocouples were used as temperature sensors mainly because of the minimal cost of each sensor compared to other sensors and because of their fast response to transient thermal effects. Thermocouples produce a differential voltage due to the Seebeck effect, one junction is placed at a known reference temperature and the other at the temperature to be measured. In the apparatus the reference temperature is achieved by soldering a copper block with multiple drilled holes to the liquid nitrogen vessels. One junction of each thermocouple is electrically insulated with Ecobond and it is then placed in a hole in the reference block that has been filled with Apezion-N grease to provide good thermal contact. The sensitivities and cost of thermocouples commonly used at cryogenic temperatures are

detailed in Table 3.8; two thermocouples of interest are Type E and Type T because of their low cost and adequate sensitivity.

Thermocouple type	Materials	Sensitivity at 30K (μV/K) [13]	Cost, £/m
E	Chromel-Constantan	12.1	0.75 [14]
T	Copper-Constantan	8.0	0.75 [14]
K	Chromel-Alumel	6.4	0.75 [14]
-	Chromel-Au/Fe(0.07%)	16.6	27 [13]

Table 3.8: Thermocouple options

Care must be taken with the thermocouple output wiring because temperature gradients at dissimilar metal junctions produce an error voltage in the measurement signal. Large errors in the measured signal are produced when measuring cryogenic temperatures with a dissimilar metal junction at room temperature because the thermoelectric sensitivity at room temperature is many times higher than at cryogenic temperatures. All thermocouple wiring junctions must therefore be maintained at a constant temperature when two dissimilar metals are joined. Temperature gradients at the vacuum leadthroughs are difficult to minimise and therefore the material of the connecting wires and pins have to be matched. Leadthroughs with chromel pins matching the type K thermocouple wires are available but are prohibitively expensive. It was therefore decided to use standard vacuum leadthroughs containing copper pins with Type T (Copper-Constantan) thermocouples to negate the need for any additional jointing inside the cryostat.

Standard curves can be used to convert the thermocouple voltage signal to a temperature measurement however the voltage signal can be influenced by the lengths of the connecting wiring and also strain effects. To obtain accurate temperature readings all thermocouples used were fabricated with connecting wiring of the same length and one thermocouple was calibrated in-situ. One junction of the thermocouple was fixed with epoxy resin into a copper block mounted to the coldhead and the other junction fixed with epoxy resin into the reference block that was maintained at 77K. The measured thermocouple output voltage is shown in Figure 3.18. The sensitivity of the thermocouple derived from the output voltage is shown in Figure 3.19, also shown are sensitivity values quoted by Lake Shore

Cryotronics Inc [13], a leading cryogenic sensor manufacturer. It can be seen that the measured sensitivities are verified by the quoted values.

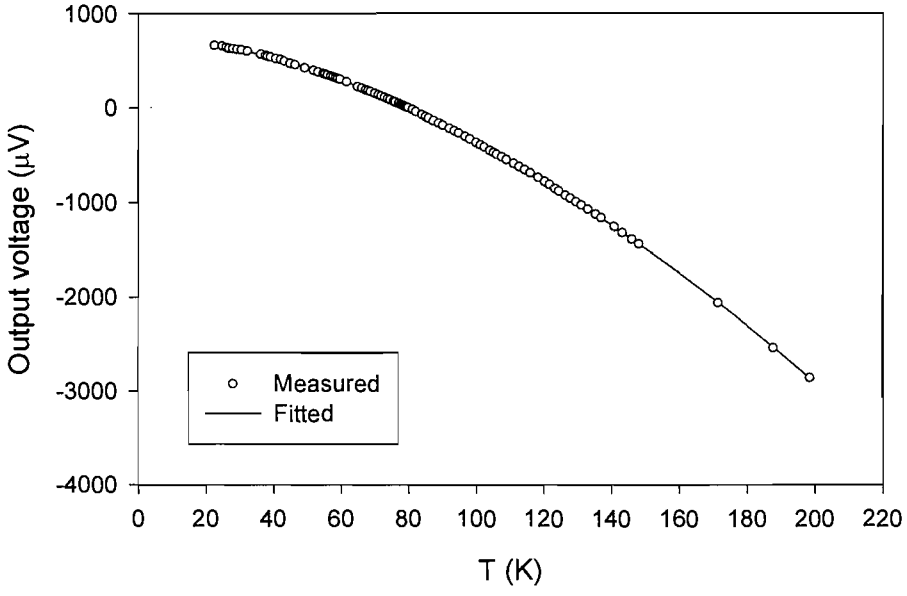

Figure 3.18: Type T output voltage as a function of temperature, reference junction maintained at 77K

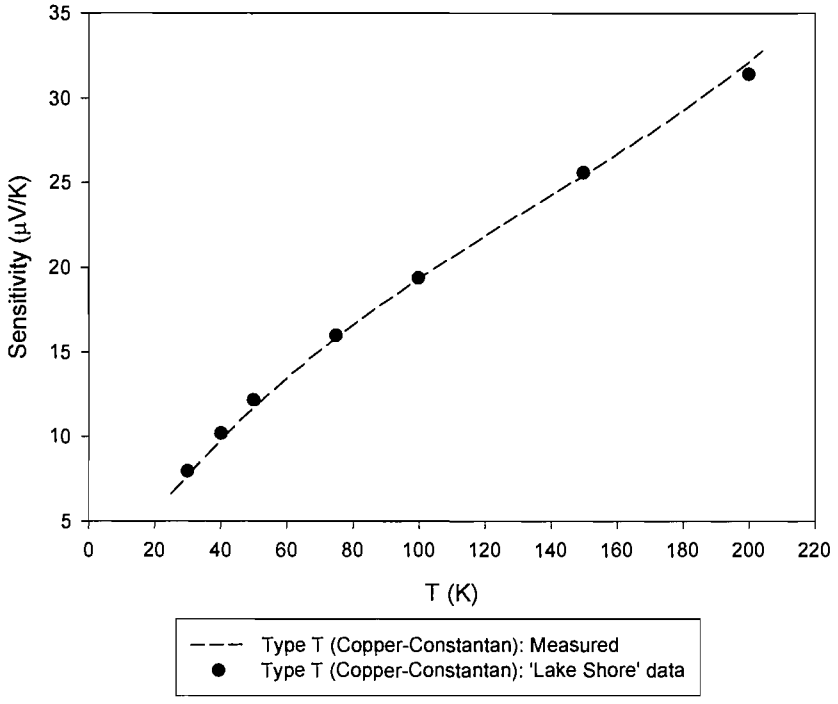

Figure 3.19: Type T calculated sensitivity as a function of temperature, reference junction maintained at 77K

3.8.3 Measurement and acquisition system

It was required that the transient voltage and temperature signals from the thermocouples and voltage taps were recorded. Thermocouples have low voltage sensitivity compared to other temperature sensors such as silicon diode thermometers and therefore to distinguish the input signal from background noise the thermocouple signals have to be conditioned by amplifying them before they are fed into a data acquisition device. A 32 channel amplifier and data acquisition system was purchased from 'National Instruments'. The system layout is shown in Figure 3.20 and is part of the Signal Conditioning eXtensions Instrumentation (SCXI) range [15]. The system has the capability to perform amplification on separate channels allowing each channel to be tuned to achieve maximum signal accuracy. Diode and quench voltages (magnitude of volts) can therefore be measured with the same device used to measure thermocouple voltages (magnitude of mV). The system provides acquisition speeds of up to 5000Hz on each of the 32 channels. To display and record the measured data a program was written using the 'LabView 7' software package. The program was used to select the signals to be acquired, the gain for each channel and the acquisition speed. A filter was included in the program to reduce the 50Hz noise picked up by the HTS coil affecting the signal from the voltage taps.

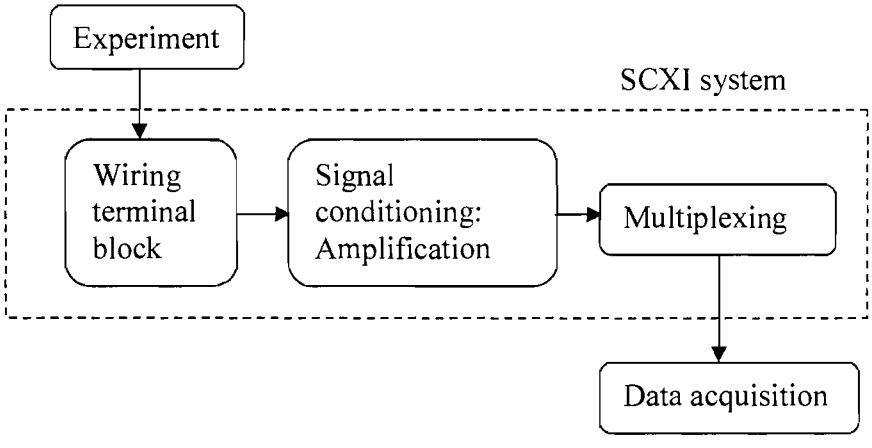

Figure 3.20: Data acquisition system layout

3.9 Testing

3.9.1 Apparatus cooldown

With the liquid nitrogen vessels filled, the cryocooler was switched on and the temperature of the coldhead recorded. This test was completed with and without the coil and thermal links connected and the results shown in Figure 3.21. It can be seen that the additional thermal mass of the coil and thermal links increases the cooldown time from ~1 hour to ~3hours. The cooldown time is short enough to cool the coil and perform a series of quench measurements in one day if needed.

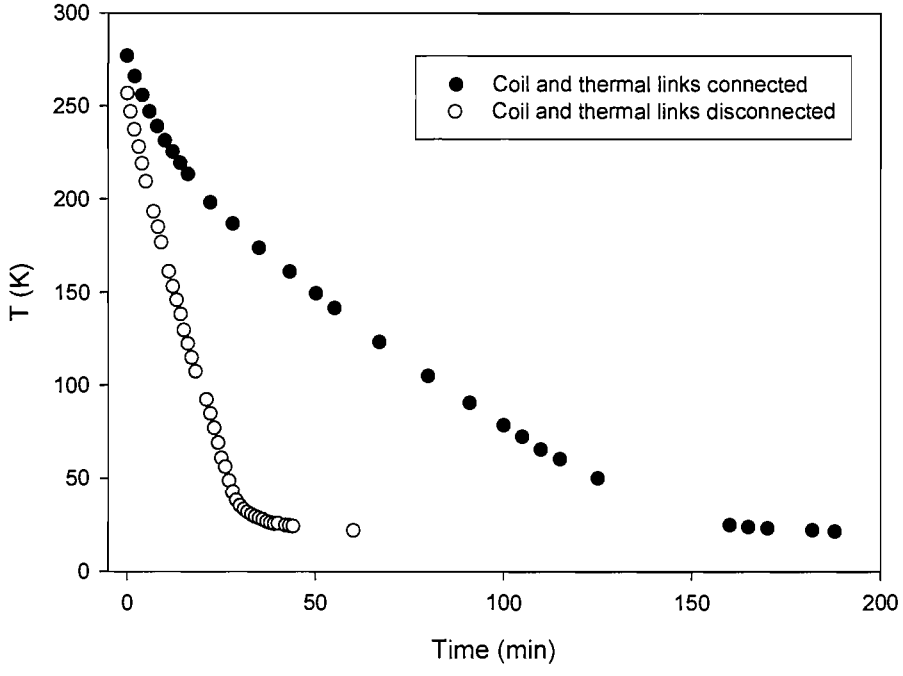

Figure 3.21: Apparatus cooldown

3.9.2 Electrical characterisation of the current leads

To electrically characterise each joint the current leads were shorted by connecting a copper link between each thermal station. Voltage taps were applied across each joint and also across a 50mm section of both HTS current leads, the voltage tap positioning is detailed in Figure 3.22 and the construction and designation of each joint listed in Table 3.9. The current-voltage (I-V) characteristics of each joint were measured up to 300A with zero heat

applied to the coldhead heater and the results shown in Figure 3.23. Particular care was taken with the HTS leads on the first test run to ensure an overcurrent quench of the leads was not initiated. The temperature of the coldhead during the I-V test is discussed in section 3.9.3 below.

Joint	Construction	Notes
V_{FLEX} to $V_{HTS\ HT}$	Cu-solder*-HTS lead	Soldered
$V_{HTS\ LT}$ to V_{STA}	HTS lead-solder*-Ag plating-Cu	Soldered
V_{STA} to V_{CLA}	Cu-Ag plate-Cu	Bolted, torque=34Nm

*Solder: 2% Ag, 62% Sn, 36% Pb

Table 3.9: Joint construction details

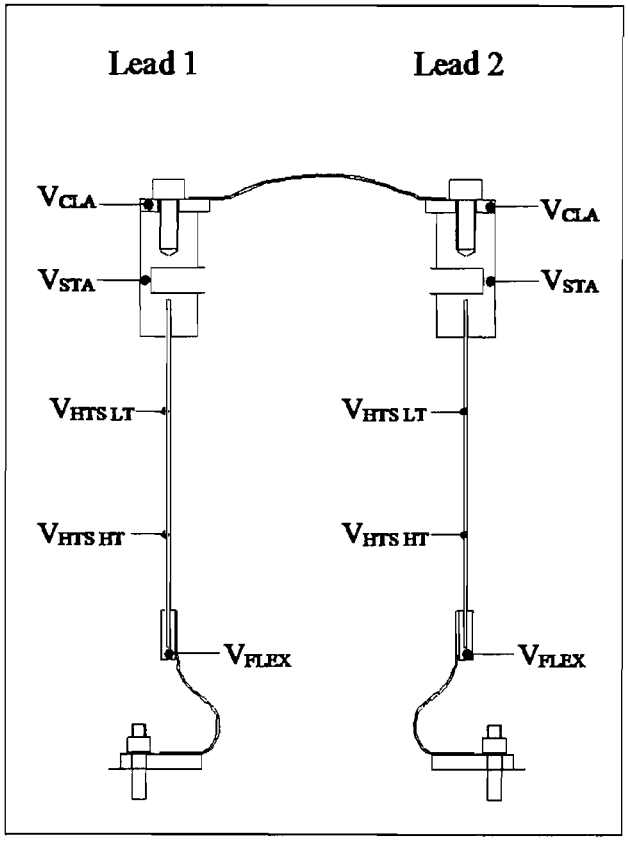

Figure 3.22: Voltage tap positions

It can be seen that all joints exhibit a linear current voltage characteristic. This is not at first obvious because a logarithmic scale is used to show the large differences between measured voltages. The resistance across each joint and the associated power dissipations calculated at an operating current of 300A are shown in Table 3.10. The resistances of the clamped joints ($V_{HTS\ LT}$ to V_{STA}) on lead 1 and lead 2 differ by an order of magnitude demonstrating the significant effect that the joint surface conditions have on the resistance of the clamped joint. The difference in joint resistances occurred even though every effort was made to prepare the joints in a similar manner. Soldered joints at the same position on both lead 1 and lead 2 exhibit approximately the same resistance. The resistance of the soldered joints at the 77K end of the HTS leads (V_{FLEX} to $V_{HTS\ HT}$) is 14 times higher than the resistance of the soldered joints at the end of the HTS leads in contact with the coldhead ($V_{HTS\ LT}$ to V_{STA}). It is thought this difference is due to the temperature dependent resistivity of the copper, silver and solder [7] that constitute the joint. No detectable voltage rise was measured across the HTS leads until an applied current of 200A. It was observed that even at 300A the HTS leads operate significantly below their critical current. Using the contact resistances of the joints from Table 3.7 it is estimated that the total heat dissipation from the joints of 164mW will further increase the temperature difference between the coldhead and the thermal station by a maximum of 0.27K.

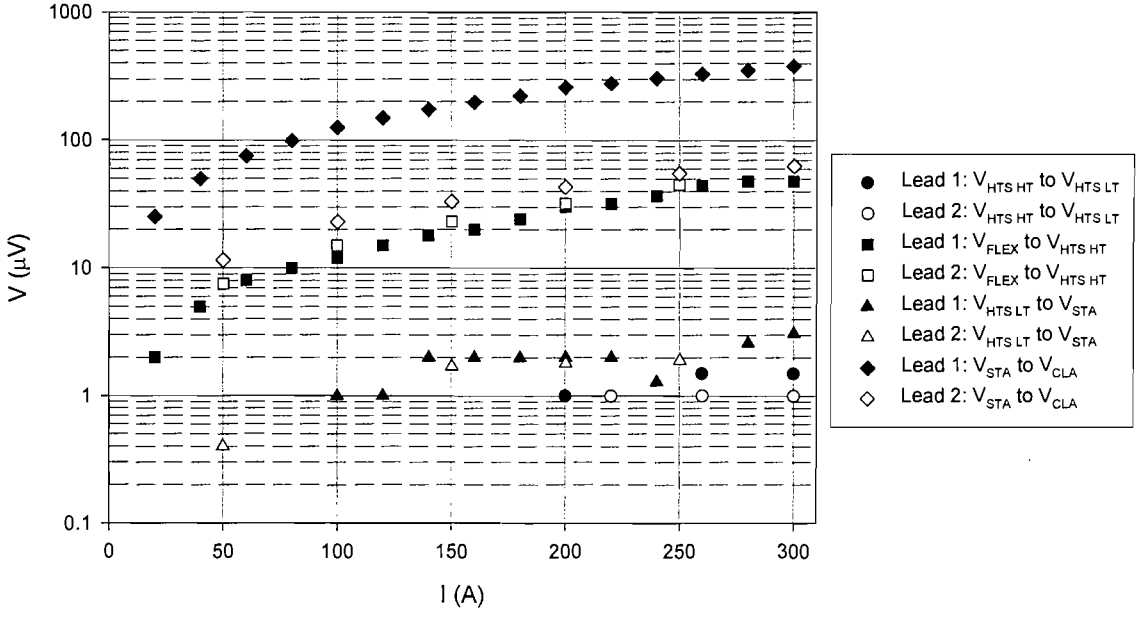

Figure 3.23: I-V characteristics of current lead joints

Joint	R_{joint} (μΩ)	Q @ 300A (mW)
Lead 1:V_{FLEX} to $V_{HTS\ HT}$	0.153	13.8
Lead 2:V_{FLEX} to $V_{HTS\ HT}$	0.167	15.0
Lead 1: $V_{HTS\ LT}$ to V_{STA}	9.30e-3	0.8
Lead 2: $V_{HTS\ LT}$ to V_{STA}	8.70e-3	0.8
Lead 1: V_{STA} to V_{CLA}	1.265	113.9
Lead 2: V_{STA} to V_{CLA}	0.216	19.4
		Total: 164mW

Table 3.10: Electrical contact resistances of current lead joints

3.9.3 Coldhead temperature dependence on current

The temperature of the coldhead was measured during the I-V characterisation of the current leads and is shown as a function of the operating current in Figure 3.24. It is expected that as the current is increased the heat load produced from dissipation at the joints and across the electrical links will cause the temperature of the coldhead to rise. This behaviour is observed in Figure 3.24; it can be seen that as the coldhead temperature

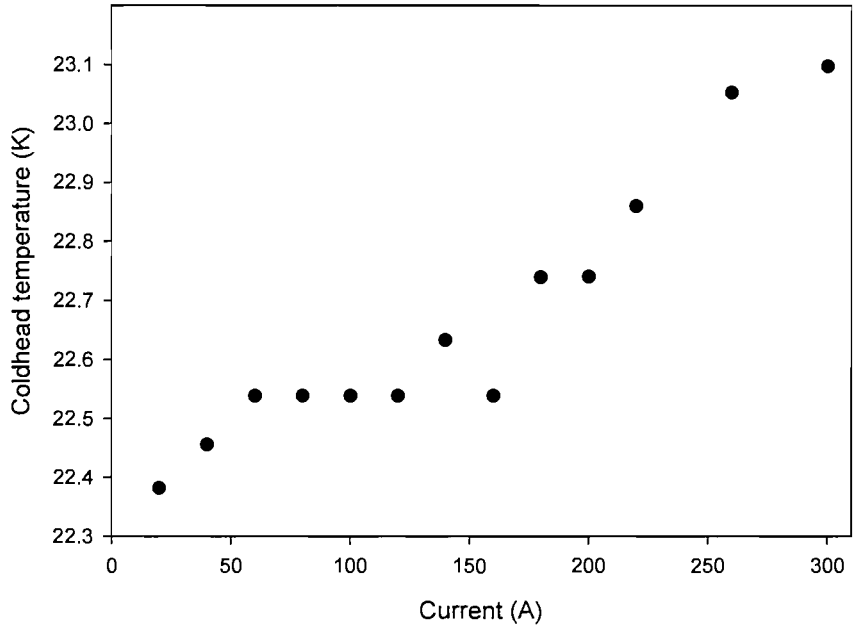

Figure 3.24: Coldhead temperature as a function of current

increases as the operating current is increased. The irregular shape of the graph is most probably due to the behaviour of the cryocooler. A maximum temperature rise of 0.7K is observed at the maximum current of 300A which shows that the current can be varied whilst keeping the coldhead temperature stable.

3.10 Conclusion

Apparatus has been designed and manufactured that can provide stable operating conditions for a HTS coil over a wide temperature range. The apparatus uses a cryocooler and conduction cooling system to provide cooling to the coil. A combination of gas cooled resistive current leads and HTS current leads supply current to the coil. HTS current leads were used to minimise the heat leak to the coldhead thereby limiting fluctuations of the coldhead temperature when the operational current is varied. The apparatus was tested up to a maximum operating current of 300A at which only a 0.7K drift in the coldhead temperature was observed. The electrical resistance of joints in the current lead assembly were measured up to 300A. It was found that the majority of heat dissipation from the joints was due to the bolted joints as expected. The temperature difference between the coldhead and coil was estimated by considering the temperature drop along thermal links and due to the thermal contact resistances across joints. The actual temperature difference was measured in section 4.8 when the coil was mounted into the apparatus. The commissioning of the apparatus provided invaluable experience in conduction cooling technology

3.11 References

[1]A. Korpela, Lehtonen, J., Mikkonen, R., Quench, ***Superconductor science and technology***, 2003, vol. 16, pp.355-360

[2] Al-Mosawi, M.K, Beduz, C., Goddard, K.F., Sykulski, J.K., Yang, Y., Xu, B., Ship, K.S., Stoll., R, Stephen, N.G, ***Physica C***, 2002, vol. 372-376, p.1539-1542

[3] Kalliohaka, T., Korpela, A., Lehtonen, J., Mikkonen, R., 2003, ***Superconductor Science and Technology*** vol. 16, pp.946-950

[4]Penny, M., Beduz, C., Yang, Y., Manton, S., Wroe, R., ***Applied-Superconductivity-1997-Proceedings-of-EUCAS-1997***, 1997, vol.2, pp.1551-1554

[5] Nordic Superconductor Technologies, ***Application note 0010v01***

[6] Dudley, R., ***Personal communication***

[7]Wilson, M.N., **Superconducting magnets**, Oxford University press, 1983

[8] Fujishiro, H., Ikebe, M., Noto, K., Sasaoka, T., Nomura, K., ***IEEE transactions on Magnetics***, 1994, vol. 30, no. 4, pp. 1086-1090

[9] Vase, P., Flukiger, R., Leghissa, M., Glowacki, B., ***Superconductor Science and Technology***, 2000, vol. 13, pp. 71-84

[10] Indium Corporation of America, ***www.indium.com***

[11] Radio Spares, ***www.rswww.com***

[12] Gmelin, E., Assen-Palmer, M., Reuther, M., Villar, R., ***Journal of Applied Physics D***, 1999, vol.32, pp.19–43

[13]Lake Shore Cryotronics Inc, ***www.lakeshore.com***

[14] Omega, ***www.omega.co.uk***

[15]National Instruments, 2000, Part Number 320515F-01

Chapter 4 : Fabrication and characterisation of a (BiPb)2223 conduction cooled pancake coil

4.1 Introduction

HTS tape conductors based on the (BiPb)2223 system and manufactured by the powder in tube method are currently being produced [1,2] in lengths of up to a kilometre with critical current densities above 20kAcm^{-2} at 77K [3]. The availability of long lengths of conductor with high critical current density allows the construction of HTS coils. Thin film 2nd generation conductors have not been considered because they have not reached the same state of commercial availability.

In order to investigate the thermal stability and quench propagation characteristics of HTS coils a 38 turn pancake coil wound with (BiPb)2223 tape has been manufactured. It has been designed to integrate with the conduction cooling system detailed in chapter 3 so that tests can be performed over a range of operating temperatures. The various stages of coil design, manufacture, and testing are examined along with the challenges relating to conduction cooling the coil. The coil was characterised by measuring the critical current and quench current as a function of operating temperature. A procedure is presented to predict the critical current of a HTS coil over a range of operating temperatures. The transient temperature and voltage distributions across the coil were also measured when a quench was initiated due to an overcurrent.

The work presented will be of use to the HTS magnet designer when developing cryocooled HTS magnets which is one of the main applications for HTS conductors. When generating concepts for HTS magnets the critical current and quench current can be predicted with relative ease before detailed design work commences. This work also provides a basis for investigations into transient stability as detailed in chapter 5.

4.2 Coil design

4.2.1 Coil dimensions

The maximum coil diameter is set by the spatial constraints of the test apparatus and is approximately 90mm. The number of turns must be chosen so that the quench propagation can be studied without the influence of coil boundaries in the radial direction or artificial boundaries created by quench annihilation in the longitudinal direction. As shown in Chapter 2 the ratio of the quench propagation velocity in the longitudinal direction to that in the radial direction is approximately 10:1. A coil thickness of 15mm, or approximately 38 turns, was chosen so that when the quench front has reached the coil boundary it is estimated to have progressed 115° around the coil from the quench initiation point.

4.2.2 Strain effects

During coil winding tension must be applied to the conductor to ensure the turns are closely packed. The conductor must be tolerant against axial strains produced by the winding tension and strains caused by bending of the conductor. The irreversible strain limit ε_{irr} [dimensionless] is defined as the strain beyond which the critical current decreases irreversibly [4]. (BiPb)2223 conductors are produced in tape form to obtain the best performance. A benefit of the tape geometry of the conductor is that it helps to reduce the tensile and compressive strains at the conductor surface during bending. One method of increasing the strain tolerance of HTS tapes is to use a sheath material that has sufficient strength so that during cooldown the sheath will induce a pre-compression in the tape caused by differential thermal contraction. When a tensile strain is applied the critical current will be almost constant until the thermally induced pre-compression is cancelled, therefore increasing the irreversible strain limit of the conductor. The irreversible strain limit of Ag alloy sheathed conductors subjected to bending strains is approximately 0.2%. This is increased to approximately 0.4% if stainless steel clad tapes are used.

Due to the sufficiently high strain tolerance of HTS conductors that can now be produced conductors can be transported in their final form by the supplier and wound into coils by

the customer, this is known as the react and wind process. In contrast the Nb_3Sn superconductors are extremely strain sensitive and the multifilamentary conductor must be wound and then heat treated in-situ, this is known as the wind and react process. The wind and react process has several disadvantages compared to the react and wind process including the need for high temperature inter-turn insulations and large furnaces for heat treating the coils.

The bending strain to which a conductor is subjected when wound onto a former is given by Equation 4.1 [4]; where t [m] is the conductor thickness and R [m] the bending radius. Equation 4.1 assumes the change in thickness due to bending is negligible. Considering a minimum bend radius of 30mm and maximum bend radius of 45mm as dictated by the spatial constraints the calculated strain is 0.41% at the inner radius and 0.28% at the outer radius. For the conductor of interest, the critical current in self field as a function of bending strain and operating temperature was measured by a colleague, the results are presented in Figure 4.1 [5]. It can be seen that the effect of the bending strain on the critical current is independent of temperature between 4.2K and 77K. The measurement does not

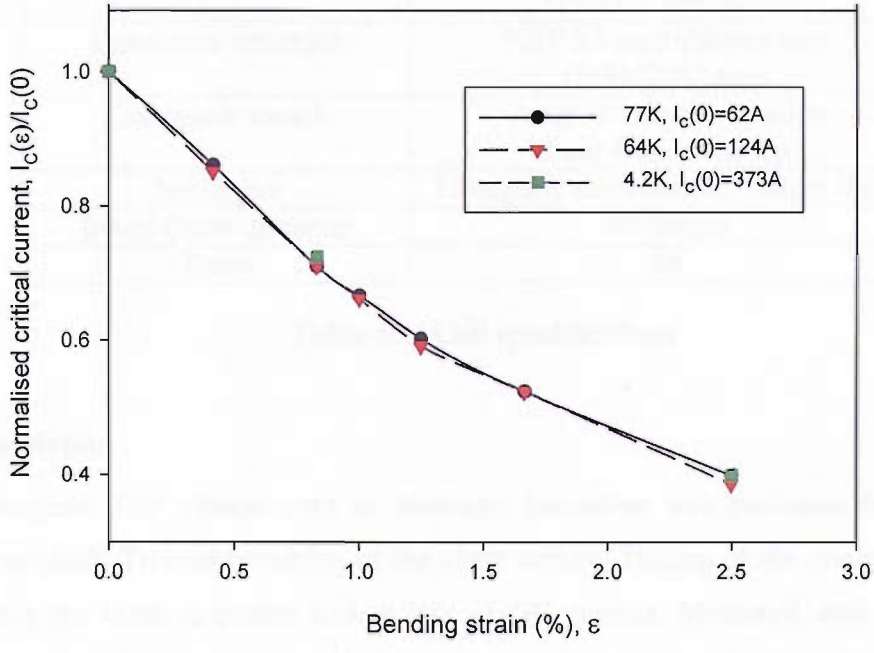

Figure 4.1: Bending strain dependence of the critical current for a NST 'Zerome Hercules' tape

have sufficient resolution to show evidence of thermally induced pre-compression. However, it can be seen that a reduction in the critical current to 85% and 91% of its unstrained value was expected at the inner coil radius and outer coil radius respectively.

$$\varepsilon = \frac{t}{2R + t} \quad \text{[dimensionless]} \qquad \textbf{Equation 4.1}$$

A winding tension of 3N was applied to the conductor during winding. It was observed [6] that this tension did not cause degradation in pure Ag sheath tapes whilst still ensuring a sufficient packing density.

4.3 Coil winding

An overview of the coil components and coil geometry are summarised in Table 4.1. The preparation of each component in the coil and the winding process are described below.

Item	Specification
Former	Phenolic cotton Tufnol 'Carp' brand
Conductor structure	NST 37-multifilamentary (BiPb)2223 tape
Conductor sheath	Outer: 0.1MgNi-Ag alloy Inter-filaments: Ag
Insulation	Fibreglass cloth ribbon, 100μm thick
Inner/ Outer diameter	60/ 90mm
Turns	38

Table 4.1: Coil specifications

4.3.1 Insulation

The fibreglass cloth ribbon used as inter-turn insulation was produced from a sheet of fibreglass cloth. To enable cutting of the cloth without flaking of the fibres or warping of the weave the cloth is coated with a mix of GE varnish, Methanol, and Toluene. High concentrations of GE varnish make the cloth easier to cut and eliminate flaking of the individual fibres but make the cloth brittle and seal the weave of the cloth. This prevents the penetration of epoxy resin into the weave consequently adversely affecting the coil

strength. The optimum ratio of the coating mix was determined by varying the GE varnish concentration and examining the wetting properties of epoxy, brittleness of the cloth, and both the warping and flaking of the weave. The optimum GE varnish: Methanol: Toluene ratio was found to be 7.5:1:1. The fibreglass cloth was drawn through parallel razor blades as shown in Figure 4.2 to produce lengths of cut fibreglass ribbon of the same width as the superconducting tape. Guides were needed after the cutting blades to ensure the weight of the cut tape did not distort the uncut cloth.

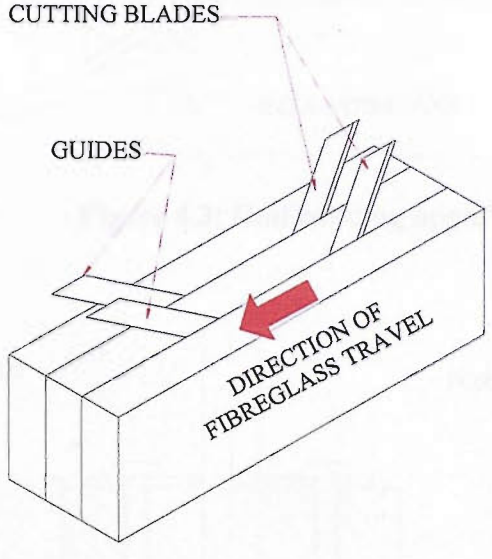

Figure 4.2: Fibreglass cutting apparatus

4.3.2 Coil Winding apparatus

The machine used for coil winding consists of a conductor spool, insulation spool, brake to add tension to the conductor and a rotating guide plate made of PTFE as shown in Figure 4.3. 5 copper sheets (grade C101) were screwed to the periphery of the former to create a thermal and electrical boundary. The former was attached to the guide plate which provides a flat surface to wind the coil against as shown in Figure 4.4. PTFE is used because of its low surface energy and hence non-stick properties, consequently after impregnation with epoxy resin the coil could be removed from the guide plate.

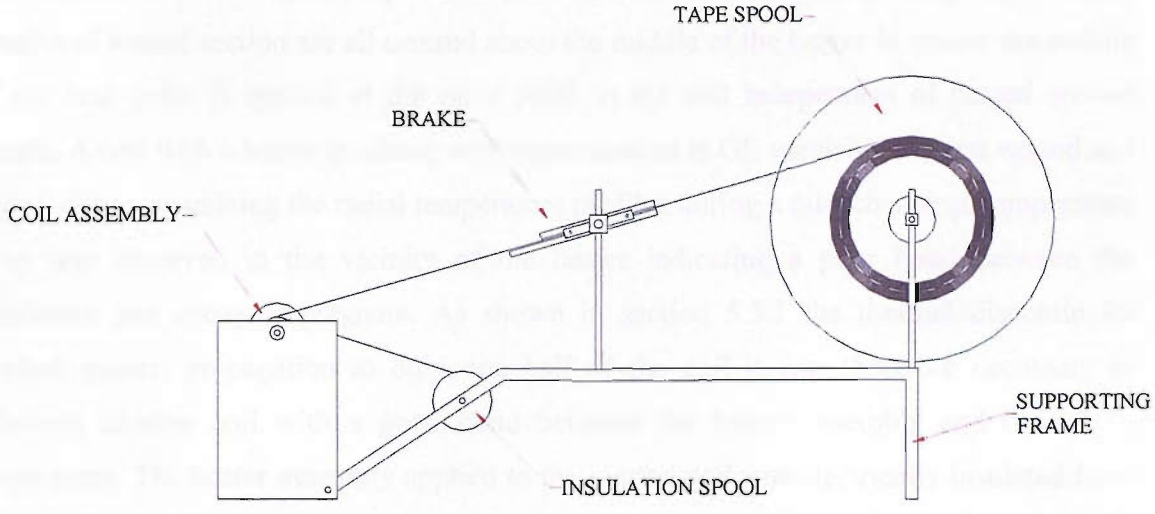

Figure 4.3: Coil winding apparatus

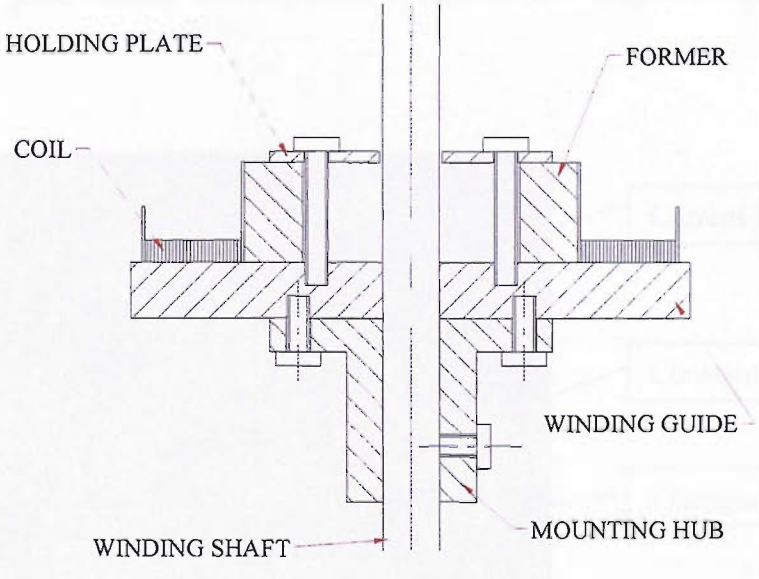

Figure 4.4: Coil winding assembly

4.3.3 Quench heater

A constantan ribbon heater (200mm x 2mm x 0.15mm) was co-wound with the coil. It was placed adjacent to the middle turn and the purpose of the heater is to initiate a quench in the

winding. Current leads are positioned to allow heated sections of 25mm, 60mm, 125mm, and 200mm to be energised representing distributed and localised heating. The various lengths of heated section are all centred about the middle of the heater to ensure the middle of the heat pulse is applied at the same point in the coil independent of heated section length. A coil with a heater insulated with paper soaked in GE varnish, was first wound and tested. When examining the radial temperature profiles during a quench a large temperature drop was observed in the vicinity of the heater indicating a poor bond between the insulation and epoxy impregnate. As shown in section 5.5.1 the thermal discontinuity limited quench propagation to only one half of the coil it was therefore necessary to fabricate another coil with a good bond between the heater assembly and the epoxy impregnate. The heater assembly applied to the second coil was electrically insulated from the conductor by a layer of 40μm fibreglass cloth impregnated with epoxy resin. The thickness of the entire heater assembly was kept below 340μm by flattening the current lead joints with a rolling machine as shown in Figure 4.5. This method of applying the heater produced a good thermal contact as observed from the temperature profiles measured in Chapter 5.

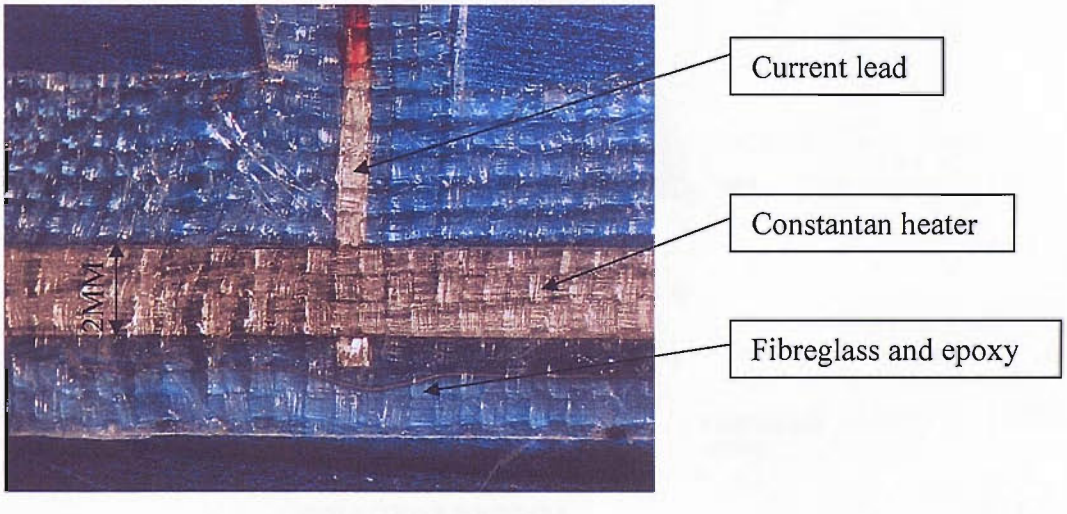

Figure 4.5: Disturbance heater, detail of current lead junction

4.3.4 Coil winding process

Electrical and thermal links were applied to the inner boundary of the coil by soldering the conductor to the entire periphery of the copper boundary of the former. The conductor was then co-wound with fibreglass insulation to form a 38 turn single layer pancake coil. A heater as described in section 4.3.3 was placed with its mid-plane at 180°. All current leads to the heater are symmetric about this mid-plane. Miniature copper cold fingers (90mg, length=20mm) were soldered to the conductor during coil winding. Thermocouples could be soldered to the cold fingers after epoxy impregnation therefore simplifying coil fabrication and installation. The cold fingers were placed in such a way that the temperature profiles in the coil during a quench could be measured. The outer thermal and electrical links consisting of 10 copper links (50mm x 7mm x 0.5mm) were soldered equidistant around the periphery of the final turn to form the outer boundary. Insulation was wound around the finished coil to hold the turns in place and produce a 2mm thick durable surface when vacuum impregnated. The coil design including the placement of the cold fingers is shown in Figure 4.6 and the cold finger positions listed in Table 4.2. Quench propagation

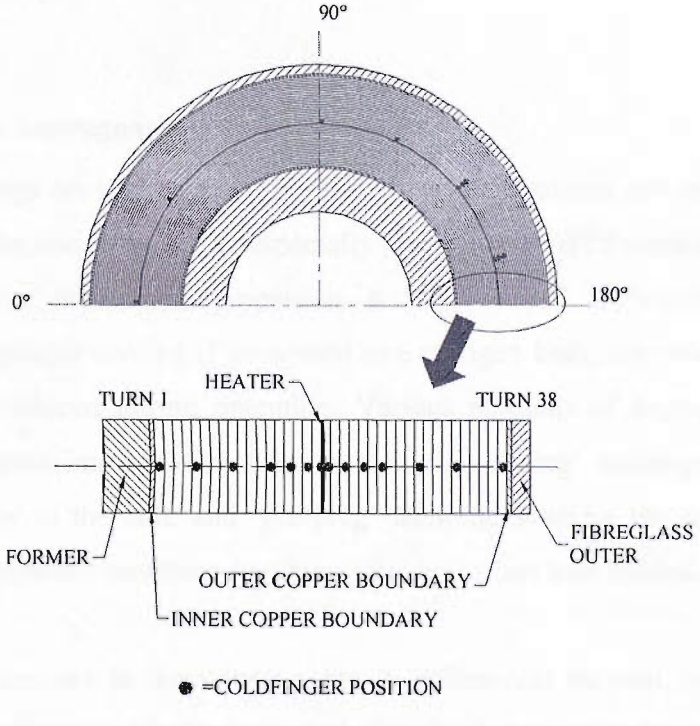

Figure 4.6: Coil construction and cold finger positioning

symmetry was assumed meaning that instrumentation cold fingers were placed on only one half of the coil.

Cold finger #	Turn #	Angle (°)	Cold finger #	Turn #	Angle (°)
1	38	180	13	5	180
2	33	180	14	1	180
3	29	180	15	19	165
4	25	180	16	21	165
5	23	180	17	23	165
6	21	180	18	19	140
7	19	180	19	21	140
8	Heater (19)	180	20	23	140
9	17	180	21	19	90
10	15	180	22	19	115
11	13	180	23	19	35
12	9	180	24	19	0

Table 4.2: Cold finger positions

4.4 Impregnation

4.4.1 Why use impregnation?

Magnet windings are impregnated to eliminate turn movement and increase the mechanical properties of the winding. This is especially important for HTS windings in which the silver sheath has poor mechanical properties. A 'dry' wound HTS coil, though having the advantage of greater cooling if immersed in a cryogen bath, may not be able to withstand the stresses produced during operation. Various methods of impregnation are available including vacuum impregnation techniques, 'wet winding' techniques where the resin is applied directly to the coil, and 'pre-preg' techniques where the conductor is co-wound with pre-impregnated insulation that bonds the coil when heat treated.

To minimise stresses in the winding due to differential thermal contraction the thermal expansion coefficients of the resin and the conductor must be matched. This can be accomplished by adding filler to the resin. A coil construction and vacuum impregnation technique has been developed at Southampton University that involves using fibreglass

tape as both electrical insulation between conductor windings and as a filler to match the thermal contraction of the resin to that of the conductor. Measurements from previous work [6] have indicated no degradation of the critical current due to the impregnation process or after 5 cooling cycles between room temperature and 100K.

4.4.2 The vacuum impregnation process

The apparatus to perform the vacuum impregnation process is detailed in Figure 4.7. The epoxy resin used is Stycast 1266, a 2 part resin system from 'Emmerson and Cumming' that cures due to an exothermic reaction. The coil winding assembly was placed in a chamber that was evacuated and epoxy resin introduced into the winding. Vacuum conditions were maintained until all air pockets in the epoxy had collapsed and the chamber then brought to atmospheric pressure thus forcing the epoxy resin into all gaps in the winding.

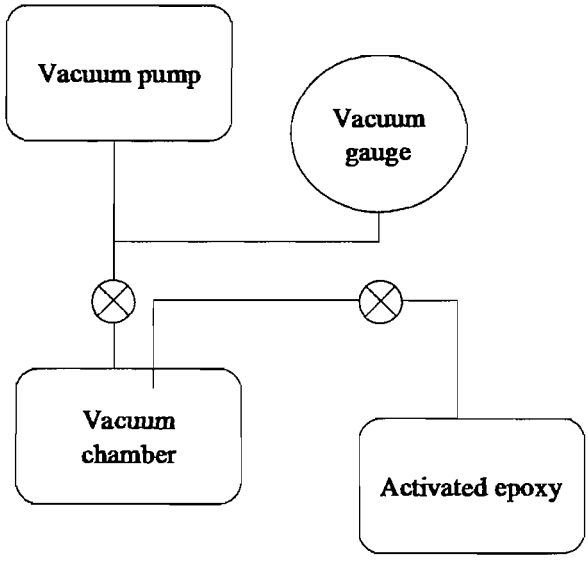

Figure 4.7: Vacuum impregnation apparatus

The vacuum impregnation process is used to minimise voids and cracks in the coil structure that can reduce the mechanical properties of the coil winding and also degrade thermal conductivity leading to localised heating during a quench. Figure 4.8 shows a radial cross-

section of a coil fabricated using the same method as described above. No voids, bubbles or cracks are observed indicating a successful impregnation technique.

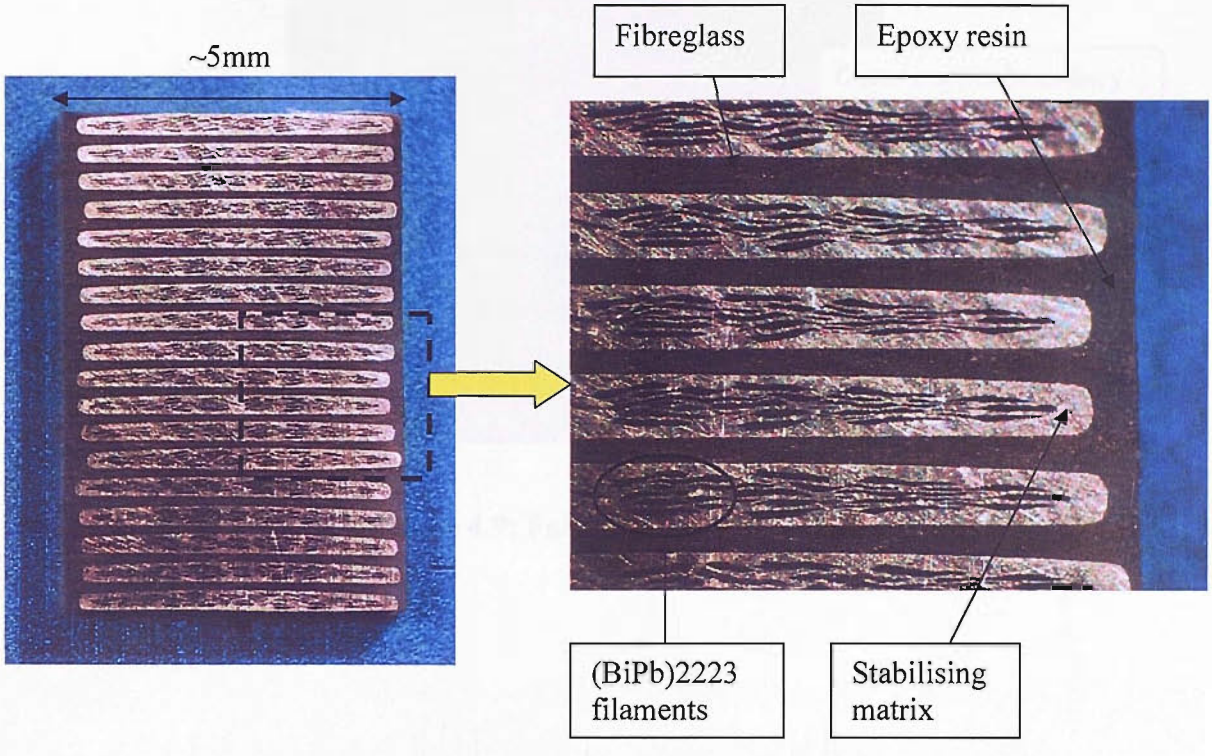

Figure 4.8: Impregnated coil cross section

4.5 Mounting the coil into the conduction cooling apparatus

The pancake coil to be tested, Figure 4.9, was mounted onto locating studs in the conduction cooling apparatus, as shown in Figure 4.10. Thermal and electrical connections were made to the coil by soldering connecting braids to the inner and outer coil boundaries with a low temperature Indium alloy solder [7]. Thermocouples were soldered to the copper cold fingers and connections made to the quench heater.

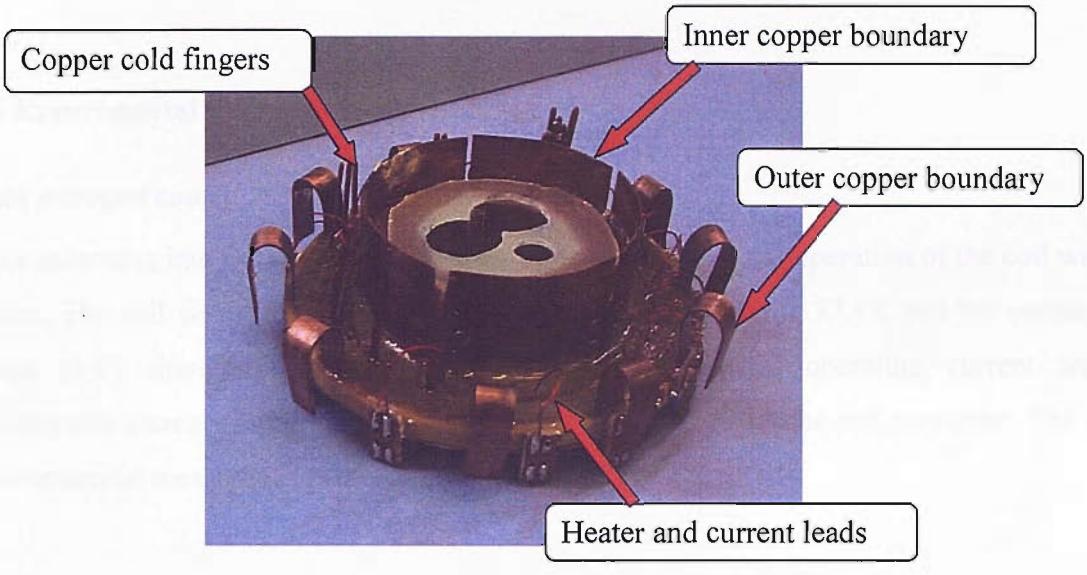

Figure 4.9: Fabricated pancake coil

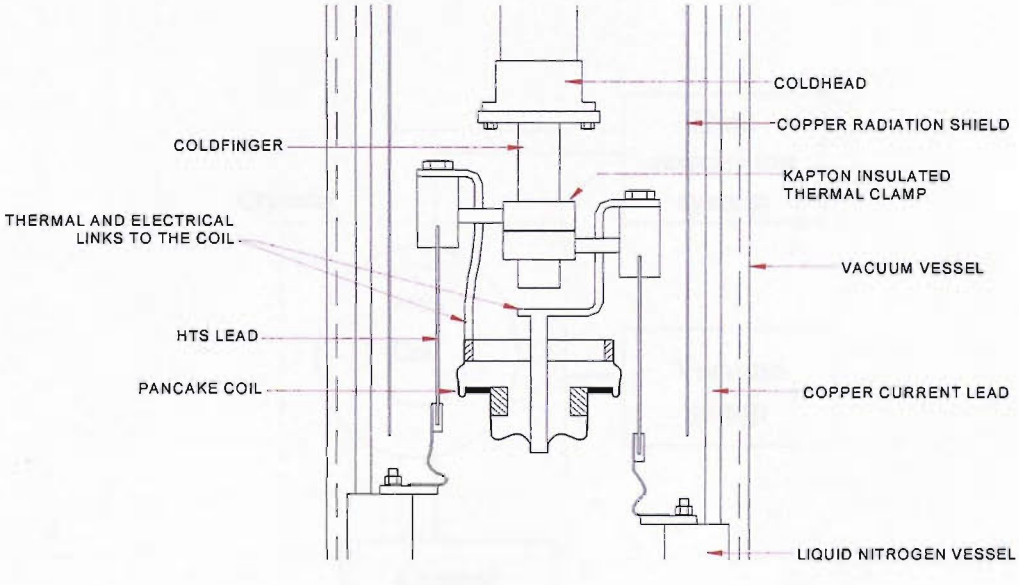

Figure 4.10: Mounting of the HTS coil into the conduction cooling apparatus

4.6 Measurement of the coil I-V characteristics

4.6.1 Experimental

Liquid nitrogen cooled

Before mounting into the conduction cooling apparatus the normal operation of the coil was ensured. The coil was fully submerged in a liquid nitrogen bath at 77.4K and the current-voltage (I-V) characteristic of the coil was measured. The operating current was incrementally increased and the voltage across the entire length of the coil measured. The I-V characteristic measured is presented in Figure 4.12.

Conduction cooled

Connections were made to the test apparatus as per the experimental set-up, Figure 4.11. For each I-V measurement the coil boundaries were set at a given temperature between 35K and 74K. The operating current was successively increased to produce an electric field

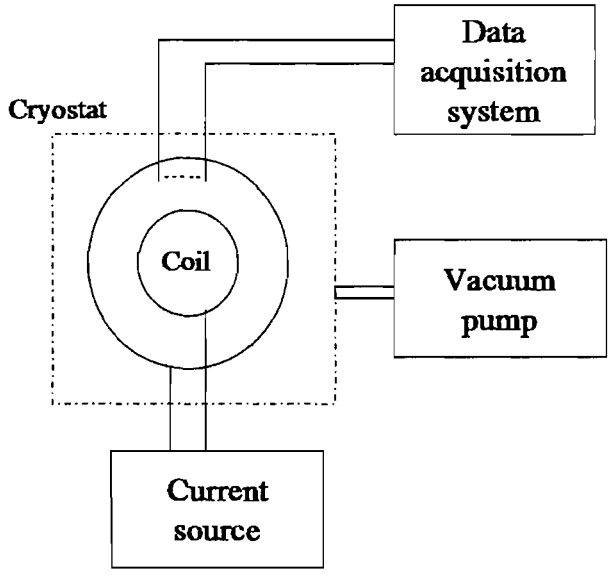

Figure 4.11: I-V measurement experimental set-up

increase across the entire length of the coil of approximately 0.2μV/cm at each increment. Temperature and voltage measurements were taken once the coil had reached a thermally steady state at each increment of current.

4.6.2 Results

The measured I-V characteristics across the entire length of the coil as a function of operating temperature are shown in Figure 4.12. The voltage has been converted to electric field, E [V.m^{-1}], to enable the identification of the coil critical current, I_C [A], using a 1μV/cm criterion. At the quench current, I_Q [A], the coil becomes unstable and the temperatures and voltages start to increase without bound. The quench current is the maximum current shown on the I-V characteristics and is discussed in more depth below in section 4.9. The entire I-V characteristic of the coil in liquid nitrogen is not shown because a quench is not observed until 42A when an average electric field of 47μV/cm is produced.

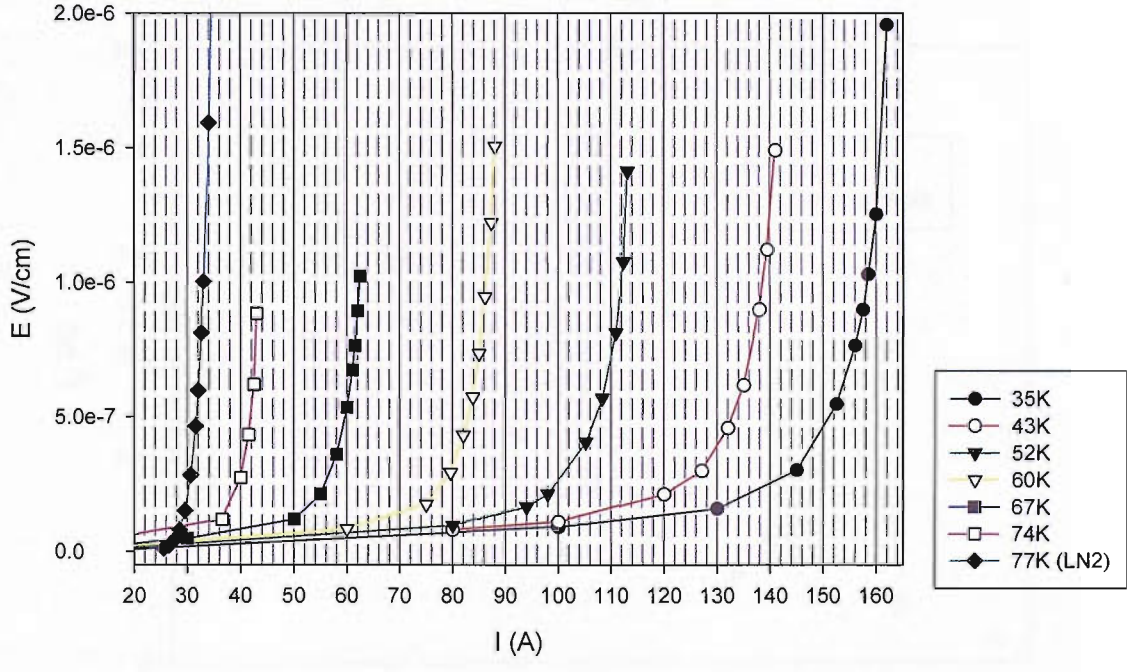

Figure 4.12: Coil I-V characteristic

The I-V characteristics shown in Figure 4.12 exhibit a small baseline voltage that appears to increase linearly as the operating current is increased. It is thought this is because one of the voltage taps used in the measurement was soldered to a copper current lead

approximately 5mm from the end of the HTS tape. The voltage drop across a portion of the copper current lead can therefore be seen in the I-V characteristics.

The determination of the coil critical current is an essential tool when examining the stability of HTS coils because many stability analyses represent the quench current of a coil as a ratio of the critical current. The average critical current measured over the entire coil length as a function of operating temperature, T_{OP} [K], is shown in Figure 4.13. Also shown is the critical current as a function of operating temperature for a short tape sample [8]. The coil critical current is considerably lower than that of the short tape sample. The degradation may be due to strain effects, the effect of the generated magnetic field or a combination of the two. Section 4.7 below attempts to confirm that the critical current degradation observed is mainly due to the field generated by the coil.

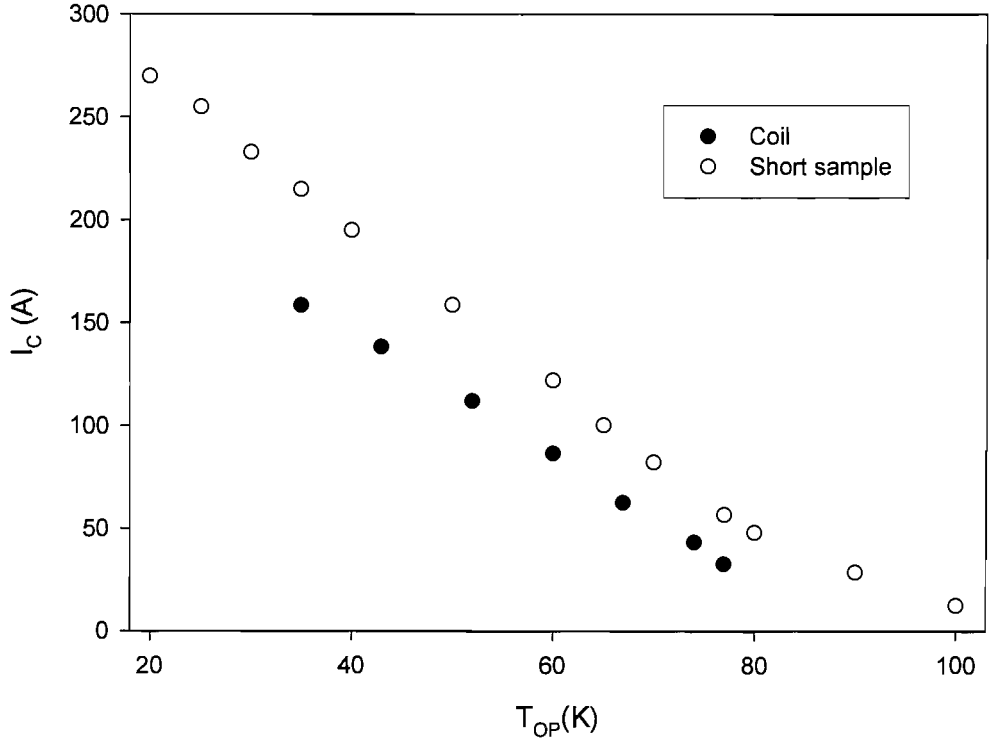

Figure 4.13: Temperature dependence of the coil critical current

4.7 Prediction of the coil critical current

The analysis is conducted to confirm that the critical current degradation observed is due to the field generated by the coil. The field produced by the coil at each operating temperature when operating at the measured critical current was simulated using finite element analysis (FEA) software. The effect of the simulated field on the critical current of a short sample was calculated using a scaling function and the predicted critical current compared to the measured critical current. The steps of the analysis are presented in the following sections.

4.7.1 Magnetic field calculation

The ANSYS finite element analysis program was used to calculate the distribution and magnitude of the magnetic flux density generated by the coil at different operating currents. An axisymmetric 2-dimensional representation of the coil and surrounding vacuum space was constructed and the entire model was meshed with 4 node magnetic elements (PLANE 13). At each operating temperature a current equal to the measured critical current of the coil was applied to the coil section and the steady state solution simulated. To account for the anisotropy of the (BiPb)2223 conductor the simulated field is shown as separate components. The field in the radial direction denoted as B_r [T] is perpendicular to the surface of the tape and the field in the axial direction denoted as B_z [T] is parallel to surface of the tape. Figure 4.14 and Figure 4.16 show contour plots of the simulated B_r and B_z distributions over the coil and surrounding vacuum space for an operating current of 158.5A. It can be seen that both B_r and B_z vary as a function of coil radius and axial distance along the coil. To further investigate the calculated field distribution B_r and B_z were calculated at different axial distances through the coil as shown in Figure 4.15 and Figure 4.17 respectively. The axial distances shown are; on the top surface of the coil, 1mm below the top surface and on the coil mid-plane. The field component perpendicular to the surface of the tape conductor causes the majority of critical current degradation. Therefore the point in the coil that will be subjected to the highest critical current degradation is generally the point that sees the maximum value of B_r. In this coil that is the top and bottom surfaces, on approximately the middle turn.

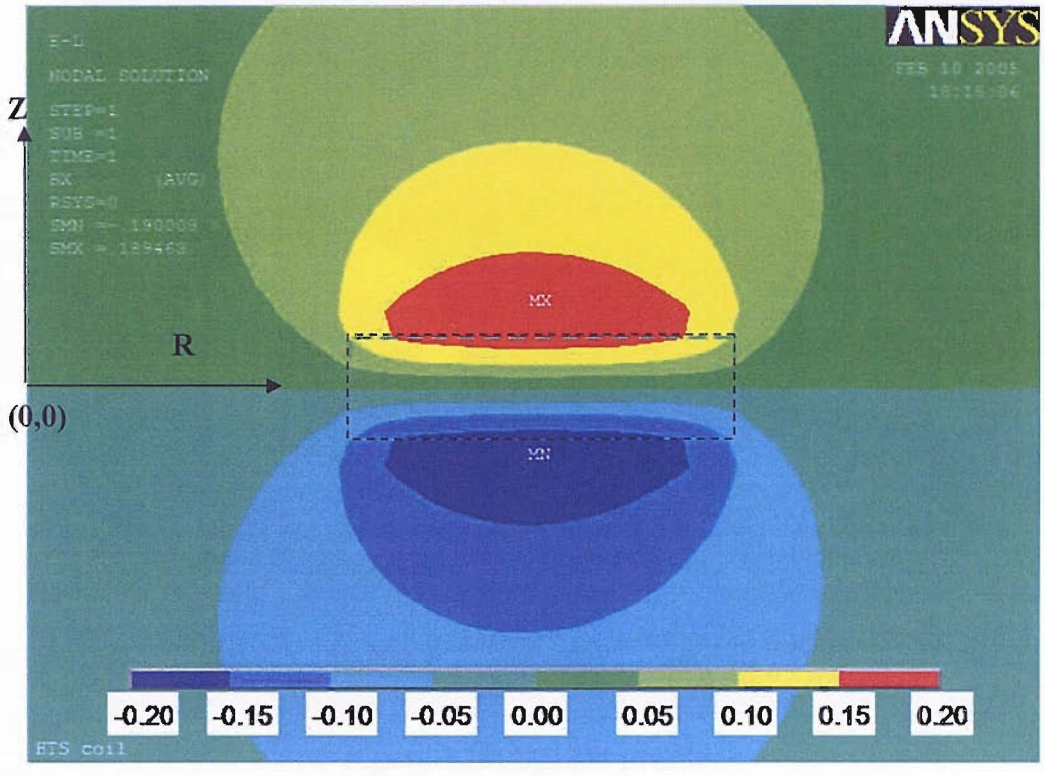

Figure 4.14: B_r field plot 158.5A

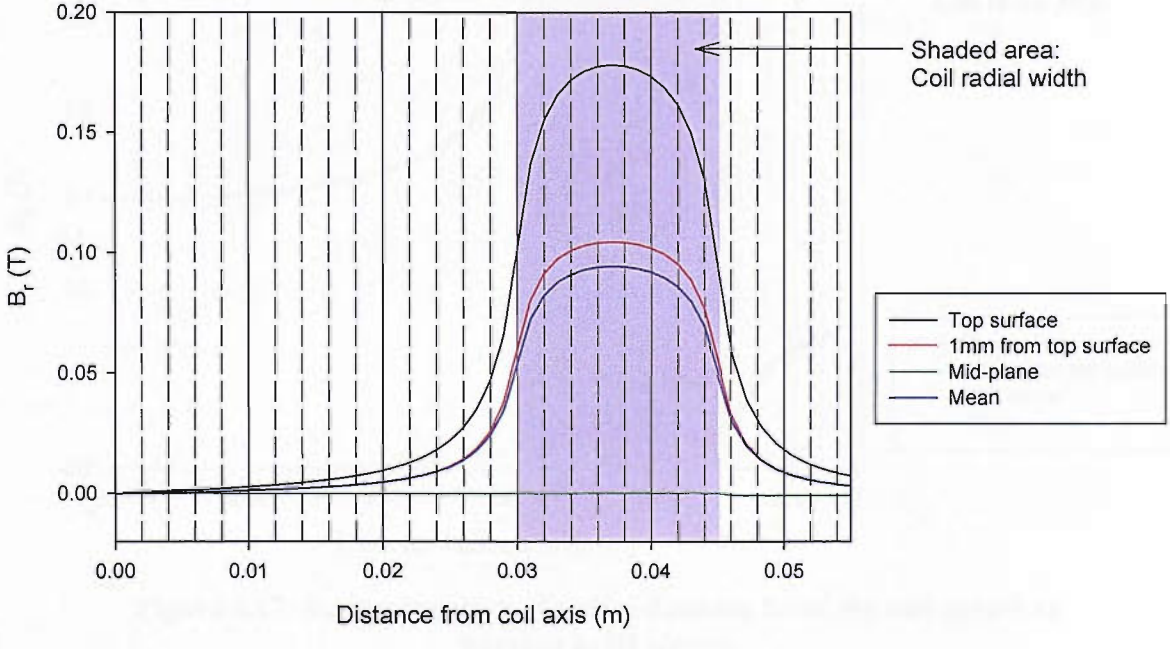

Figure 4.15: B_r as a function of radial distance from coil centre at varying axial planes

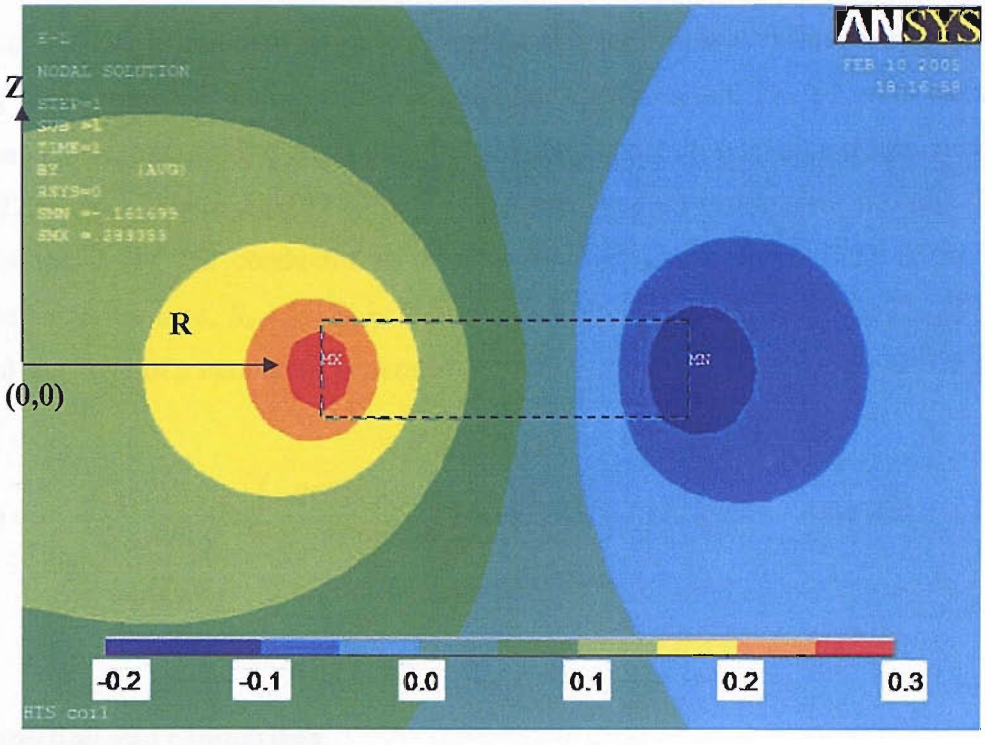

Figure 4.16: B_z field profile

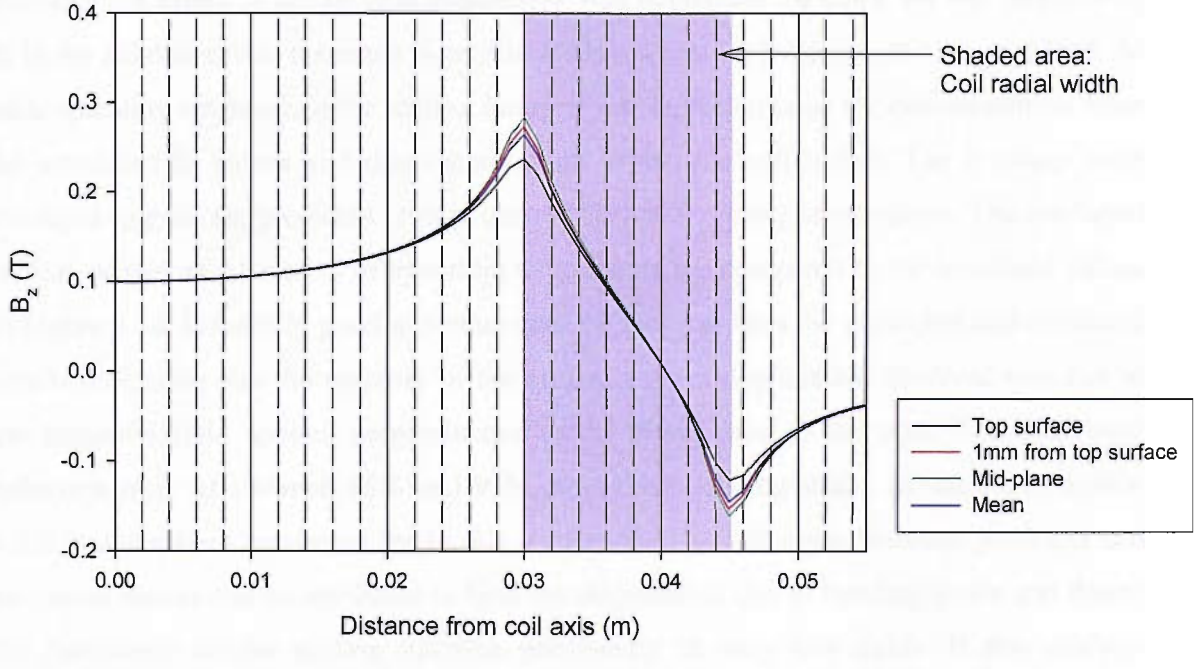

Figure 4.17: B_z as a function of radial distance from the coil centre at varying axial planes

4.7.2 Scaling function

The critical current degradation due to the applied magnetic field is influenced by the coil operating temperature. A scaling function proposed by Kobayashi [9], given in Equation 4.2 was used to account for the effect of both field and temperature on the critical current of a (BiPb)2223 tape. Where $J_C(B,T)$ [A.m^{-2}] is the predicted critical current density, $J_{C0}(T)$ [A.m^{-2}] is the J_C of the conductor in zero external magnetic field, $B(T)$ is the field perpendicular to the tape, $B_{irr}(T)$ [T] is the irreversibility field [10], and $B_{self}(T)$ [T] is the calculated self field of a conductor generated by transport current in zero external field [11].

$$J_C(B,T) = \frac{J_{C0}(T)}{\log\left(\frac{B_{self}(T)}{B_{irr}(T)}\right)} \log\left(\frac{B(T)}{B_{irr}(T)}\right) \qquad [\text{A.m}^{-2}] \qquad \textbf{Equation 4.2}$$

4.7.3 Prediction and comparison

The B_r component of the field causes the majority of the critical current degradation and therefore the effect of the B_z field component was neglected. To allow for the variation of B_r in the axial direction the mean B_r profile at each operating temperature was examined. At each operating temperature the scaling function was used to predict the critical current from the simulated B_r values at 6 equidistant points across the coil radius. The 6 values were averaged to give the predicted critical current at that operating temperature. The predicted critical current as a function of operating temperature are compared to the measured values in Figure 4.18. Relatively good agreement can be seen between the predicted and measured results indicating that the majority of the critical current degradation observed was due to the magnetic field applied perpendicular to the broad face of the tape. The calculated reduction in I_C of between 85% and 91% due to the bending strain, as shown in section 4.2.2, has not been accounted for in this prediction. The difference between predicted and measured results can be attributed to both the degradation due to bending strain and due to the inaccuracy of the scaling function particularly at very low fields. If this analysis procedure were used as a design tool an iterative process could be used that started from a 'guess' value for the critical current and converged upon the final predicted value.

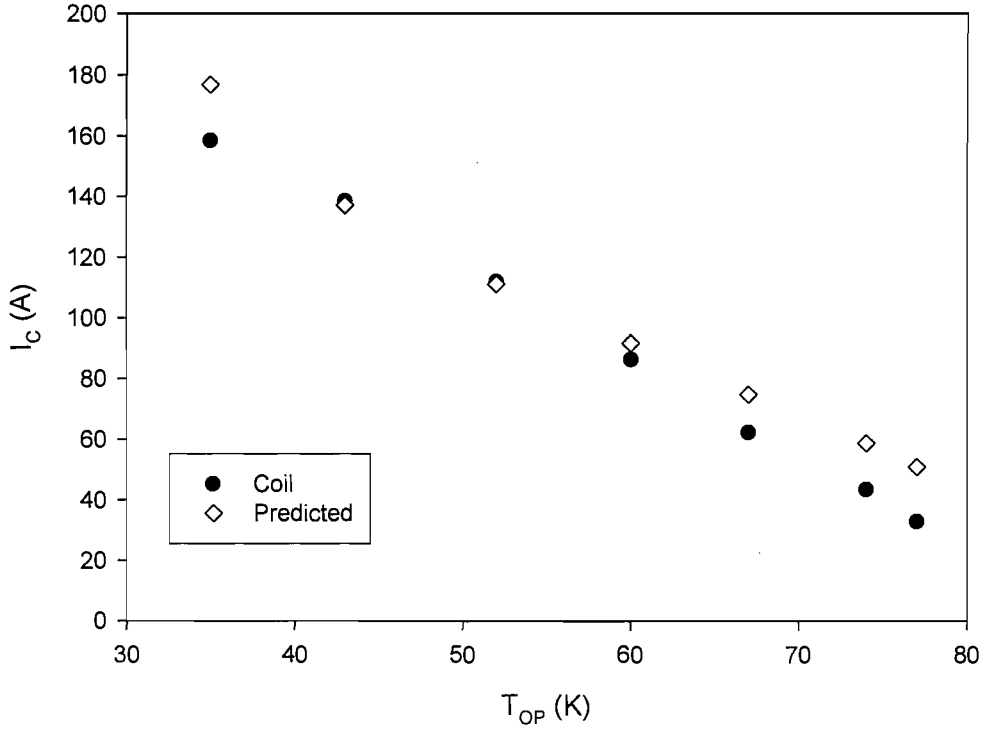

Figure 4.18: Comparison of the measured and predicted $I_c(T)$

4.8 Temperature differences across the conduction cooling system

At varying coldhead operating temperatures the temperature difference between the coil boundaries and coldhead was measured, as shown in Figure 4.19. No current was applied to the coil during the measurement. The temperature difference between the coldhead and coil boundaries of between 9K and 18K was observed. This is higher than the temperature drop of between 4.6K and 12.2K predicted in section 3.6. However, as previously stated a high uncertainty exists in the prediction due to the large variation in thermal contact resistance values used. It can be seen that a temperature difference between the inner and outer coil boundaries of approximately 2K is exhibited that is constant over the operating temperature range. This is thought to be due to the differing thermal resistance across the electrically isolated thermal clamps. The temperature difference between the coldhead and coil increases as operating temperature increases, despite it having been reported that the

thermal contact resistance should decrease as temperature is increased [12]. It is therefore assumed that the increasing temperature difference is caused by the decrease in thermal conductivity of the copper thermal links as the operating temperature increases above 20K. One major component of the temperature drop could be the thermal links consisting of copper sheet attached to the coil boundaries that were not accounted for in previous estimations.

With the coldhead at 23K the temperature difference across the electrically isolated clamps was measured and found to be 8K. The estimated temperature drop across the clamps was only 1K, indicating that the clamped surfaces only contact at a fraction of the available area. The temperature difference between the coldhead and coil, though larger than estimated, still allows the coil boundaries to reach a minimum temperature of 35K. At this temperature considerably different quench behaviour is expected than at the higher operating temperatures of over 70K.

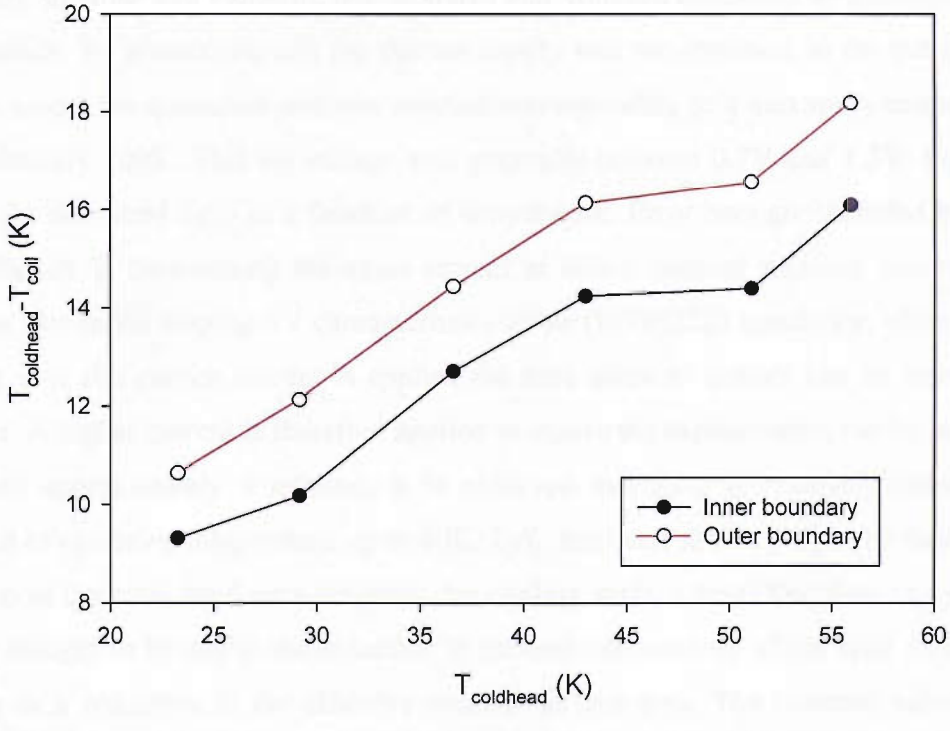

Figure 4.19: Temperature difference between the coldhead and coil boundaries as a function of operating temperature

4.9 Overcurrent tests

Due to the broad sloping current-voltage (I-V) characteristics of HTS conductors it is possible to balance the joule heat generation produced by an HTS tape in the current sharing regime with the cooling provided. Above the quench current joule heat generation exceeds the heat removed by cooling and the temperature of the coil will rise in an unbounded fashion resulting in a quench. The stability of a coil to a constant overcurrent, I_Q [A], is often expressed as the ratio of the quench current to the critical current (I_Q/I_C), mainly because the critical current is a commonly defined parameter for all conductors.

4.9.1 Quench current of the conduction cooled coil

The quench current of the conduction cooled coil was measured at each operating temperature by incrementally increasing the operating current and allowing the coil to thermally stabilise at each current increment. At the quench current the coil did not thermally stabilise and therefore temperatures and voltages continued to increase resulting in a quench. To protect the coil the current supply was programmed to cut out once a set voltage across the quenched coil was reached corresponding to a maximum temperature of approximately 100K. This set voltage was generally between 0.7V and 1.3V. Figure 4.20 shows the measured I_Q/I_C as a function of temperature. Error bars are included because of the difficulty in determining the exact current at which thermal runaway occurs. This is because, due to the sloping I-V characteristics of the (BiPb)2223 conductor, when a current slightly over the quench current is applied the time taken to quench can be many tens of minutes. A higher current is therefore applied to ensure the measurement can be acquired in less than approximately 5 minutes. It is observed that I_Q/I_C is relatively constant as a function of operating temperature up to 60K. I_Q/I_C has been shown [13] to be dependent on the ratio of the total conductor length to the cooling surface area. The drop in I_Q/I_C above 60K is thought to be due to the reduction in thermal conductivity of the solid thermal links leading to a reduction in the effective cooling surface area. The constant value of I_Q/I_C below 60K is thought to be due to a combination of the increased thermal conductivity of the solid thermal links balancing an increase in the volumetric heat generation of the coil.

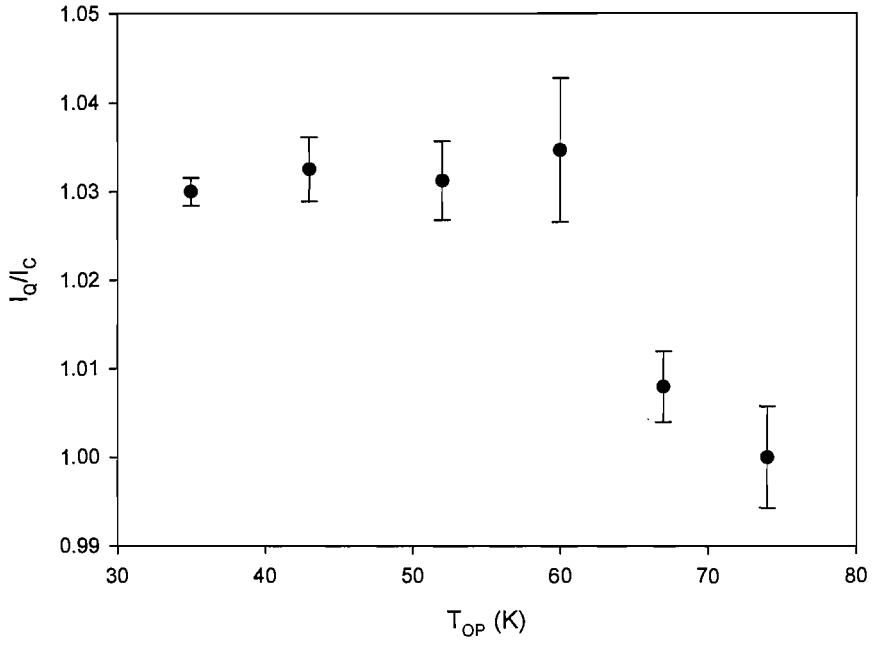

Figure 4.20: I_Q/I_C as a function of operating temperature

4.9.2 Quench current in liquid nitrogen

As shown in section 4.6 the critical current and quench current of the coil were determined when operated in a liquid nitrogen bath at 77.4K. The critical current and quench current were 33A and 42A respectively hence the observed I_Q/I_C was 1.27. The higher tolerance to overcurrents exhibited by the bath cooled coil compared to the conduction cooled coil is due to the increased surface area available for cooling. The coil submerged in liquid nitrogen is cooled at all external surfaces where as the conduction cooled coil has adiabatic boundaries imposed on the top and bottom surfaces and cooling is only provided at the inner and outer boundaries. The tolerance of the bath cooled coil to overcurrents is lower than a short tape sample which can be operated at $I_Q/I_C>2$. Heat generated in the short tape sample is removed from all external surfaces ensuring a large cooling surface area compared to the conductor length. The bath cooled coil is impregnated and therefore only the edges of the tape are exposed to liquid nitrogen and hence the ratio of the cooling surface area to the conductor length is lower than a tape sample.

4.9.3 Evolution of a quench due to an overcurrent

With the coil boundaries operating at 58K an overcurrent quench was initiated by increasing the current from a stable operating current of 91A to 95A. The transient thermal and electrical responses of the coil were measured using thermocouples and voltage taps positioned as described in Table 4.2. Figure 4.21 shows the evolution of the temperature distribution in the radial direction at a constant angle of 180°, and Figure 4.22 demonstrates the evolution of the temperature profiles in the longitudinal direction along the middle turn. For both figures, plot (a) shows temperature profiles across the winding at selected times after the current is increased and plot (b) shows the complete evolution of the temperature distribution in the winding. Up to a time of 410s after the current is increased temperatures rise uniformly along the circumferential length of the middle turn and smooth temperature profiles are observed indicating heat distribution across the width of the coil. After a time of 410s a sharp temperature peak develops around the middle turn of the coil indicating heat localisation due to insufficient time for diffusion of heat away from this area. From the radial temperature profiles it can be seen that the maximum temperature point evolves from the middle turn of the coil towards the outer boundary. It is thought that this is because the outer boundary is 2K hotter than the inner boundary which shifts the maximum point of the temperature profile towards the outer boundary.

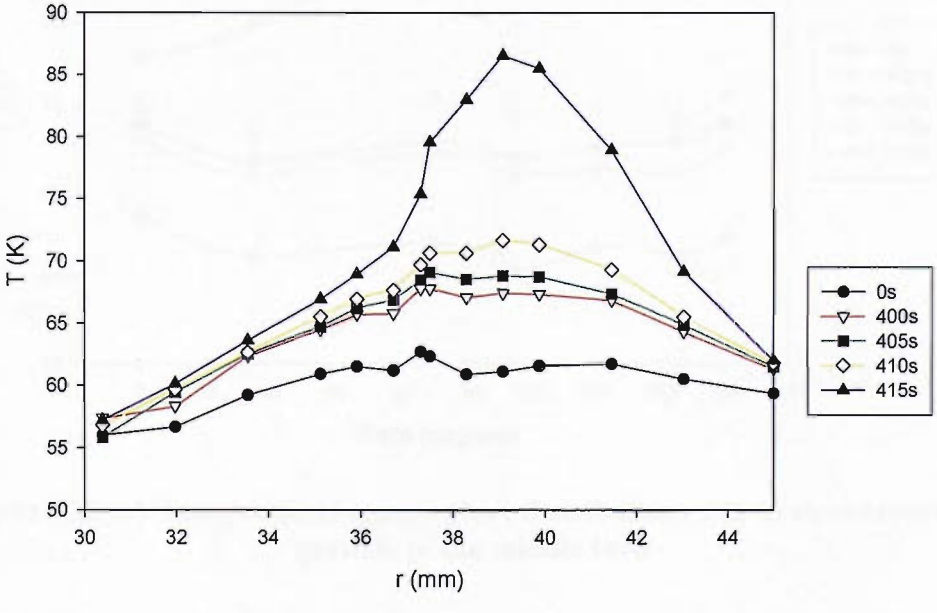

Figure 4.21 (a): Radial temperature distributions due to an overcurrent quench, at theta is 180°

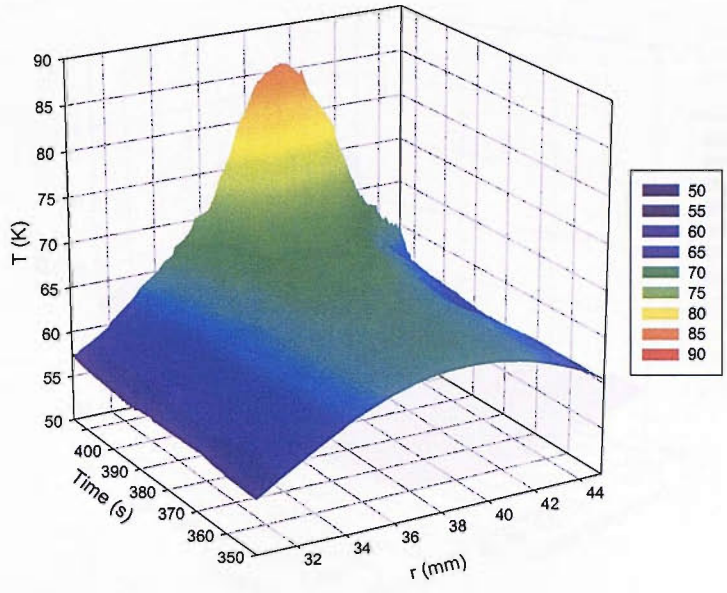

Figure 4.21 (b): 3-D mesh of the radial temperature distributions due to an overcurrent quench, at theta is 180°

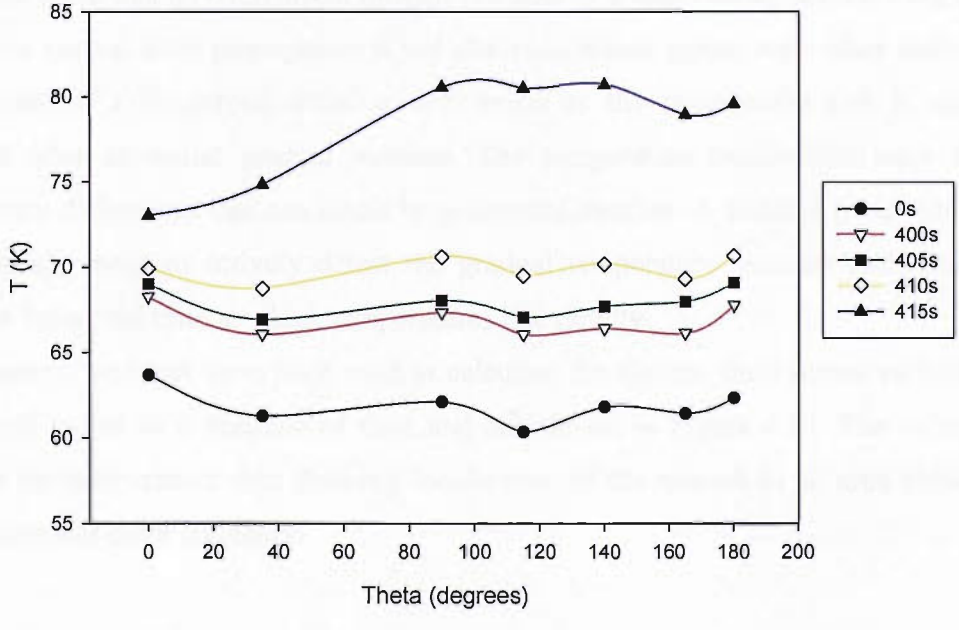

Figure 4.22 (a): Longitudinal temperature distributions due to an overcurrent quench, of the middle turn

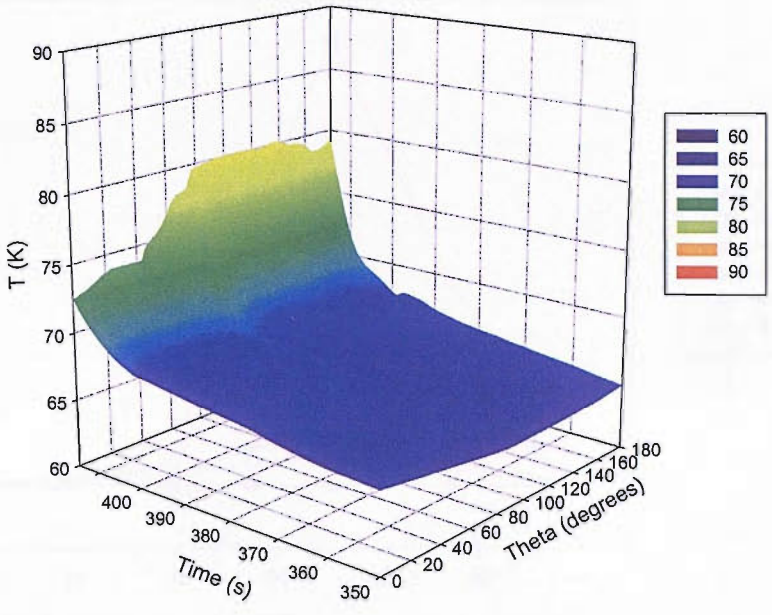

Figure 4.22 (b): 3-D mesh of the longitudinal temperature distributions due to an overcurrent quench, of the middle turn

It must be noted that an overcurrent quench is a case of a quasi-steady overheating and that distinctive normal zone propagation is not observed which agrees with other authors tests [13]. However a dangerous situation still exists as the temperature rise is rapid and localised after an initial gradual increase. The temperature localisation leads to large temperature differences that can cause large thermal stresses. A suitable protection system would ideally need to actively detect the gradual temperature increase and initiate coil rundown before the time at which temperatures rise rapidly.

The measured voltages have been used to calculate the electric field across various points of the coil radius as a function of time and are shown in Figure 4.23. The voltage data supports the temperature data showing localization of the quench to an area between the middle turn and outer boundary.

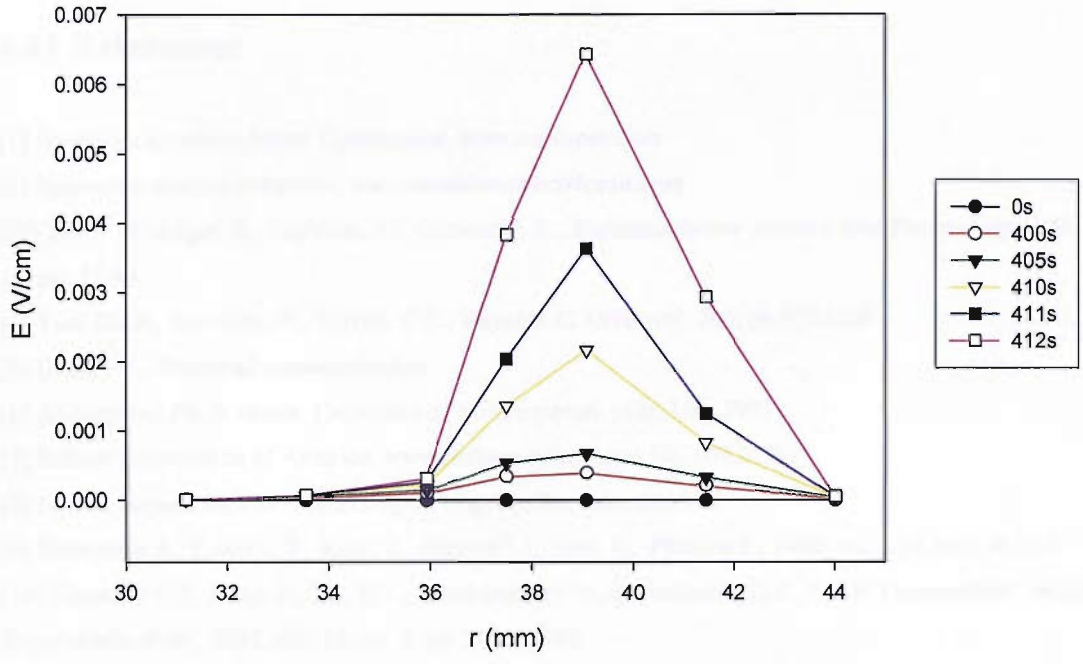

Figure 4.23: Radial electric field distribution

4.10 Conclusion

A conduction cooled pancake coil wound with a (BiPb)2223 tape conductor has been manufactured using a vacuum impregnation process. The highly instrumented coil has been characterised by measuring the current-voltage curves and the quench current as a function of operating temperature. The critical current across the entire length of the coil was determined from the measured current-voltage curves and a procedure presented to predict the critical current as a function of operating temperature. It was shown that the conduction cooled coil was less tolerant to a steady overcurrent than when cooled in a bath of liquid nitrogen. The temperature and voltage distributions were mapped during the evolution of a quench caused by an overcurrent. It was observed that the quench initially evolves due to a steady heating of the entire coil, although, localisation of the temperature distribution occurs as heating rates increase due to insufficient time for heat diffusion.

4.11 References

[1] American Superconductor Corporation, ***www.amsuper.com***

[2] Sumitomo electric industries, ***www.sumitomoelectricusa.com***

[3]Vase, P., Flukiger, R., Leghissa, M., Glowacki, B., ***Superconductor Science and Technology***, 2000, vol. 13, pp. 71-84

[4] Yau, J.K.F., Savvides, N., Sorrell, C.C., ***Physica C***, 1996, vol. 266, pp.223-229

[5] Dudley R., ***Personal communication***

[6] Al-Mosawi, ***Ph.D. thesis***, University of Southampton, year, UK, 1997

[7] Indium Corporation of America, ***www.indium.com***, Form No. 97622 R6

[8] Nordic Superconductor Technologies, ***Application note 0010v01***

[9] Kobayashi S., Kaneko, T., Kato, T., Fuikami, J., Sato, K., ***Physica C***, 1996, vol. 258, pp.336-340

[10] Chandler J.G., Jiang, J., Cai, X.Y., Schwartzkopf A., Larbalestier, D.C, ***IEEE Transactions on Applied Superconductivity***, 2003, vol. 13, no. 2, pp. 2945-2948

[11] Majoros, M., Glowacki, B.A., Campbell, A.M., ***Superconductor Science and Technology***, 2001, vol. 14, pp.353-362

[12]Gmelin, E., Assen-Palmer, M., Reuther, M., Villar, R., ***Journal of Applied Physics D***, 1999, vol.32, pp.19–43

[13] Ilyin Yu.A., Vysotsky, V.S, Kiss, T., Takeo, M., Okamoto, H., Irie, F., ***Cryogenics***, 2000, vol. 41, pp. 665-67

Chapter 5 : Formation and propagation of a normal zone in a (BiPb)2223 conduction cooled pancake coil

5.1 Introduction

The concept of a minimum propagating zone (MPZ), as discussed in Chapter 2, was first proposed by Wipf and Martenelli [1]. It is a measure of how sensitive a superconductor is to applied energy pulses [2] and has been successfully used to investigate the thermal stability of LTS magnets. If a disturbance in the coil winding causes a normal zone to form with a size that is everywhere greater than the MPZ then the normal zone will propagate and the coil will quench. The minimum quench energy (MQE) is the minimum energy needed to initiate a quench in a winding and therefore gives a measure of the stability of the winding to point disturbances. The MQE of HTS coils has been shown to be of the order of joules [3,4]. Despite the high stability of these coils their response to transient thermal disturbances must be better understood so that the stability of magnet designs can be accurately evaluated and adequate protection systems designed. The analysis of the formation and propagation of a normal zone in a HTS coil is complex because a quench occurs over a wide temperature range where the properties of the coil composite are highly temperature dependent. This chapter investigates the formation and propagation of a normal zone in a conduction cooled 38 turn (BiPb)2223 pancake coil operating between 35K and 74K. The detail of the design, manufacture, and steady state characterisation of the coil has previously been presented in chapter 4.

5.2 Experimental

5.2.1 Set-up

The 38 turn (BiPb)2223 pancake coil was mounted into the test apparatus as described in Section 4.5. The experimental layout showing the test coil and connected auxiliaries is detailed in Figure 5.1. It is essential that a controlled energy pulse is applied to the

constantan heater (R_{heater} [Ω]) embedded in the test coil so that the quench energy can be accurately determined. To accomplish this a 40Hz sinusoidal waveform from a frequency generator was modulated by a square wave pulse lasting about 1s provided by a pulse generator. The power of the heat pulse could be varied by adjusting the gain of the audio amplifier.

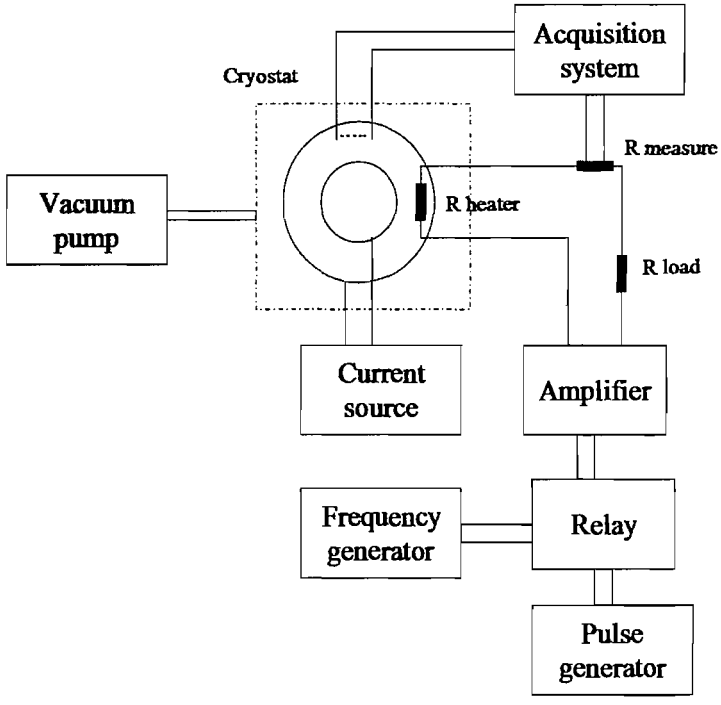

Figure 5.1: Experimental set-up

The heater resistance is required to calculate the energy produced by the heater. The resistance of the 25mm, 60mm and 125mm heated sections were measured as a function of operating temperature using the 4 point resistance method. It was observed that the heater resistance of each length varied by a maximum of 0.36% in the 43K to 60K temperature range and therefore the resistance was assumed constant over the temperature range of interest. The heater resistance as a function of heater length can be seen in Figure 5.2. The resistance for the 200mm length was extrapolated using the fitted regression line.

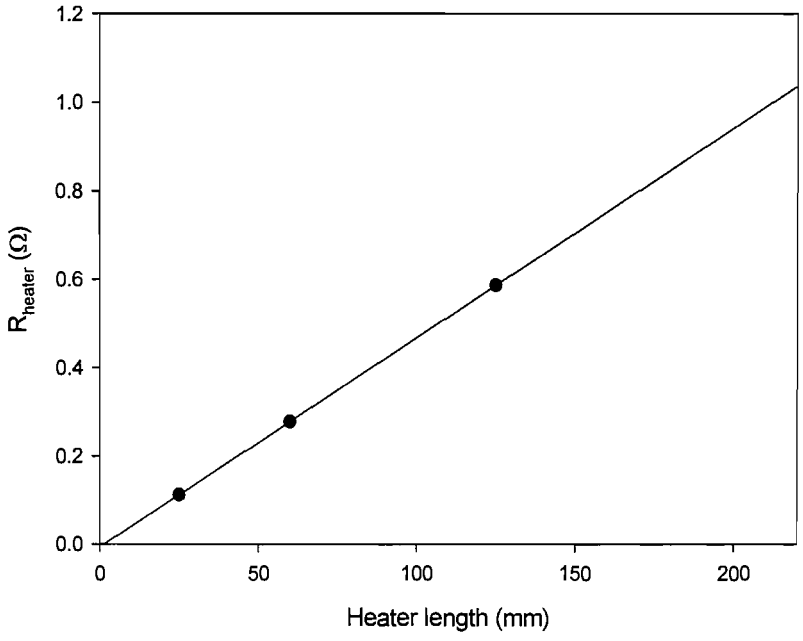

Figure 5.2: Heater resistance as a function of heater length

For each test the coil boundaries were set at a given temperature between 35K and 74K, and an appropriate transport current was applied that produced an average electric field of 0.7μV/cm across the ends of the coil. This electric field was chosen because it allowed the coil to recover quickly after an energy pulse that failed to initiate a quench. Upon reaching the steady state for a given temperature and transport current, a transient heating pulse was applied to a defined heated segment (25mm, 60mm, 125mm and 200mm) of the constantan heater to simulate both local and distributed heating. The current leads for the different heated sections are positioned symmetrically about the middle of the heater. The balance between a quench and recovery is determined by incrementally increasing the energy of the heating pulses until a quench is initiated as shown in section 5.2.2 below. The coil is left to fully recover after each heat pulse is applied. The minimum energy required to initiate a quench is denoted as the quench energy, E_Q [J]. Once a quench is initiated, to prevent overheating of parts of the coil, the current supply was programmed to cut out once a set voltage across the quenched coil was reached. This voltage was obtained by gradually increasing the voltage limit until a maximum temperature of between 130K and 150K was reached during a quench.

5.2.2 Determination of the quench energy

To determine the quench energy a series of measurements using successively increasing values of heat pulse energy were acquired, an example of which is shown in Figure 5.3. For the example presented the coil boundaries were set at 35K and heat pulses were applied to a 25mm heater section. The transient temperature response of the middle turn adjacent to the heater (turn 19) and a point 2 turns radially outwards (turn 21) are shown. From Figure 5.3 it can be seen that the coil recovers when heat pulses of 14.5J and below are applied. A quench is initiated when a heat pulse of 14.9J is applied; the quench energy is therefore between 14.5J and 14.9J. The results show good repeatability between each test run indicating that the coil temperatures return to the same temperature after a quench and that reproducible heat pulses are applied to the coil.

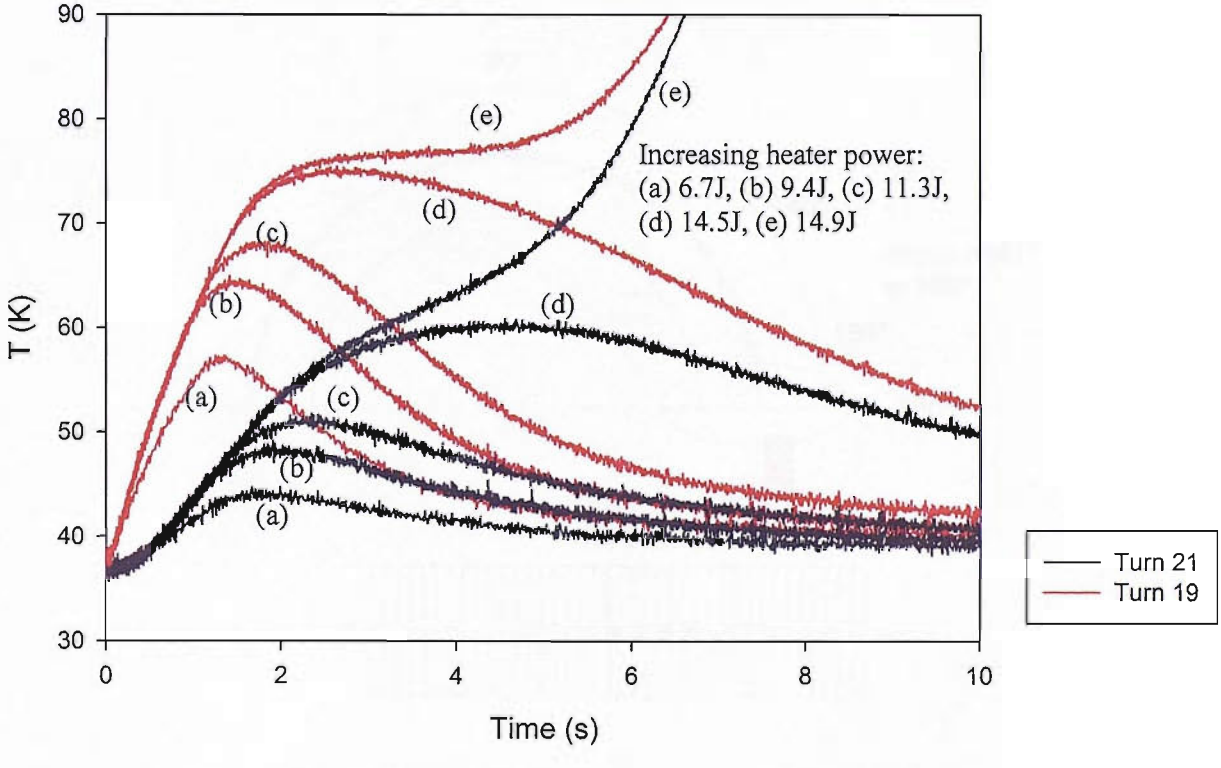

Figure 5.3: Determination of the quench energy

5.2.3 Normal zone formation

With the coil boundaries operating at 67K a quench was initiated by applying a 25.3J heat pulse to a heated section 25mm long. The previously applied heat pulse of 22.3J failed to initiate a quench indicating the applied energy approximates the quench energy. Figure 5.5 and Figure 5.6 detail both the temperature and voltage response of the coil at various taps distributed across the coil radius and along the middle turn respectively. The time for which the heat pulse is applied has been indicated by the shaded section at the beginning of each measurement. The positions of the measurement taps are detailed in Figure 5.4 and inset into Figure 5.5 and Figure 5.6. To enable comparison between different sections of the coil the voltages have been converted to electric field values. This is achieved by dividing the measured voltages by the conductor length between voltage taps.

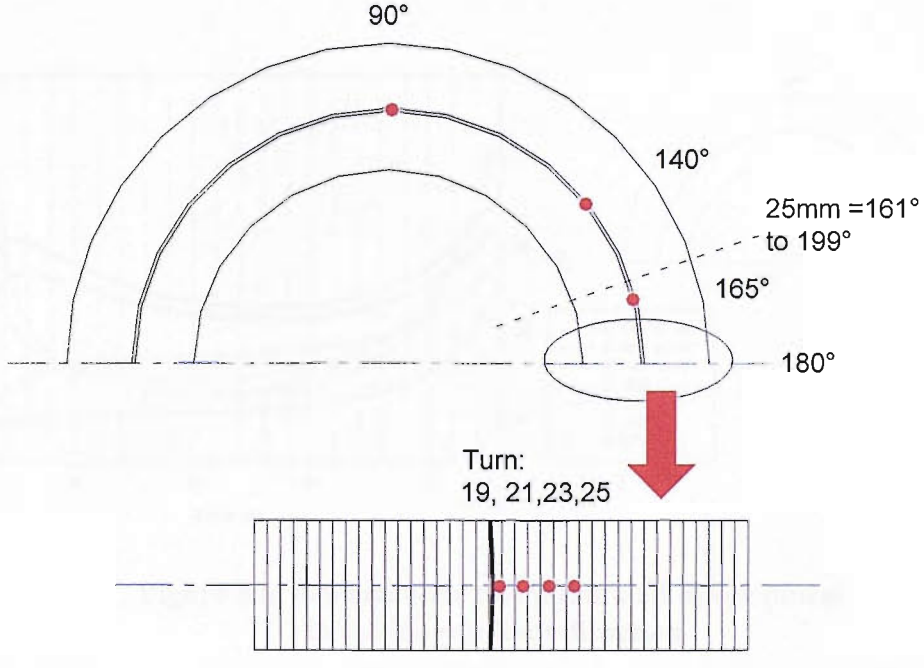

Figure 5.4: Positioning of temperature and voltage taps

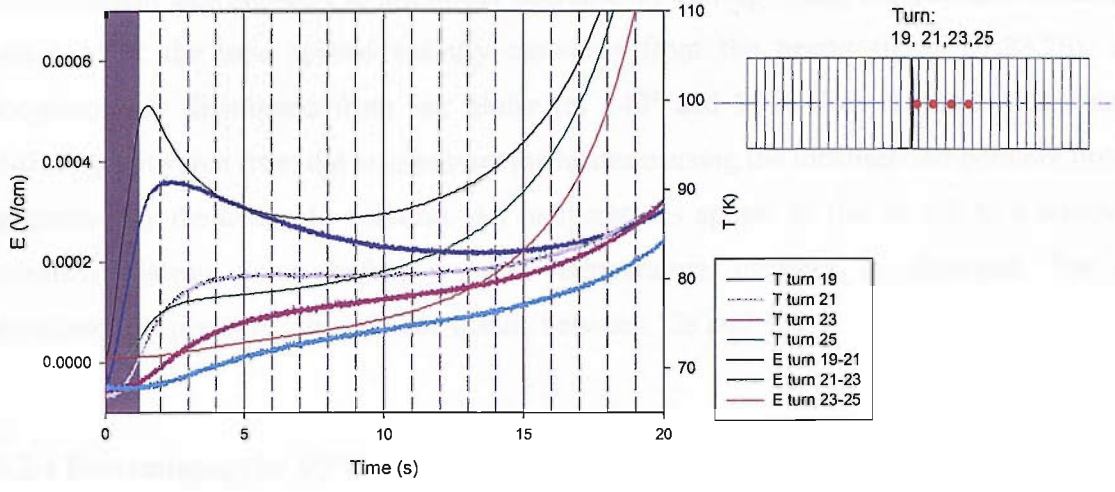

Figure 5.5: Normal zone formation and development in the radial direction

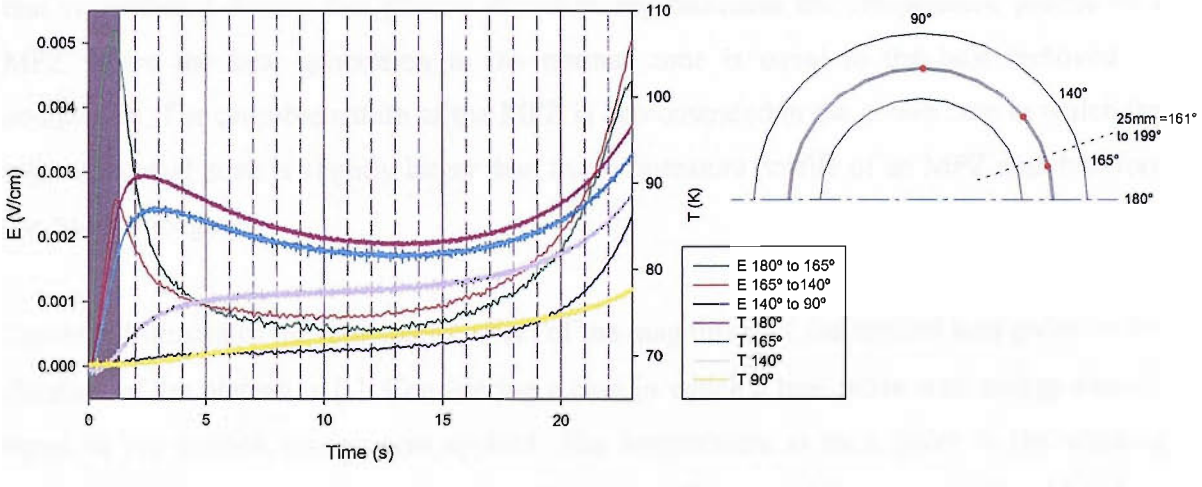

Figure 5.6: Normal zone formation and development in the longitudinal direction

For the measurements shown in Figure 5.5 and Figure 5.6 it is observed that the heat pulse initially generates a temperature profile that is radially localised to the middle turn and longitudinally localised to the length of the heater. The measurement taps adjacent to the heater (turn 19 at 180° and 165°) experience a rapid temperature and voltage rise correlated to the duration of the heat pulse. All other taps exhibit a gradual heating that continues after

the end of the heat pulse. After the heat pulse is removed the temperature of the measurement taps adjacent to the heater decrease. A corresponding temperature increase is observed at the taps spaced radially outwards from the heater (turns 21,23,25), and longitudinally distributed from the heater (at 140° and 90°). This indicates that heat is diffusing outwards from the area around the heater causing the localised temperature profile generated by the heater to collapse. All temperatures appear to rise or fall to a relatively constant plateau value before a rapid temperature increase is observed. For the measurement presented this plateau occurs between 12s and 15s.

5.2.4 Determining the MPZ

Examining the plateau observed in Figure 5.5 and Figure 5.6 it can be seen that all temperatures are approximately constant during the time over which the plateau exists indicating that heat generation is approximately equal to cooling. The temperature profile that is produced during this plateau therefore approximates the temperature profile of a MPZ where the heat generation in the normal zone is equal to the heat removed by conduction. The unstable nature of the MPZ is demonstrated in the above case in which the applied normal zone is slightly larger than the temperature profile of an MPZ and therefore the zone propagates.

Figure 5.7 illustrates the anticipated effect of the magnitude of the applied heat pulse on the duration of the plateau, τ [s]. Considering a case in which a heat pulse with energy exactly equal to the quench energy was applied. The temperature at each point in the winding would stabilise and a steady state temperature profile would be created in which heat generation is equal to cooling. In 'real' quenches the energy of the applied heat pulse would be high enough over the quench energy such that no plateau is observed. Sufficient resolution of the applied heat pulse energy is required so that a temperature plateau is observed. It has been shown that the experimental set-up has a satisfactory resolution to observe the temperature plateau.

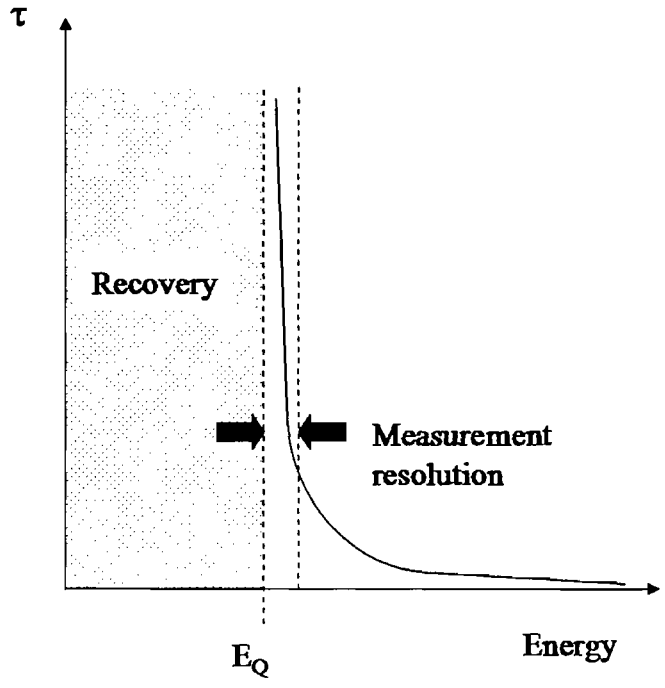

Figure 5.7: Effect of applied energy on plateau duration

Figure 5.8 demonstrates the effect of operating temperature on the duration of the plateau. At each operating temperature the temperature response of the middle turn (turn 19) at the mid-plane of the heater (180°) to a disturbance 25mm long is shown. At each operating temperature the energy applied is slightly over the quench energy, E_Q, therefore a quench is initiated. It can be seen that duration of the plateau is normally longer when the coil is operated at higher temperatures. This is because at higher operating temperatures the coil is less sensitive to differences between the applied energy and quench energy due to the lower operating current and higher heat capacity.

5.2.5 Experimental limitations

It can be seen from both Figure 5.5 and Figure 5.6 that the temperature and voltage measurements exhibit a similar response to the applied heat pulse. It is observed that the thermal measurements lag behind the voltage by approximately 1 second and the

temperature measurements exhibit less rapid transient behaviour than the voltage measurements. Part of this behaviour can be attributed to the non-linear relationship between voltage and temperature. However, the main cause of this behaviour was due to the method of temperature measurement in which miniature copper coldfingers were soldered to the conductor during coil winding. After epoxy impregnation thermocouples could be soldered to the coldfingers thereby simplifying coil fabrication and installation. The copper coldfingers introduce an additional thermal diffusion path between the conductor and point of measurement causing a slight delay in the dynamic response of the temperature measurement.

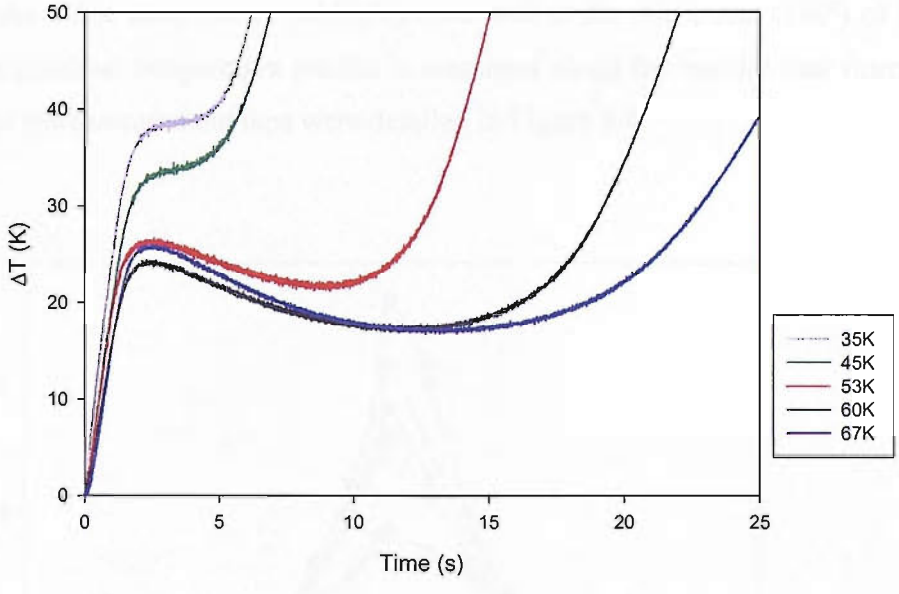

Figure 5.8: Effect of operating temperature on the plateau duration

5.3 Normal zone temperature profiles

The normal zone that approximates the MPZ was determined as a function of operating temperature and heated section length over which the disturbance was applied as described in section 5.2.4 above. The normal zone temperature profiles can aid the magnet designer when examining the effect of continuous and transient disturbances on a winding. For

example a heat load from a resistive joint will cause a temperature profile to form in the winding. If this profile is smaller than the MPZ then the coil will not quench. The temperature profiles also demonstrate the spatial size and maximum temperature of transient disturbances to which the winding is stable that can then, as shown in section 5.4.2, be used to predict the stability of the windings.

5.3.1 Effect of operating temperature on the normal zone temperature profiles

Figure 5.9 and Figure 5.10 show the effect of operating temperature on the normal zone temperature profiles in the radial and longitudinal directions respectively. The results were produced when a disturbance was applied to a 60mm heated section. For all profiles presented the radial temperature profile is measured at the mid-plane (180°) of the heater and the longitudinal temperature profile is measured along the middle turn (turn 19). The positions of the measurement taps were detailed in Figure 5.4.

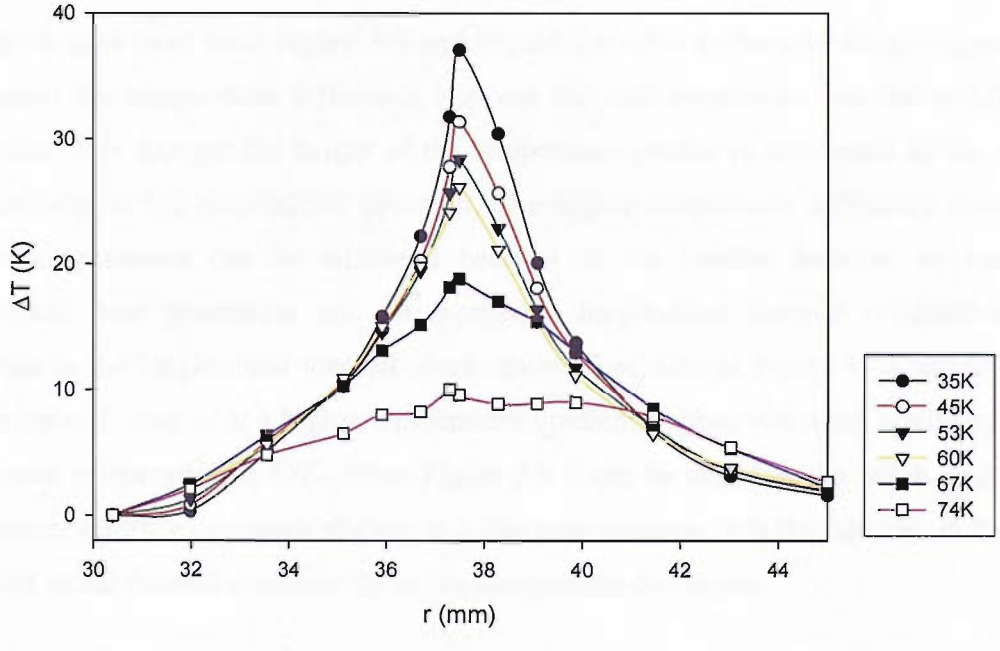

Figure 5.9: Radial normal zone temperature profiles created by a 60mm long disturbance as a function of operating temperature

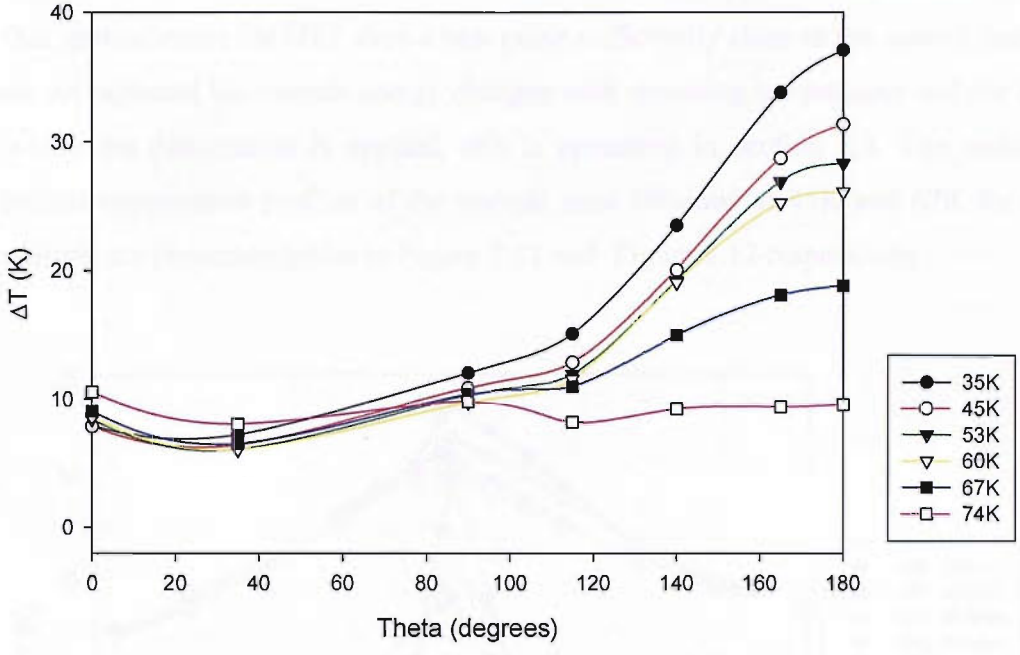

Figure 5.10: Longitudinal normal zone temperature profiles created by a 60mm long disturbance as a function of operating temperature

It can be seen from both Figure 5.9 and Figure 5.10 that as the operating temperature is decreased the temperature difference between the coil boundaries and the middle turns increases. It is thought the height of the temperature profile is dominated by the thermal conductivity in the longitudinal direction. The higher temperature difference observed at lower temperatures can be sustained because of the balance between an increasing volumetric heat generation and an increasing longitudinal thermal conductivity. The increase in the longitudinal thermal conductivity is evident in Figure 5.10 where a larger hotter normal zone with a higher temperature gradient is observed when operating at 35K compared to operation at 67K. From Figure 5.9 it can be seen that the width of the radial temperature profile decreases slightly at lower temperatures. It is thought this is due to the reduced radial thermal conductivity as the temperature decreases.

5.3.2 Effect of disturbance length on the normal zone temperature profiles

The effect of varying the disturbance length on the shape of the normal zone that approximates the MPZ was investigated. To obtain the temperature profiles of the normal

zone that approximates the MPZ then a heat pulse sufficiently close to the quench energy is applied. As expected the quench energy changes with operating temperature and the length over which the disturbance is applied, this is presented in section 5.4. The radial and longitudinal temperature profiles of the normal zone obtained at 45K and 67K for every heater length are presented below in Figure 5.11 and Figure 5.12 respectively.

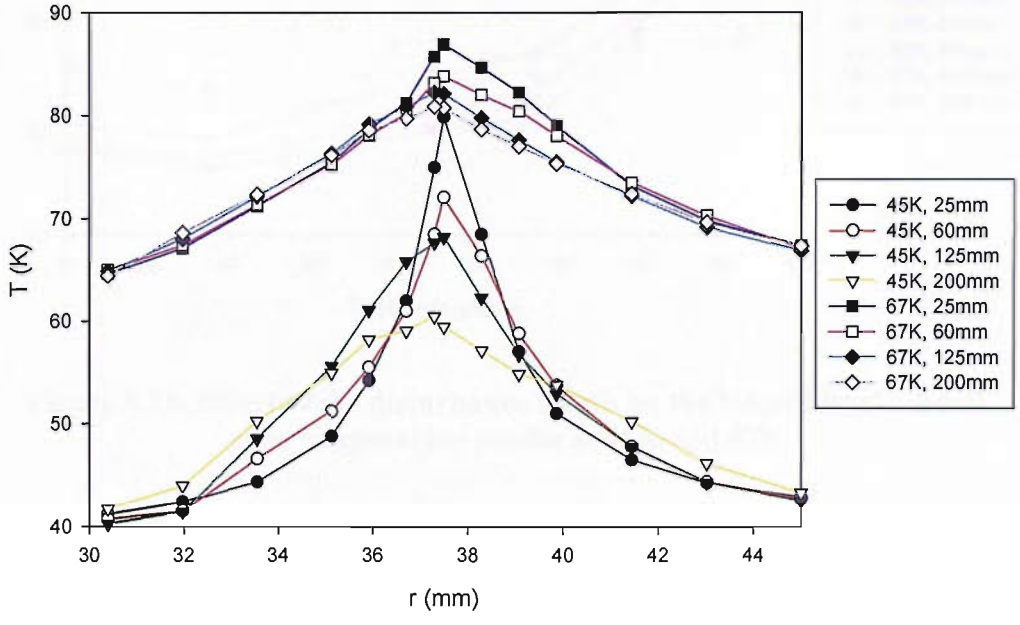

Figure 5.11: Effect of the disturbance length on the radial normal zone temperature profile at 45K and 67K

It can be seen that as the length of the heated section increases the size of the normal zone grows in both the radial and longitudinal directions. The heat removed at the end of the zone is therefore decreasing compared to the normal zone volume. To maintain a balance between heat generation and cooling the heat generation per unit volume must decrease. This is evidenced by the lower temperature difference between the middle turns and the coil boundaries when examining the longer heated lengths. At lower temperatures the effect of the disturbance length on the temperature profiles becomes more evident. The higher volumetric heat generations present at lower temperatures makes the coil more sensitive to changes in the disturbance length.

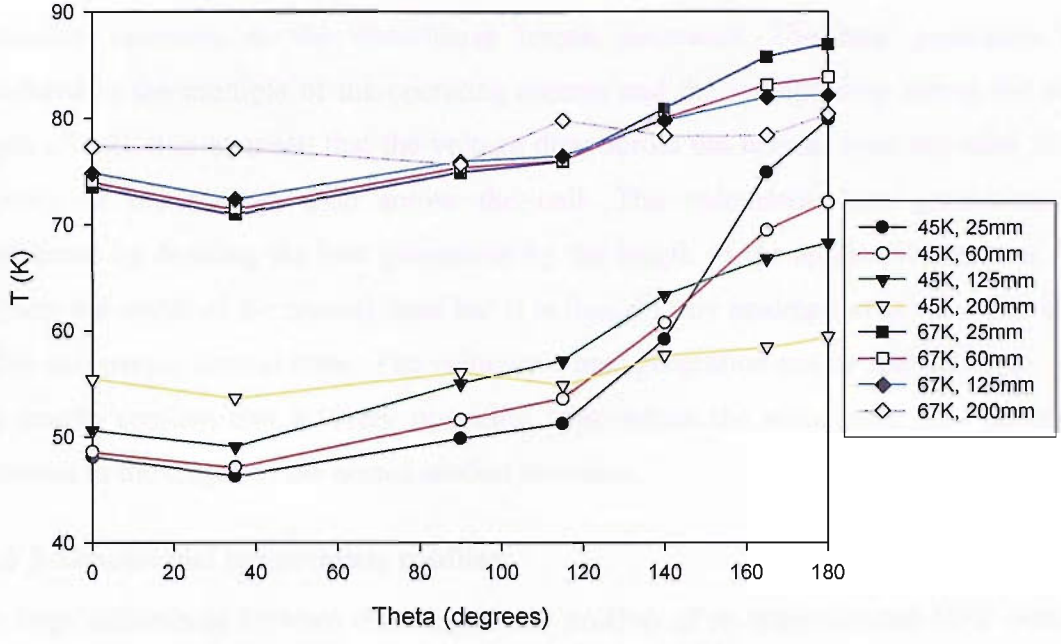

Figure 5.12: Effect of the disturbance length on the longitudinal normal zone temperature profile at 45K and 67K

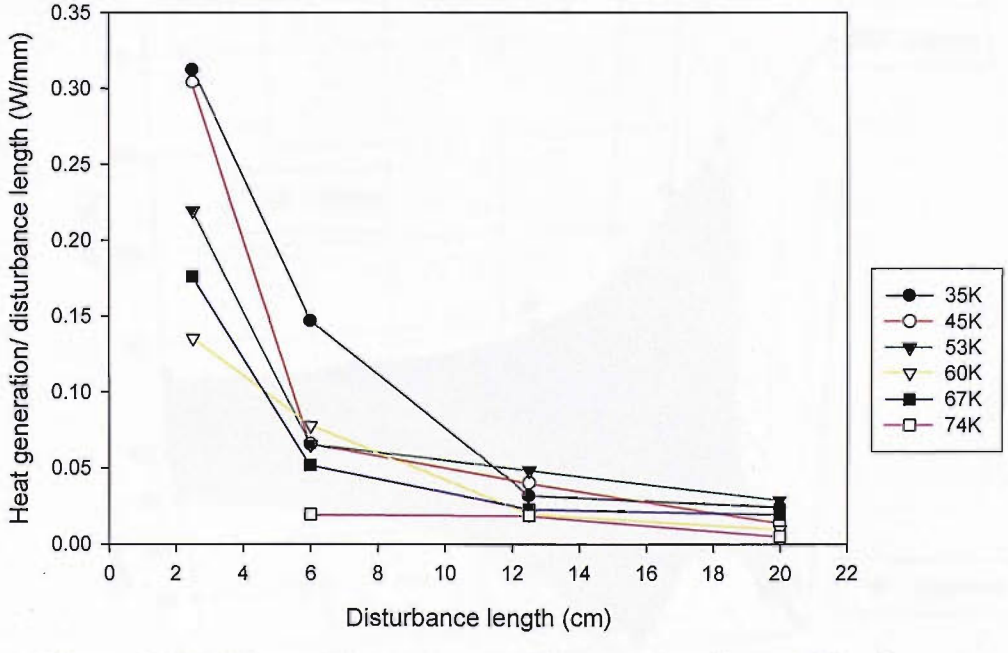

Figure 5.13: Volumetric heat generation as a function of disturbance length and operating temperature

The heat generated by the normal zone was measured to confirm that the volumetric heat generation increases as the disturbance length decreases. The heat generation was calculated as the multiple of the operating current and the voltage drop across the entire length of coil. It is assumed that the voltage drop across the normal zone accounts for the majority of the voltage drop across the coil. The volumetric heat generation was represented by dividing the heat generation by the length of the applied disturbance. This neglects the width of the normal zone but it is thought this assumption is valid due to the highly anisotropic normal zone. The volumetric heat generation can be seen in Figure 5.13. The results confirm that at every operating temperature the volumetric heat generation decreases as the length of the heated section increases.

5.3.3 3-dimensional temperature profiles

The large differences between the temperature profiles of an approximated MPZ obtained at 35K with a 25mm heater length and at 74K with a 200mm heater length are illustrated in

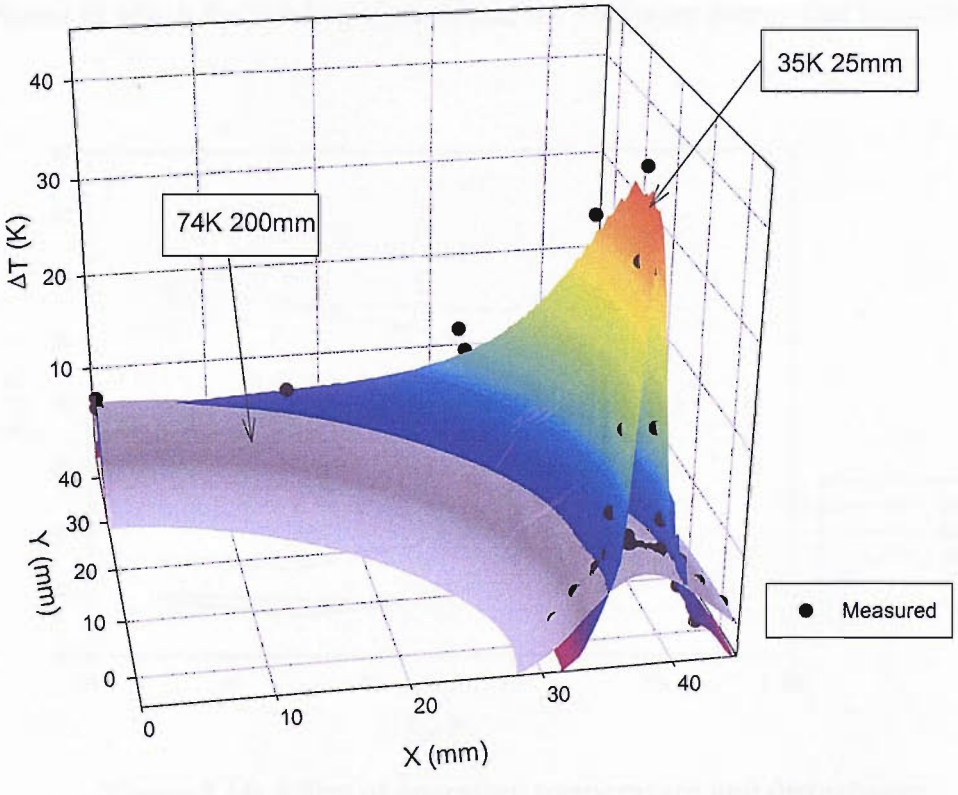

Figure 5.14: Difference in MPZ temperature profiles. E_Q at 35K 2.5cm is 14.9J, at 74K 20.0cm E_Q is 45.6J

Figure 5.14 below. Measured temperatures are presented and to aid comparison a 3-dimensional mesh is fitted to each set of experimental results. The localised temperature profile generated at 35K can be clearly seen compared to the distributed temperature profile produced at 74K. The results indicate that coils operating at lower temperatures can sustain small localised heat inputs because of the increase in thermal conductivity as temperature is decreased down to approximately 25K.

5.4 Quench energy

5.4.1 Effect of operating temperature and disturbance length

The quench energy was determined as a function of operating temperature, T_{OP} [K], and as a function of the heated section length over which the disturbance was applied. Figure 5.15 presents the quench energy as a function of operating temperature for various disturbance lengths. The experimental resolution is indicated by showing the maximum energy of a disturbance to which the winding is stable and the minimum energy that initiates a quench.

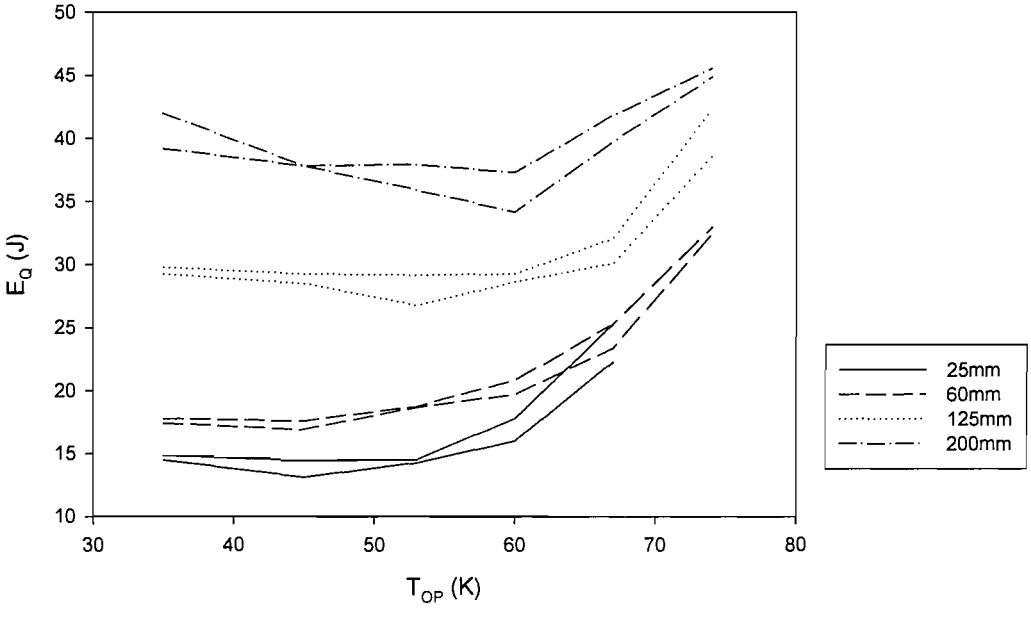

Figure 5.15: Effect of operating temperature and disturbance length on the measured quench energy

All measurements were obtained from the second coil that was wound, the details of which were discussed in section 4.3.3. Multiple cooldowns were used to acquire the results over a period of approximately one month. The absence of a measurement at 74K for a 25mm heated section is due to the limited gain of the amplifier.

Effect of temperature

It is observed that the quench energy increases as the operating temperature is increased above 60K. This relationship is expected due to the increased heat capacity of the coil composite and lower operating current at higher temperatures. The experimental results indicate a minimum value of the quench energy between 35K and 60K at each heater length. This is attributed to a sharp increase in Ag thermal conductivity below 60K that counteracts the effect of a decreasing heat capacity. As the temperature is decreased below approximately 25K, at which the thermal conductivity is a maximum, it is anticipated that the quench energy will sharply decrease due to the combined effect of a decreasing thermal conductivity and a rapid reduction in heat capacity. The quench energy obtained when a 200mm long disturbance is applied increases as the operating temperature is decreased below 50K. This increase is not observed at shorter heater lengths and is thought to be due to the effect that the heat capacity has on the quench energy. At longer heater lengths the temperature rise that is required to form a MPZ is significantly smaller than at shorter heater lengths. The quench energy is therefore affected more by the increasing thermal conductivities than by the heat capacity causing the rise in quench energy at lower temperatures.

Effect of disturbance length

It can be seen from Figure 5.15 that the quench energy increases as the length of the disturbance increases. This can be seen more clearly in Figure 5.16 where the quench energy is re-plotted as a function of the disturbance length for various operating temperatures. As Wilson [5] reported the quench energy at disturbance lengths longer than the MPZ is determined by the energy per unit volume. The quench energy should therefore increase as the disturbance length increases beyond the MPZ length. From Figure 5.16 it can be seen that the measured quench energy increases as the disturbance length increases

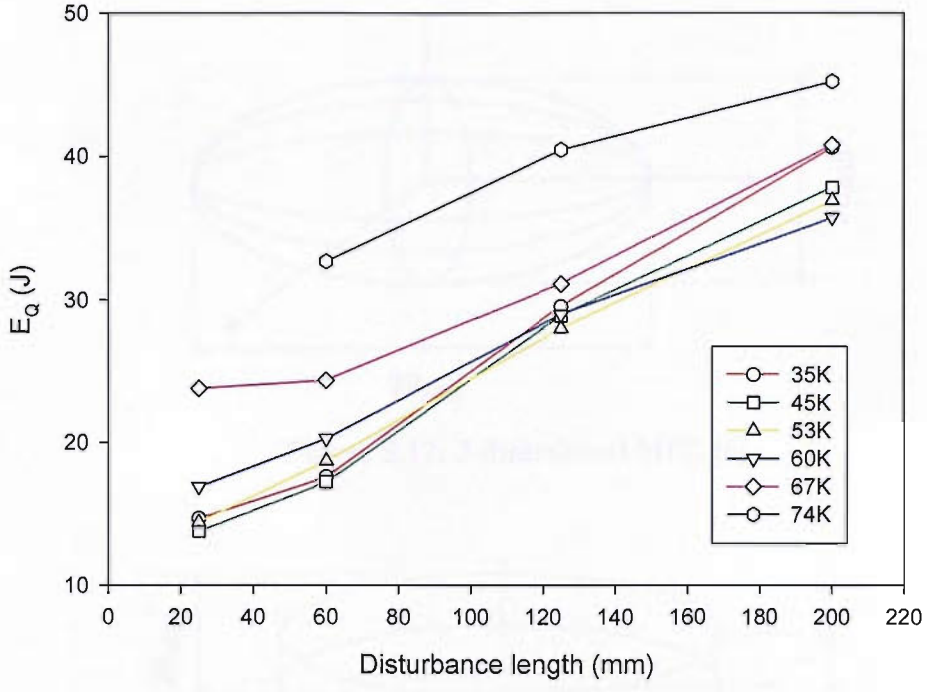

Figure 5.16: Quench energy dependence on disturbance length

as predicted. It is difficult to infer the MPZ size from Figure 5.16 and therefore it is best to examine the normal zone profiles as shown in section 5.3. The MQE can be estimated by extrapolating the curves in Figure 5.16 to a disturbance length of 0mm to represent a point disturbance. For all comparisons against predicted values the quench energy for the 25mm disturbance length will be used as the MQE.

5.4.2 Analytical confirmation of the stability minimum point

To confirm the trend of the experimental results the minimum quench energy was calculated by modifying a treatment reported by Iwasa [6]. Iwasa estimates the size of a 3-dimensional ellipsoidal MPZ in an adiabatic winding, as shown in Figure 5.17, by balancing the heat generated in the normal zone by the heat removed through conduction. The treatment must be modified to account for the 2-dimensional shape of the normal zone that is produced in a pancake coil, as shown in Figure 5.18.

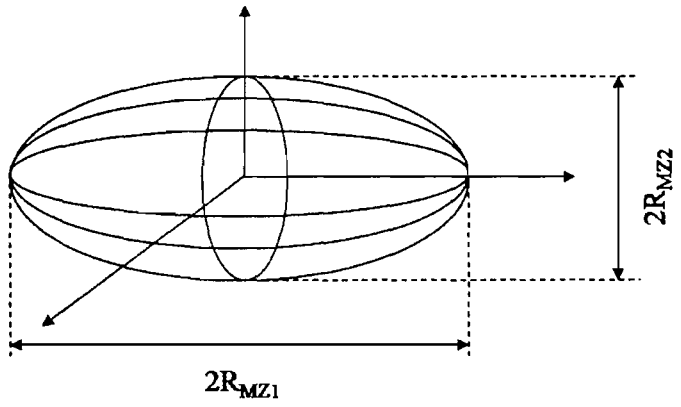

Figure 5.17: 3-dimesional MPZ [6]

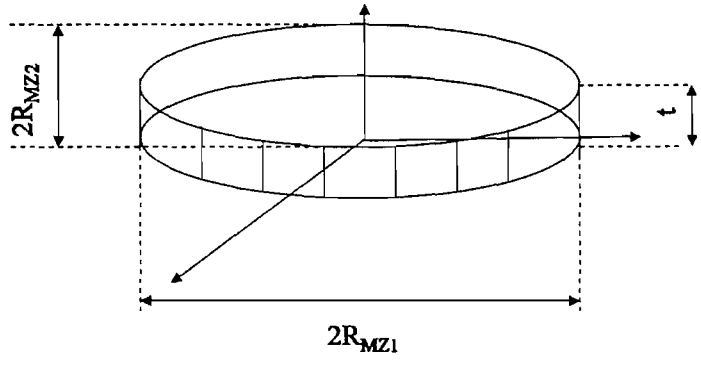

Figure 5.18: 2-dimensional MPZ in a pancake coil

Equations 5.1, 5.2, and 5.3 are used to calculate the length, radius and volume of the MPZ respectively. The thickness of the MPZ is taken as the width of the conductor which is 4mm. The MQE is calculated as the energy needed to raise the entire MPZ volume to the critical temperature as shown in Equation 5.4. The nomenclature for symbols used in the MQE estimation is shown in Table 5.1. In the calculation it is assumed that the energy to form a MPZ is the minimum energy needed to initiate a quench.

$$R_{MZ1} = \sqrt{\frac{3k_m(T_C - T_{OP})}{\rho_m J_m^{\ 2}}} \quad [\text{m}] \qquad \textbf{Equation 5.1}$$

$$R_{MZ2} = R_{MZ1}\sqrt{\frac{k_{tr}}{k_m}} \quad [\text{m}] \qquad \textbf{Equation 5.2}$$

$$V_{MZ} = \pi R_{MZ1} R_{MZ2} t \quad [\text{m}] \qquad \textbf{Equation 5.3}$$

$$E_Q = V_{MZ} \int_{T_{OP}}^{T_C} C_{wd}\, dT \quad [\text{J}] \qquad \textbf{Equation 5.4}$$

Symbol	Designation
k_m	Thermal conductivity of stabilising matrix [$W.m^{-1}.K^{-1}$]
k_{tr}	Coil radial thermal conductivity [$W.m^{-1}.K^{-1}$]
ρ_m	Resistivity of the stabilising matrix [$\Omega.m$]
T_C	Critical temperature of (BiPb)2223 [K]
T_{OP}	Operating temperature [K]
J_m	Current density in stabilising matrix [$A.m^{-2}$]
R_{MZ1}	Longitudinal MPZ size [m]
R_{MZ2}	Radial MPZ size [m]
t	MPZ thickness [m]
V_{MZ}	MPZ volume [m^3]
C_{wd}	Volumetric heat capacity of the coil winding [$J.m^{-3}.K^{-1}$]
E_Q	Minimum Quench Energy [J]

Table 5.1: Nomenclature for MQE derivation

To represent the experimental coil the material properties required in the model were taken from measurements of the coil and published data for the conductor. This data is presented in section 1.5.3. The model accounts for the temperature dependence of the material properties.

It was previously observed that a maximum normal zone temperature significantly lower than the critical temperature is required to initiate a quench. The broad temperature range over which current sharing occurs allows sufficient heat to be generated such that a normal zone can propagate with a maximum temperature below T_C. Measurements detailing the maximum normal zone temperature, T_{MAX} [K], as a function of operating temperature are shown in Figure 5.19. The measurements were acquired when a quench was initiated with a 25mm long disturbance as a function of operating temperature. The quench energy

estimation was further modified to use the value for T_{MAX} in place of T_C and the quench energy as a function of operating temperature estimated as shown in Figure 5.20.

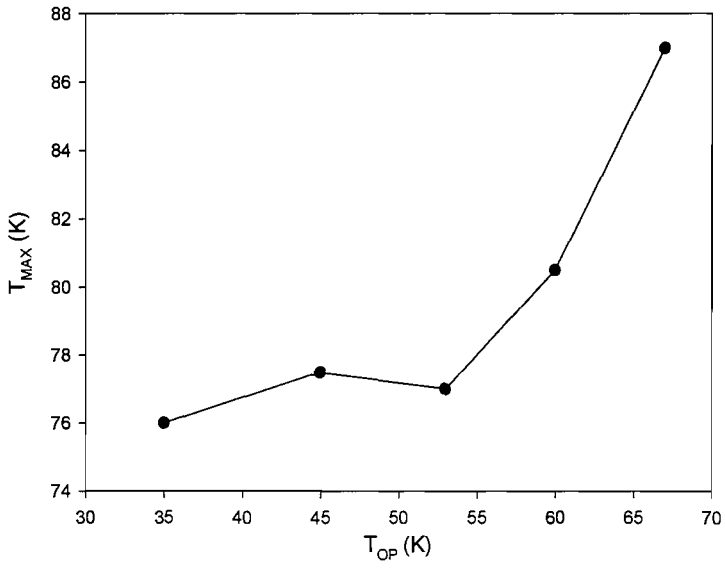

Figure 5.19: Maximum temperature of the MPZ temperature profile, T_{MAX}, as a function of operating temperature, T_{OP}

Comparing the measured and predicted quench energies it can be seen that both show an increase in the quench energy above 60K and a minimum in the quench energy between 35K and 60K. The predicted results show a sharp decrease in the quench energy below approximately 25K which is the temperature at which Ag thermal conductivity is highest. This indicates that the temperature dependence of the thermal conductivity significantly influences the coil stability. The magnitude of the predicted and measured quench energies differ by a maximum of approximately 50% in the 35K to 67K temperature range. The magnitude of the peak in the quench energy at approximately 25K was found to be very sensitive to the value used for the resistivity of the stabilising matrix. The data for the resistivity was obtained from published results for a similar sheath material to that used. The sensitivity of the quench energy estimation coupled with the slight differences in resistivity values may cause the differences between the predicted and measured quench energies.

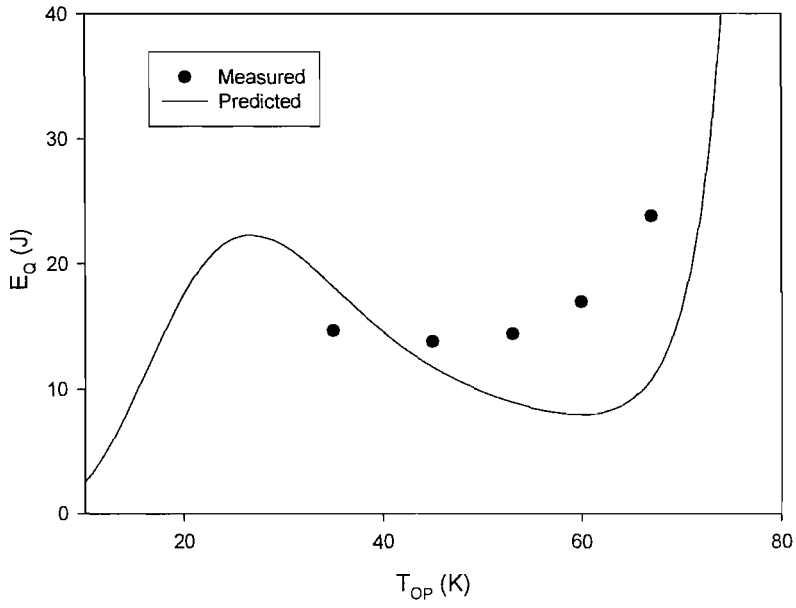

Figure 5.20: Predicted and measured E_Q as a function of operating temperature

MPZ radial width

To confirm the predicted radial MPZ size, R_{MZ2}, follows the same trend as measured values the two results are compared. The radial width of the normal zone that approximates the MPZ was measured by examining the radial voltage profiles as shown in Figure 5.21. This

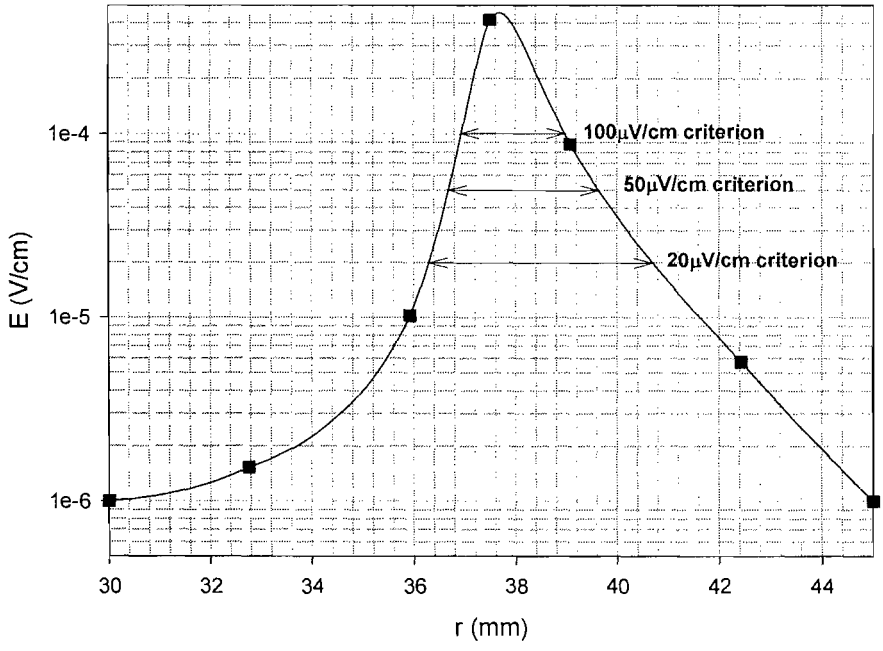

Figure 5.21: Determination of the MPZ width

profile is produced using a 25mm heater length with the coil boundaries set at 35K. The normal zone radial width was taken as any part of the coil above an arbitrary voltage criterion. The measured radial widths at voltage criterion of 20μV/cm, 50μV/cm, and 100μV/cm are compared to the predicted radial width, from Equation 5.2, and presented in Figure 5.22. The normal zone lengths could not be measured in the longitudinal direction due to a lack of measured voltages in this direction.

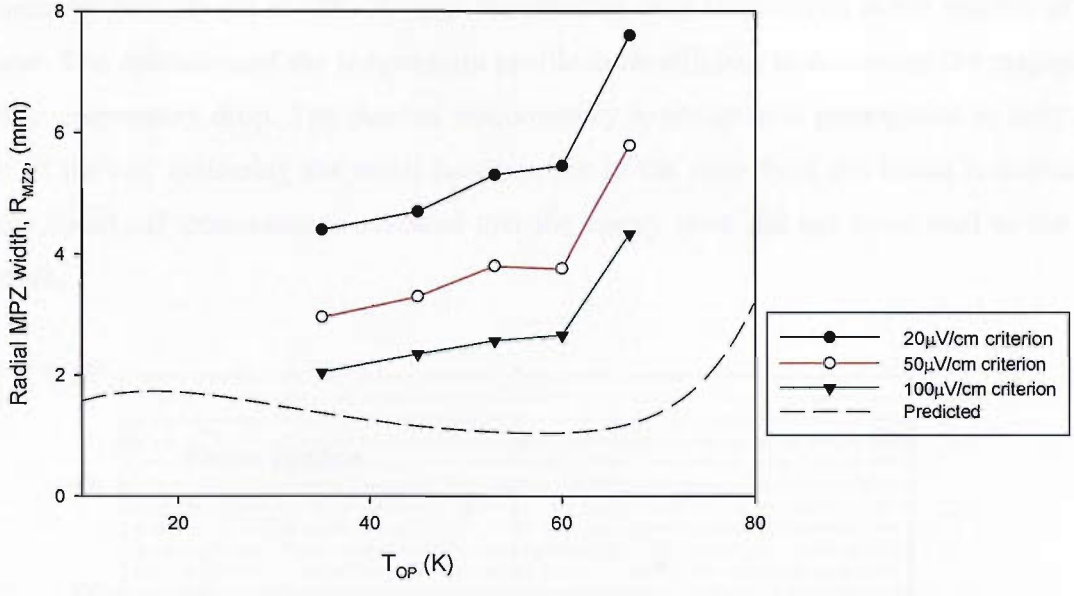

Figure 5.22: Radial MPZ width, R_{MZ2}, as a function of operating temperature

It can be seen from Figure 5.22 that the trend of the measured and predicted values is comparable. In both the measured and predicted values an increase in the measured radial width occurs above 60K. The magnitude of the measured width is highly dependent on the voltage criterion because of the sloping heat generation characteristics of HTS. Radial widths closer to the predicted values are obtained from measurements when 100μV/cm is taken as the voltage criterion

5.5 Quench propagation

5.5.1 NZP anisotropy

The first coil manufactured incorporated a heater that was insulated with paper and applied to the conductor using GE varnish. The radial temperature profiles produced at different times during the propagation of a normal zone were measured, as shown in Figure 5.23. The time is measured from the point at which the start of the heat pulse occurs. The results were obtained when a 25mm heated section was used to initiate a quench with the coil boundaries initially set at 35K. A large temperature drop is observed in the vicinity of the heater. The resolution of the temperature profile is insufficient to determine the magnitude of the temperature drop. The thermal discontinuity limits quench propagation to only one half of the coil indicating the radial heat transfer in the vicinity of the heater is extremely poor. Structural examinations revealed that the epoxy resin did not bond well to the GE varnish.

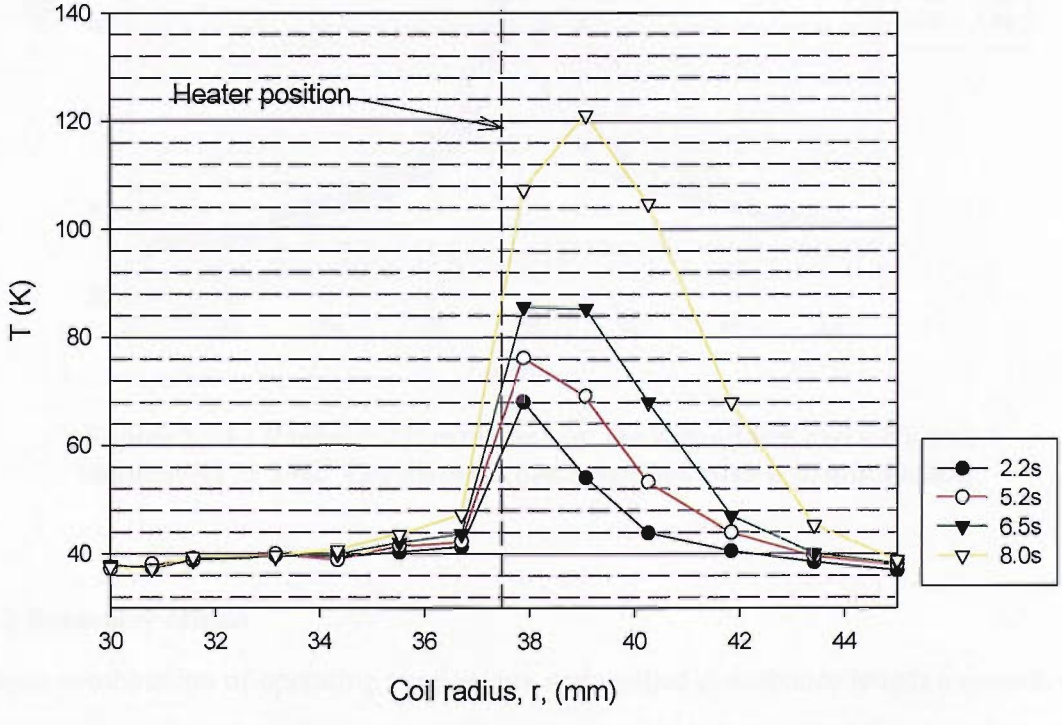

Figure 5.23: Anisotropy of the radial NZP exhibited by the first test coil with coil boundaries at 35K. The disturbance is applied over a 25mm section.

It was decided that the level of anisotropy in the NZP was unacceptable when calculating the NZP velocities and therefore a second coil was manufactured. The heater assembly applied to the second coil was electrically insulated from the conductor by a layer of 40μm fibreglass cloth impregnated with epoxy resin. The radial temperature profiles produced during the propagation of a normal zone in the second coil are shown in Figure 5.24. The results were obtained when a 25mm heated section was used to initiate a quench with the coil boundaries initially set at 35K. It can be seen that the normal zone propagates towards both the inner and outer boundary. A small thermal discontinuity in the vicinity of the heater still exists however it was decided that this level of anisotropy was acceptable when measuring the NZP velocities.

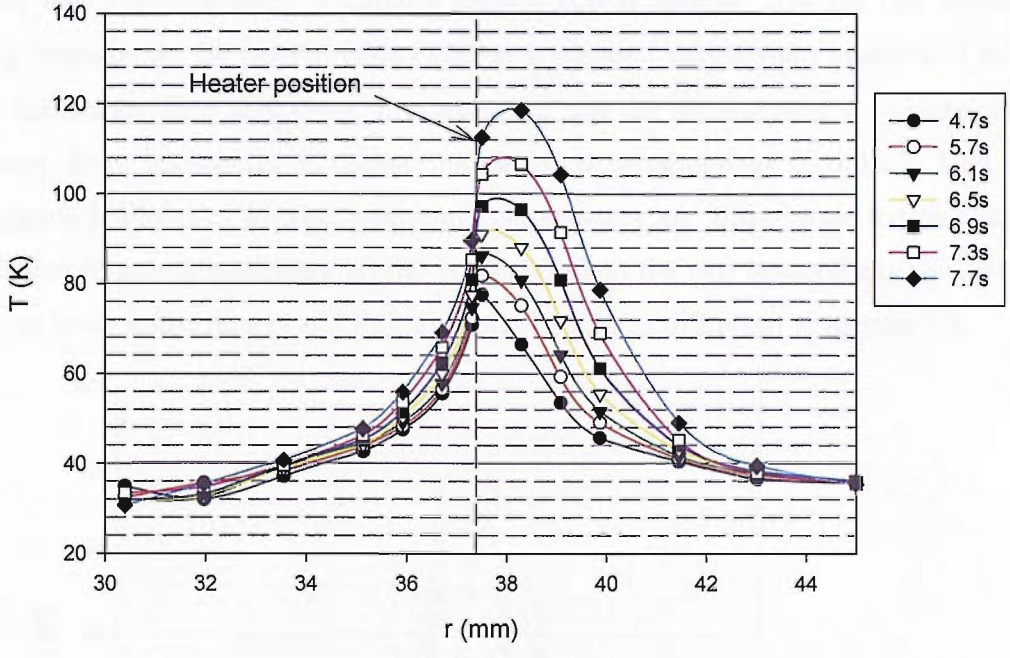

Figure 5.24 : Radial NZP exhibited by the second test coil with coil boundaries at 35K. The disturbance is applied over a 25mm section.

5.5.2 Boundary effects

At each combination of operating temperature and applied disturbance length a quench was initiated using an energy which was sufficiently close to but exceeded the quench energy. The temperature profiles in the radial and longitudinal directions were measured during

propagation. It was found that the coil boundaries significantly affect the temperature profiles during propagation. The boundary effects are investigated below by examining three cases of propagation, an unbounded propagation, a propagation constrained at the radial boundary, and a propagation that is constrained in both the radial and longitudinal directions.

Unbounded NZP

An example of the radial and longitudinal temperature profiles produced during an unbounded quench are shown in Figure 5.25 and Figure 5.26 respectively. The quench was initiated by a disturbance 60mm long with the radial boundaries maintained at 35K. It can be seen that a normal zone is initially formed that is smaller than the coil boundaries. During propagation the normal zone exhibits a constant temperature gradient in both the radial and longitudinal directions. It is observed that the normal zone propagates without influence from boundaries in either the radial or longitudinal directions. Unbounded propagation is observed at other operating temperatures and disturbance lengths when the initial normal zone temperature profile is smaller than the coil boundaries. This generally occurs at lower temperatures and shorter heater lengths as discussed in section 5.3.

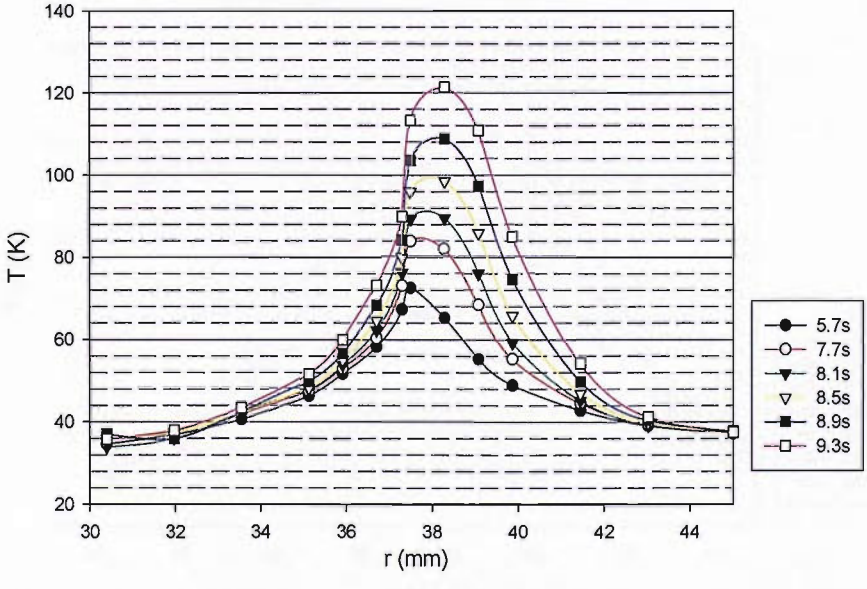

Figure 5.25: Radial temperature profiles during propagation with coil boundaries at 35K. The disturbance is applied over a 60mm section.

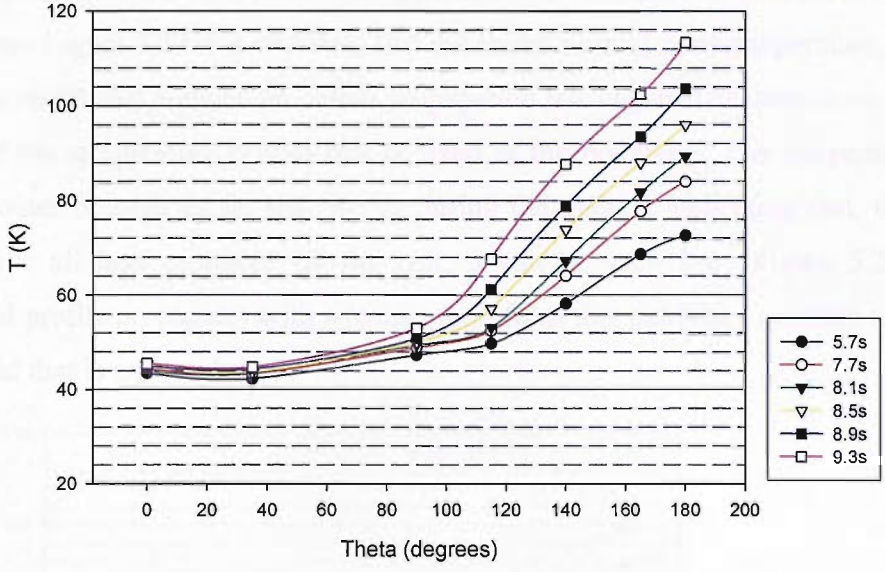

Figure 5.26: Longitudinal temperature profiles during propagation with coil boundaries at 35K. The disturbance is applied over a 60mm section.

Influence of a radial boundary

An example of the radial and longitudinal temperature profiles produced during a quench that is bounded in the radial direction are shown in Figure 5.27 and Figure 5.28 respectively.

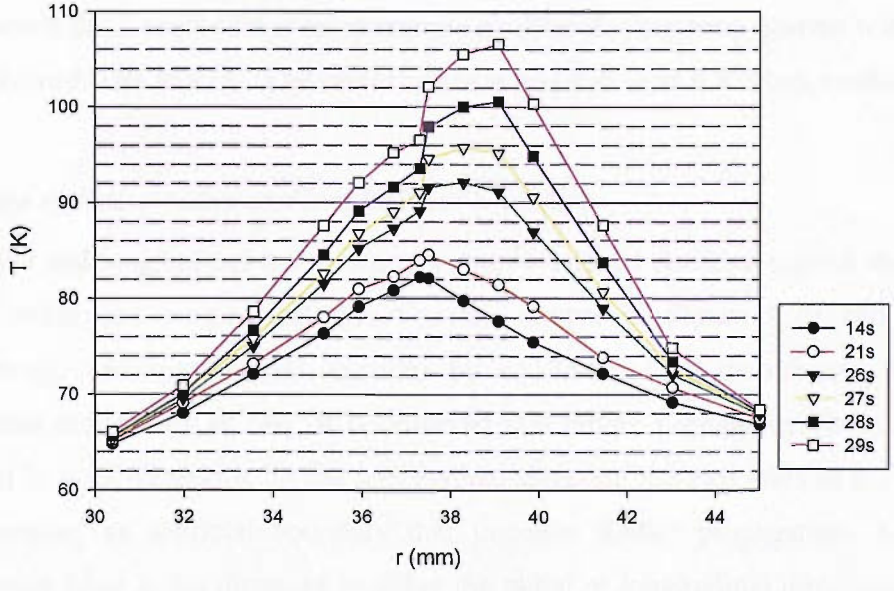

Figure 5.27: Radial temperature profiles during propagation with coil boundaries at 67K. The disturbance is applied over a 125mm section.

The quench was initiated by a 125mm long disturbance with the coil boundaries maintained at 67K. From Figure 5.27 it is observed that the initial normal zone temperature profile has reached the radial coil boundaries before propagation has begun. The quench evolves by an increase of the temperature profile that is fixed at the boundary. The temperature of the inner and outer boundaries do not change during the quench, indicating that, the thermal links remove all heat produced by the coil. It can be seen from Figure 5.28 that the longitudinal profile propagates with a temperature front that exhibits a constant temperature gradient and that is unbounded.

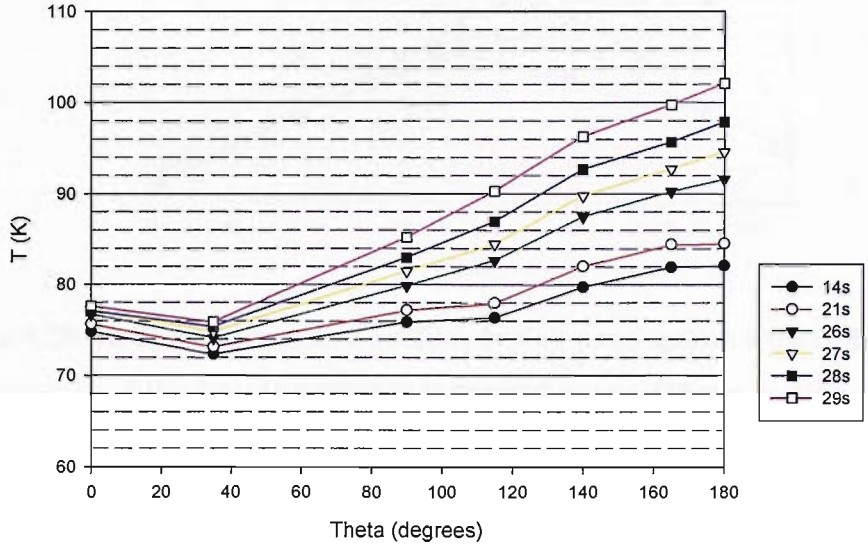

Figure 5.28: Longitudinal temperature profiles during propagation with coil boundaries at 67K. The disturbance is applied over a 125mm section.

Influence of both a radial and longitudinal boundary

The radial and longitudinal temperature profiles produced during a quench that is bounded in the radial and longitudinal direction are shown in Figure 5.29 and Figure 5.30 respectively. The quench was initiated by a 125mm long disturbance with the coil boundaries maintained at 74K. It is observed that before propagation the normal zone is bounded in both directions. In the longitudinal direction the two ends of the normal zone meet creating an artificial boundary that impedes further propagation. A propagating temperature front is not observed in either the radial or longitudinal directions. Instead the

normal zone evolves by a global temperature increase in which the temperature along the middle turn is approximately constant.

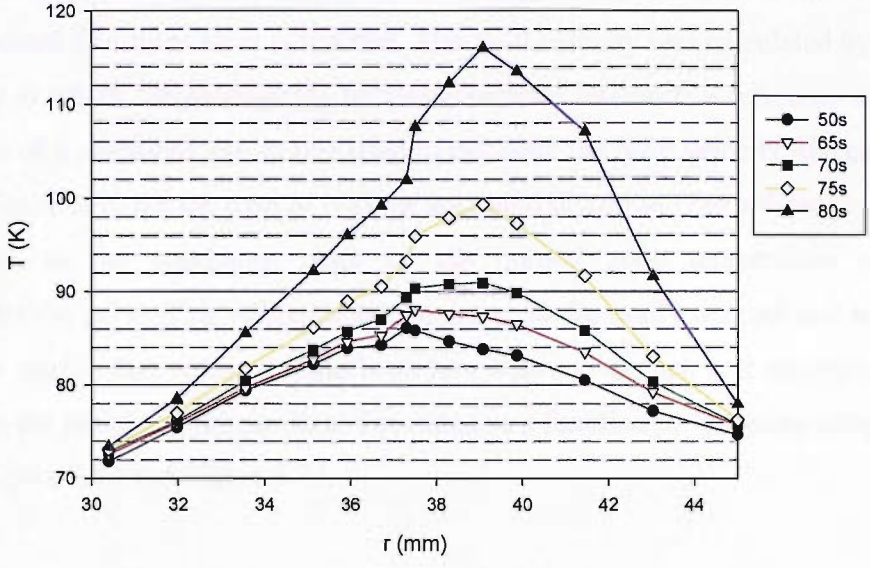

Figure 5.29: Radial temperature profiles during propagation with coil boundaries at 74K. The disturbance is applied over a 125mm section.

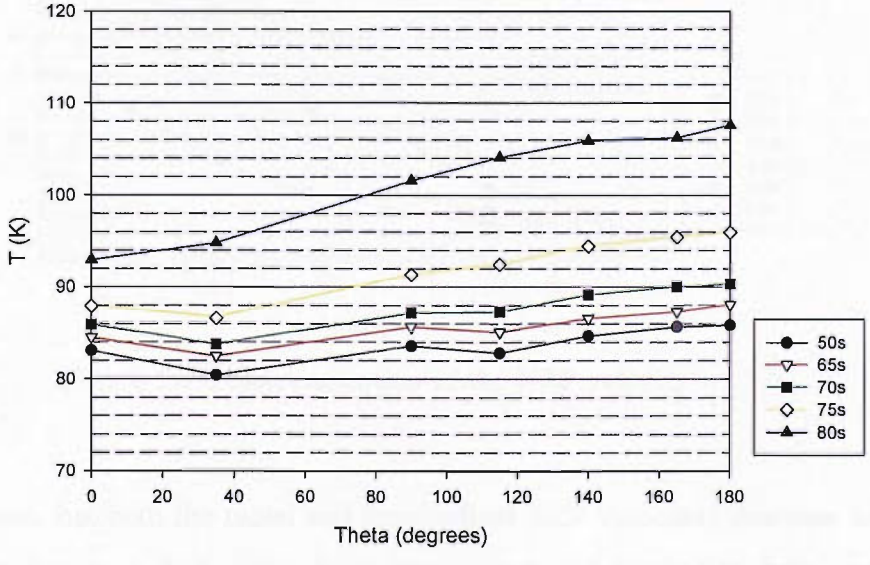

Figure 5.30: Longitudinal temperature profiles during propagation with coil boundaries at 74K. The disturbance is applied over a 125mm section.

5.5.3 Measurement of the NZP velocities

For cases in which normal zone propagation was observed the NZP velocities in the radial and longitudinal directions were calculated. The NZP velocity was calculated by examining the distance at which the propagating temperature front intersects a reference temperature. The average of 4 measured values was used to calculate the NZP velocity, the calculation is shown in Figure 5.31 for the case of NZP in the radial direction. The reference temperature was defined as the maximum point of the normal zone temperature profile that approximates the MPZ. This reference temperature can be easily defined and is part of the temperature profile that represents the boundary between quench and recovery. The NZP velocities in the radial and longitudinal directions as a function of operating temperature are shown in Figure 5.32 and Figure 5.33.

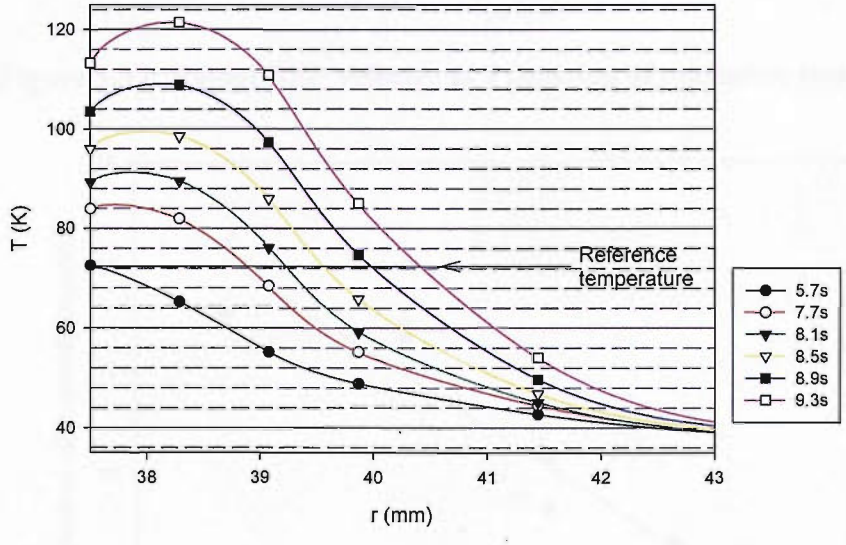

Figure 5.31: Determination of the NZP velocity

It can be seen that both the radial and longitudinal NZP velocities decrease linearly with temperature due to a decreasing operating current and increasing heat capacity. The propagation velocities measured are in the order of mm/s and are therefore similar to those measured by other authors as detailed in section 2.10.

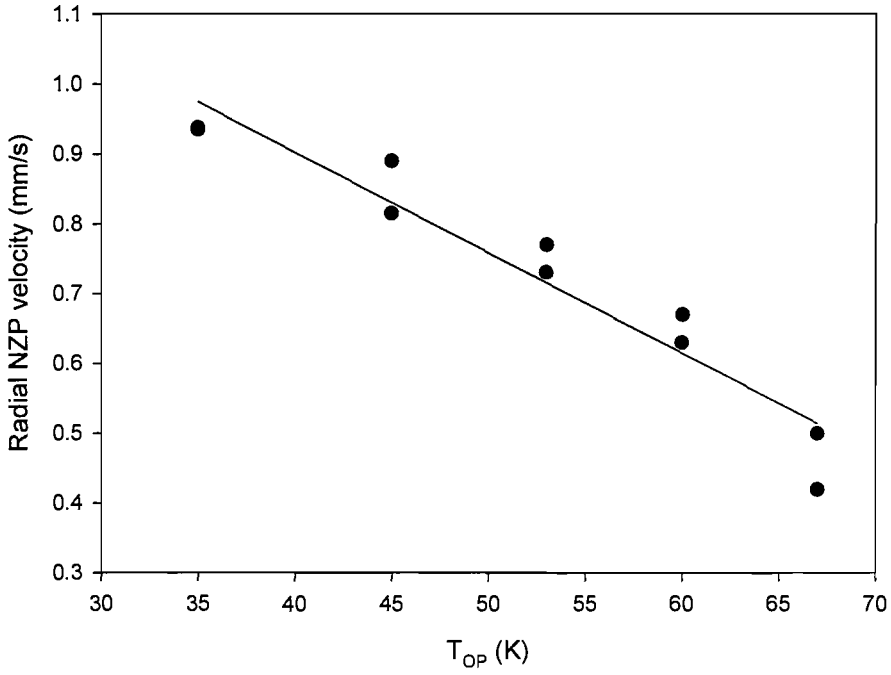

Figure 5.32: Radial NZP velocity as a function of operating temperature

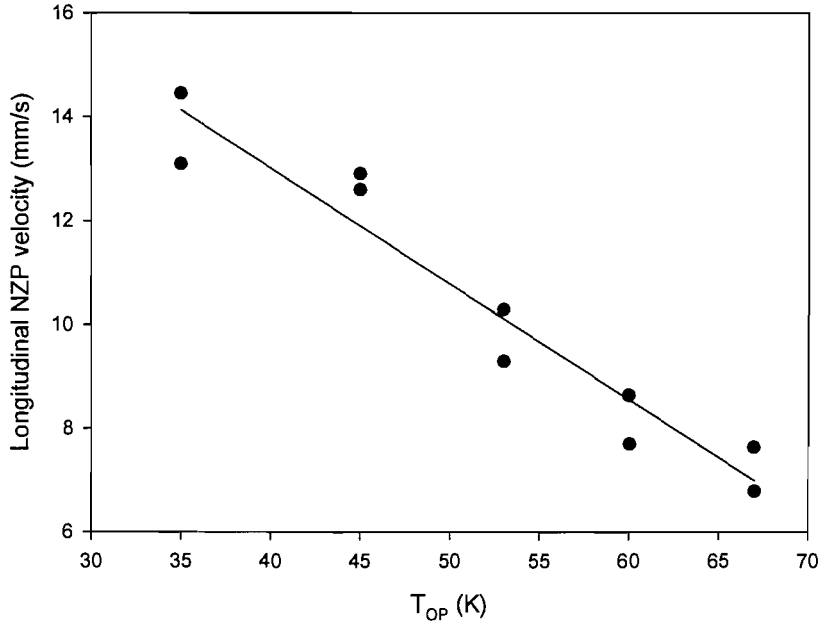

Figure 5.33: Longitudinal NZP velocity as a function of operating temperature

5.5.4 Prediction of the NZP velocities

The NZP velocities in the radial and longitudinal directions are calculated using Equation 2.10 and 2.11 respectively. The formulation of these equations and nomenclature was detailed in section 2.7. The predicted and measured NZP velocities are compared in Figure 5.34. It can be seen that the predicted NZP radial velocity is approximately 50% higher than measured and the predicted NZP longitudinal velocity is approximately 300% higher than measured. It is thought the larger difference in the longitudinal NZP velocity arises because the approximation of a step heat generation is less accurate to use because of the wide current sharing regime. The radial NZP velocity is governed by the thermal conductivity of the insulation rather than the heat generation characteristics. The approximation of a step heat generation has a smaller influence on the predicted radial velocity and therefore a more accurate prediction is obtained. The difference between the measured and predicted radial NZP velocity may be due to simplifications made in the formulation of Equation 2.11 and errors in modelling the resistivity of the stabilising sheath as discussed in 5.4.2.

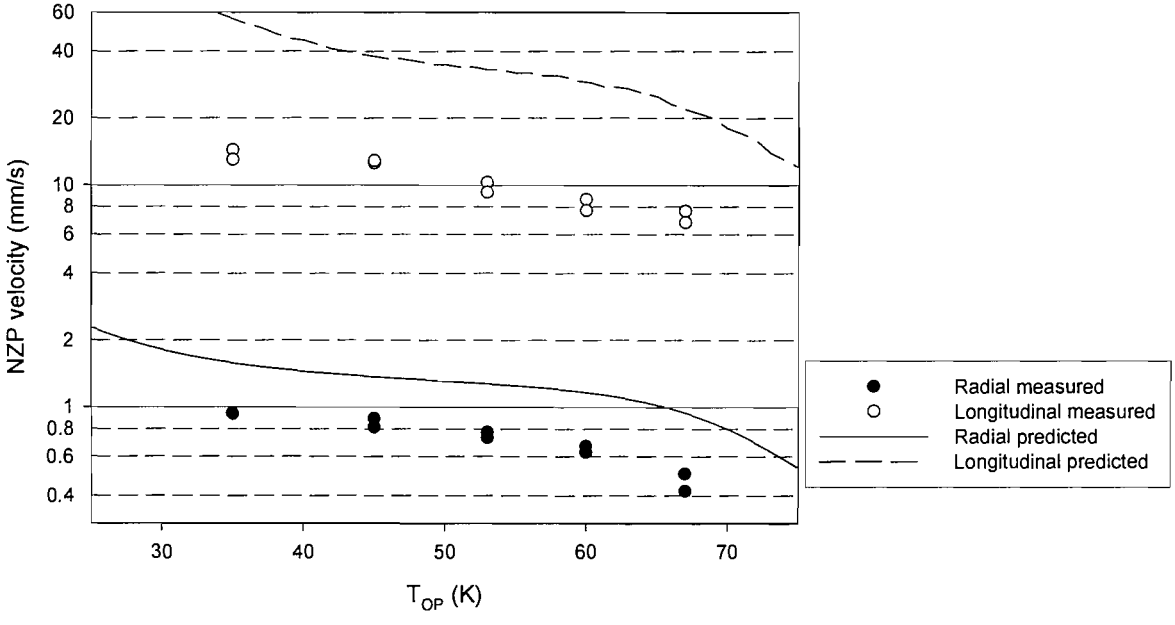

Figure 5.34: Comparison of predicted and measured NZP velocities

5.6 Relevance to protection systems

Quench heaters are often used as parts of a protection system to artificially propagate a quench detected in one coil to the other coils in a magnet. If quench heaters are to be implemented on a HTS magnet then localisation of the temperature distribution may occur around the heater leading to coil damage. It may be necessary to apply multiple quench heaters to each coil or to accurately control the power fed into the heaters to ensure the quench develops without temperature localisation. It has also been observed that the temperature localisation is highly dependent on the operating temperature and length of the heater. These parameters must be accounted for by the protection system to ensure safe operation of the magnet.

5.7 Conclusion

The formation and propagation of normal zones in a conduction cooled (BiPb)2223 Ag alloy sheathed pancake coil has been investigated. A method of determining the temperature profile of a MPZ was proposed. The temperature profiles of the normal zones that approximate the MPZ were measured as a function of both operating temperature and disturbance length. The temperature dependence of the heat generated by the conductor and the thermal properties of both the conductor and insulation were shown to affect the shape of the temperature profiles. The quench energy was measured as a function of operating temperature and disturbance length. It was observed that a minimum value of the quench energy exists between 35K and 60K and that above 60K the quench energy rapidly increases. This was attributed to a sharp increase in Ag thermal conductivity below 60K that counteracts the effect of a decreasing heat capacity. The effects of radial and longitudinal boundaries on the propagating temperature profiles were measured. The normal zone propagation velocity was measured for cases in which the boundaries did not interact with the propagating normal zone. When the normal zone was constrained in both radial and longitudinal directions it was observed that the quench progressed due to a process of general heating.

5.8 References

[1]Martinelli, A.P., Wipf, S.L., ***Proc. 1972 Appl. Supercond. Conf.***, IEEE P u b l . No.72CH0682-5-TABSC, pp. 331-340

[2] Wilson, M.N., Iwasa, Y., ***Cryogenics***, 1978, vol. 18, pp. 17-25

[3] Lue, J.W., Lubell, M.S., Aized, D., Campbell, J.M., Schwall, R.E., ***Cryogenics***, 1996, vol. 36, pp. 379-389

[4]Penny, M., Beduz, C., Yang, Y., Manton, S., Wroe, R., ***Applied-Superconductivity-1997-Proceedings-of-EUCAS-1997***, 1997, vol.2, pp.1551-1554

[5] Wilson, M.N., **Superconducting magnets**, Oxford University press, 1983

[6] Iwasa, Y., **Case studies in superconducting magnets, design and operational issues**, Plenum Press, 1994

Chapter 6 : Finite Element Modelling of Thermal Stability and Quench Propagation in a (BiPb)2223 Pancake Coil

6.1 Introduction

The current sharing regime in HTS spans a wide temperature range over which the heat generated by the conductor has a highly non-linear variation with temperature. In addition the thermal properties of the conductor change significantly over the temperature range that current sharing occurs. Numerical methods are therefore required to accurately simulate the thermal stability and quench propagation in HTS. Various workers have successfully used both the finite difference method [1] and finite element method [2,3] to simulate quench propagation in HTS conductors and coils. This work is based around the ability of the ANSYS® finite element software to allocate a non-linear temperature dependent heat generation and thermal property values to model elements. An emphasis is placed on developing a basis for an analysis tool that could be used by HTS magnet engineers. The thermal stability of a pancake coil wound with (BiPb)2223 tape, as fabricated and tested in Chapter 4 and 5, was analysed. Simulated results are compared with experimental results by examining the normal zone temperature profiles and comparing the simulated and measured temperature dependence of the quench energy.

6.2 Model construction

6.2.1 Analysis approach

A continuum modelling approach [3,4] was used to simplify the analysis by replacing the composite structure of the winding with a homogenized medium. The medium is allocated thermal property values that are averaged over the entire composite structure of the coil. This approach reduces the number of elements in the model and therefore leads to a reduction in solution time which is important when iteratively determining the minimum quench energy (MQE). In the temperature range of interest the continuum model has been

shown to produce similar results to a coil geometry in which the conductor and insulation are modelled separately [5]. The coil construction and conductor type to be modelled are shown in Table 6.1. So that simulation results can be compared to experimental results the coil construction represents the coil that was fabricated and tested in Chapters 4 and 5. All simulation operations were controlled with a parameter based macro using the ANSYS programming language. It is therefore simple to extend the analysis to different sized coils by changing the input parameters and running the simulation.

Item	Specifications
Insulation	Fibreglass cloth ~100μm
Number of turns	38
Coil inner diameter	60mm
Coil outer diameter	90mm
Conductor type	NST multifilamentary (BiPb)2223 tape
Conductor sheath	Outer 0.1MgNi-Ag alloy Inter-filaments: Ag
SC filling factor	27%
Tape dimensions	4.1mm x 0.25mm
I_C	60A at 77K (1μV/cm)
Heater	Constantan tape, up to 200mm x 2mm x 0.15mm

Table 6.1: Coil characteristics

6.2.2 Coil geometry

The coil geometry, as detailed in Table 6.1, is modelled as three concentric 2-dimensional annuli representing the inner turns, outer turns, and the middle turn at which a quench was initiated. A mesh was created using the 8 node element PLANE 77 by constraining the elements to every 1° around the inner and outer perimeters of the coil. A mesh with finer elements, as shown in Figure 6.1, was implemented around the middle turn to allow for accurate application of the heat pulse. All meshing operations were conducted using a cylindrical co-ordinate system to enable the use of anisotropic thermal conductivities in the longitudinal and radial directions.

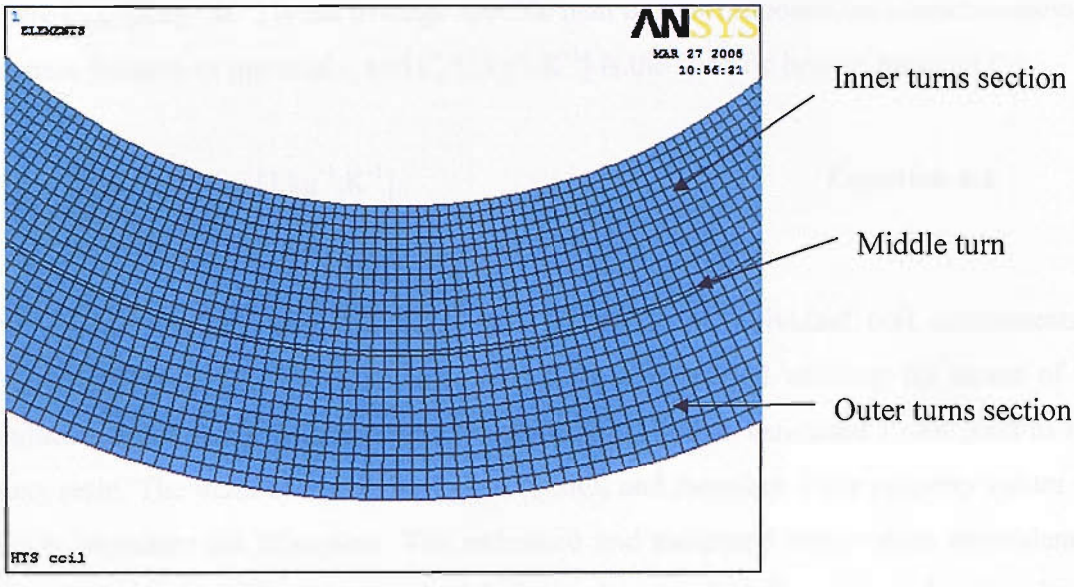

Figure 6.1: Detail of the meshed coil geometry

6.3 Thermal property measurement and estimation

6.3.1 Thermal property measurements

Test samples were removed from a coil fabricated using the same winding parameters and materials as the coil under investigation. A cross-section of the coil was removed and two samples prepared for radial thermal conductivity and heat capacity measurements using a Physical Properties Measurement System (PPMS) supplied by Quantum Design. The thermal conductivity sample was 8mm long and had a cross-sectional area of 5mm^2. The sample for specific heat measurements had a mass of 30mg. The measured properties are presented below by comparing them to estimated property values. Thermal and electrical properties of the conductor and composite structure have been introduced in section 1.5.3. The same data was used to represent the homogeneous material properties of the model coil and will be further discussed in the following sections.

6.3.2 Specific heat estimation

The specific heat of the homogenized coil composite structure can be estimated from the specific heats of the individual components of the coil [6,3] as represented by Equation 6.1.

Where C_{pav} [J.kg^{-1}.K^{-1}] is the average specific heat of the composite, m_i [dimensionless] is the mass fraction of material i, and C_i [J.kg^{-1}.K^{-1}] is the specific heat of material i.

$$C_{par} = \sum_i m_i C_i \qquad [\text{J.kg}^{-1}.\text{K}^{-1}] \qquad \textbf{Equation 6.1}$$

The volume fractions and calculated mass fractions of individual coil components are detailed in Table 6.2. They are calculated from a measured winding fill factor of 63% conductor, a conductor fill factor of 27% (BiPb)2223 and an estimated 1 part glass to 1 part epoxy resin. The main component of glass is SiO_2 and therefore these property values were used to represent the fibreglass. The estimated and measured temperature dependence of the specific heat is shown in Figure 6.2. It can be seen that the estimated values broadly agree with the measured values indicating that the specific heat could be predicted for coils wound with a different conductor or filling factor.

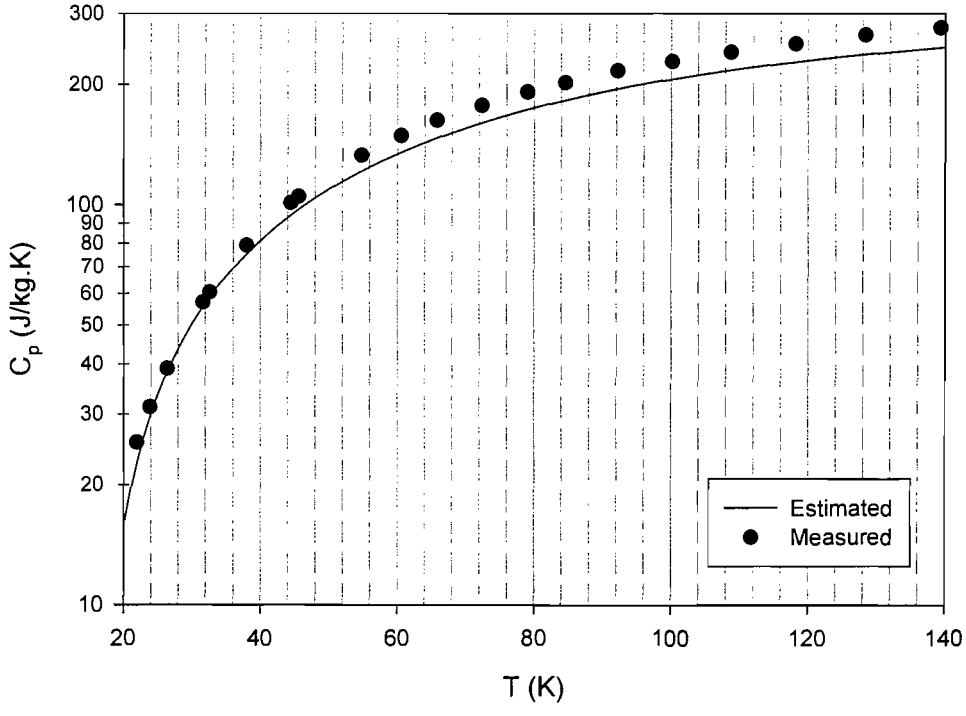

Figure 6.2: Specific heat of the coil composite

Component	Volume fraction	Mass fraction [7,8]
Fibreglass [9]	0.37 x 0.5 =0.185	0.12
Epoxy resin [10]	0.37 x 0.5 =0.185	0.01
Silver [11]	0.63 x 0.73 =0.46	0.76
(BiPb)2223 [12]	0.63 x 0.27 = 0.17	0.11

Table 6.2: Components of the coil composite

6.3.3 Thermal conductivities

The homogenized medium is allocated anisotropic thermal conductivities to represent the composite coil structure. The radial thermal conductivity is difficult to estimate in a composite material because it depends on accurately representing the thermal contact resistances and geometric distribution of the separate composite components [3,6]. It was therefore decided to rely solely on the measured radial thermal conductivity data, as shown in Figure 6.3. A typical value for the thermal conductivity of resin impregnated fibreglass is 0.35 W/m.K at 77K [13]. Hence it can be seen that the radial thermal conductivity is governed by the poor thermal conductivity of the fibreglass and epoxy resin. The longitudinal thermal conductivity of the conductor was obtained from published measurements for the specific conductor used [14] as shown in Figure 6.4.

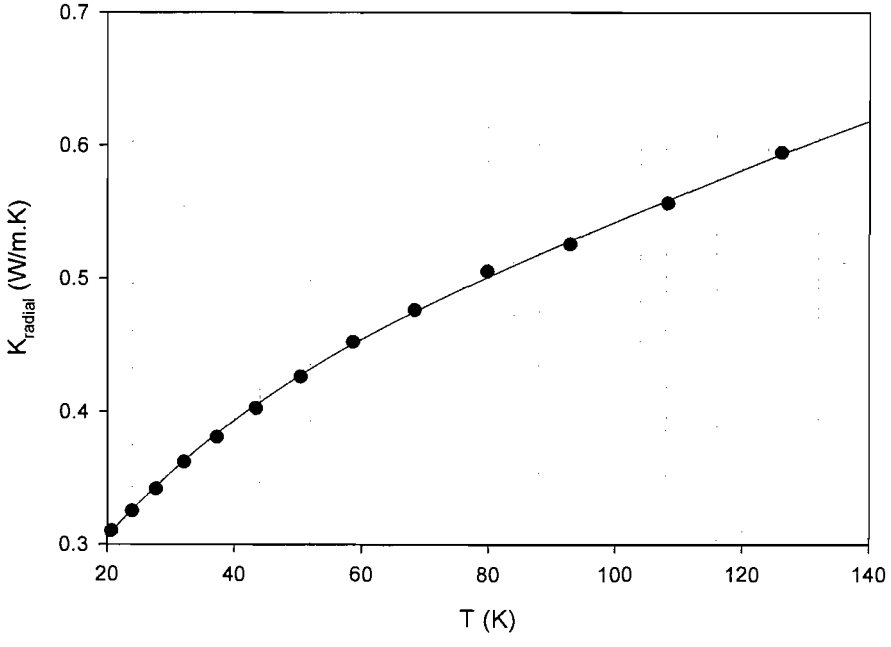

Figure 6.3: Measured radial thermal conductivity of the coil composite

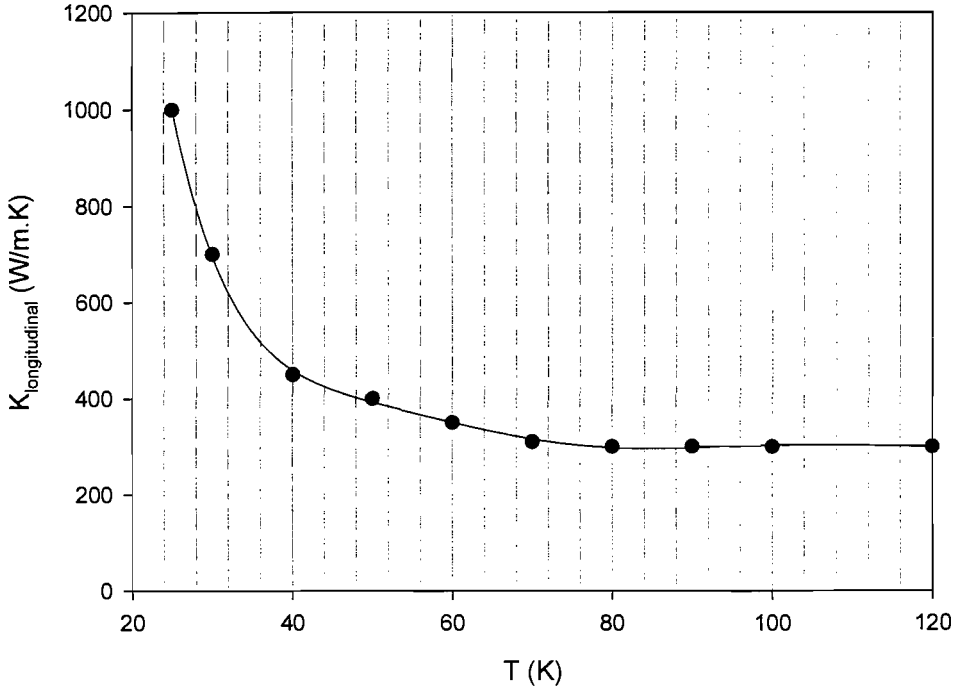

Figure 6.4: Longitudinal thermal conductivity of the NST 'Zerome Hercules' Ag-Mg-Ni sheathed conductor [14]

6.4 Boundary conditions and loading

6.4.1 Boundary conditions

The temperature variation across the conductor width is neglected and adiabatic boundaries are applied on the top and bottom surfaces of the model coil simulating heat transfer characteristics in the experimental coil. A constant temperature was applied to the inner and outer boundaries. It is thought this is a valid assumption because the temperature of the coil boundaries stayed relatively constant during a quench, as observed from experimental measurements in Chapter 5.

6.4.2 Heat generation in a superconducting composite

The heat generated by the conductor was calculated as a function of temperature using the power law approximation accounting for current sharing to the stabilising matrix as shown

in Equation 6.2. Where I_{OP} [A] is the operating current density, $I_C(T)$ [A] is the temperature dependent critical current density of the superconductor, E [V.m^{-1}] is the electric field across the conductor, E_C [V.m^{-1}] is the electric field at the critical current (1μV/cm), $n(T)$ [dimensionless] is the temperature dependent n-value from the power law, ρ_m [Ω.m] is the resistivity of the stabilising matrix, and A_m [m^2] is the area of the stabilising matrix. This heat generation formulation, Equation 6.2, is described in detail in section 2.7. The data for the resistivity of the stabilising matrix is presented in section 1.5.3.

$$I_{op} = \left(\frac{E}{E_c}\right)^{\frac{1}{n(T)}} \cdot I_c(T) + \frac{E}{\rho_m(T)} \cdot A_m \quad [\mathrm{A}] \qquad \textbf{Equation 6.2}$$

The n-value used in the calculations exhibited approximately linear temperature dependence from 16 at 77K to 28 at 20K [15]. The magnetic field generated by the coil was assumed to remain constant during a quench and therefore the $I_C(T)$ dependence was obtained from measurements of the critical current between ends of the test coil as presented in Section 4.6. The measured critical current was observed to decrease linearly from 158.5A at 35K to 43.5A at 74K. The resistivity of the stabilising matrix was considered as Ag with a residual resistivity ratio (RRR) of 100 [11] as presented in section 1.5.3. The resistivity rapidly increases from 3.5×10^{-10}Ω.m at 30K to 2.5×10^{-9}Ω.m at 70K.

For each simulation the current was set at a value near I_C that was found experimentally to give an average electric field across the coil of 0.7μV/cm at that operating temperature. Equation 6.2 was solved to obtain the volumetric heat generation, as given by the product of E and the operational current density, J_{OP} [A.m^{-2}]. Heat generation was averaged over the winding volume by multiplying the volumetric heat generation of the conductor by a winding fill factor, λ_w=0.63. The calculated volumetric heat generations at varying operating temperatures is shown in Figure 6.5. For each separate simulation the heat generation as a function of temperature is automatically read into the analysis software and applied to individual model nodes.

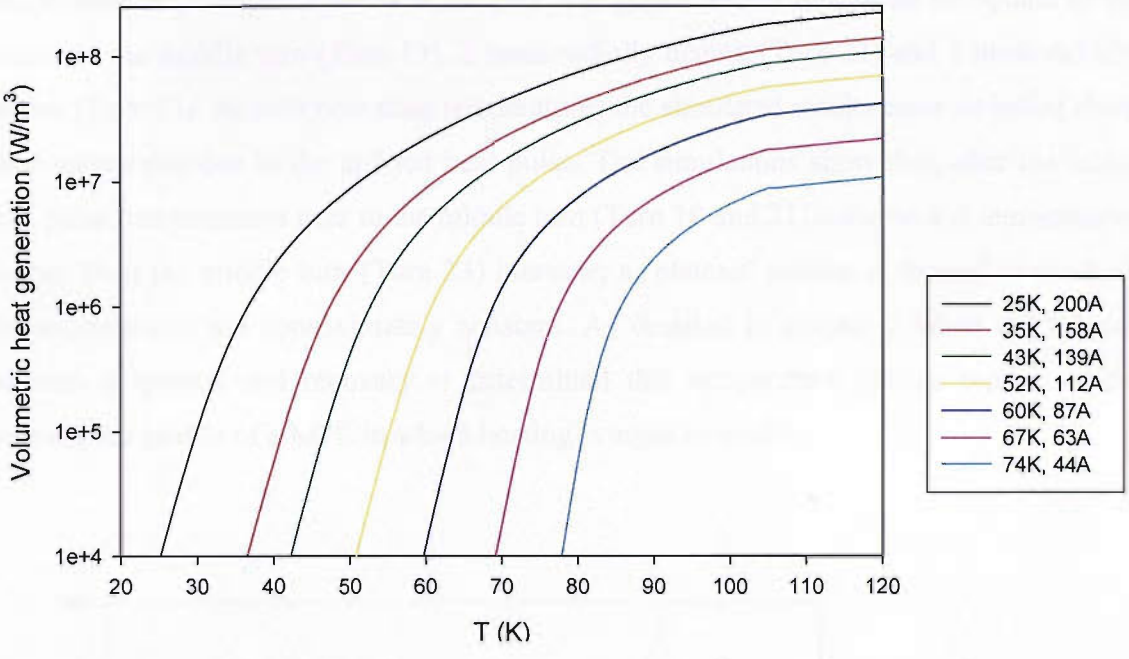

Figure 6.5: Coil volumetric heat generation for various operating temperatures with I~I_C

6.4.3 Solution

The coil boundaries were set at a constant temperature and a quench was initiated by applying a pulse of 1s duration to a set of elements 0.25mm wide representing the middle turn. The transient analysis was solved using the automatic time stepping method to aid convergence. A simulation 20s in length took approximately 300s to solve using a PC with a Pentium 4 2.4GHz processor.

6.5 Normal zone formation and propagation

6.5.1 Transient temperature response to a heat pulse

Figure 6.6 and Figure 6.7 show two separate simulations in which the coil boundaries were set to 67K and 35K respectively and a quench initiated by applying a heat pulse to a 25mm long section of the middle turn. The energy applied was just sufficient to initiate a quench and therefore the coil recovered when a heat pulse of a smaller magnitude was applied.

Shown in both Figure 6.6 and Figure 6.7 are the experimental and simulated transient temperature response of 3 points in the coil. The points are located at the mid-plane of the heater on the middle turn (Turn 19), 2 turns radially distant (Turn 21) and 4 turns radially distant (Turn 23). At both operating temperatures the simulated results show an initial sharp temperature rise due to the applied heat pulse. The simulations show that, after the initial heat pulse, temperatures near to the middle turn (Turn 19 and 21) collapse and temperatures further from the middle turn (Turn 23) increase; a 'plateau' section is formed over which the temperatures are approximately constant. As detailed in chapter 5 when the balance between a quench and recovery is determined this temperature plateau represents the temperature profile of a MPZ in which heating is equal to cooling.

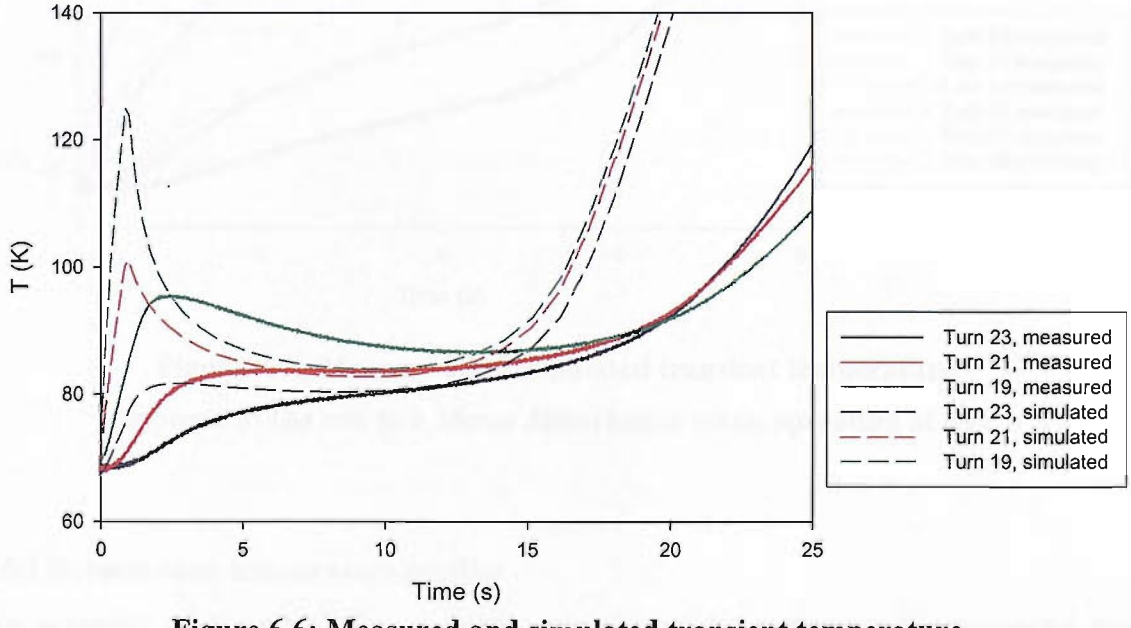

Figure 6.6: Measured and simulated transient temperature response of the coil to a 25mm disturbance when operating at 67K

The experimental temperature traces show a similar trend to the simulated results with a temperature plateau being formed that then propagates. However, the initial sharp temperature rise is not observed in the measured results. As explained in Chapter 5, it is thought this 'damping' effect is caused by the method of temperature measurement. Small

copper cold fingers soldered to the coil to aid assembly introduce an additional thermal diffusion path between the tape and point of measurement causing the observed damping effect. The rate at which temperatures increase during propagation is greater for the simulated results than for the measured results indicating that the volumetric heat generation applied to the modelled coil is larger than that produced in the experimental coil.

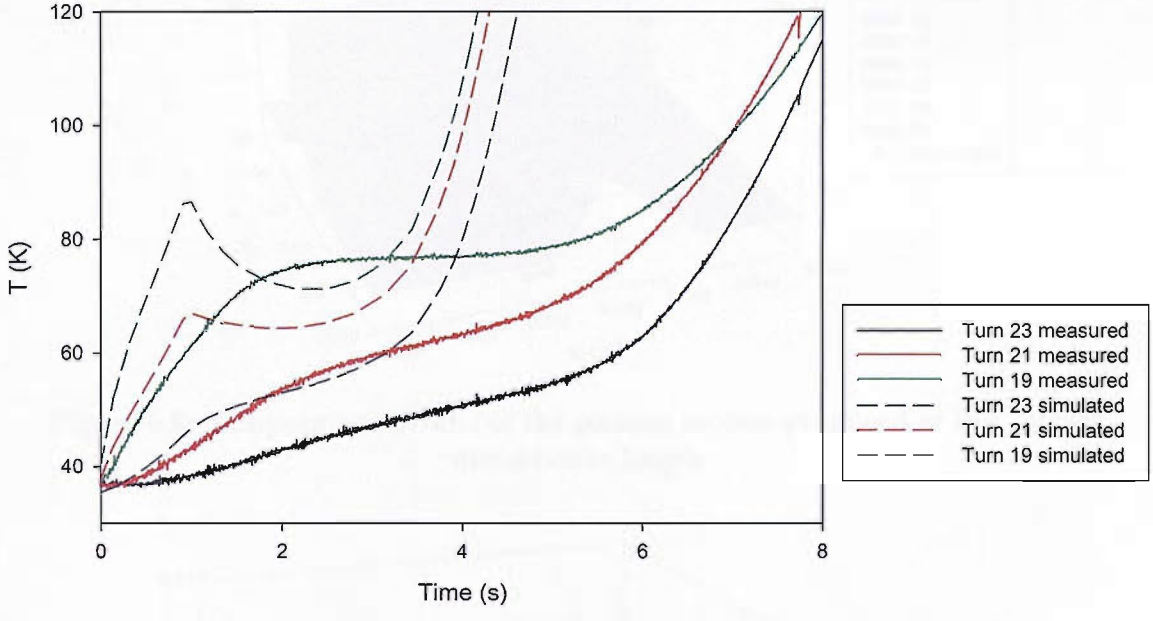

Figure 6.7: Measured and simulated transient temperature response of the coil to a 25mm disturbance when operating at 35K

6.5.2 Normal zone temperature profiles

The accuracy of the simulation is further investigated by comparing the measured and simulated normal zone temperature profiles. The temperature profiles that approximate the MPZ temperature profiles produced during the plateau section are compared in Figure 6.8 and Figure 6.9 for operating temperatures of 35K and 67K respectively. A section of the coil is presented to allow observation of the radial temperature profile.

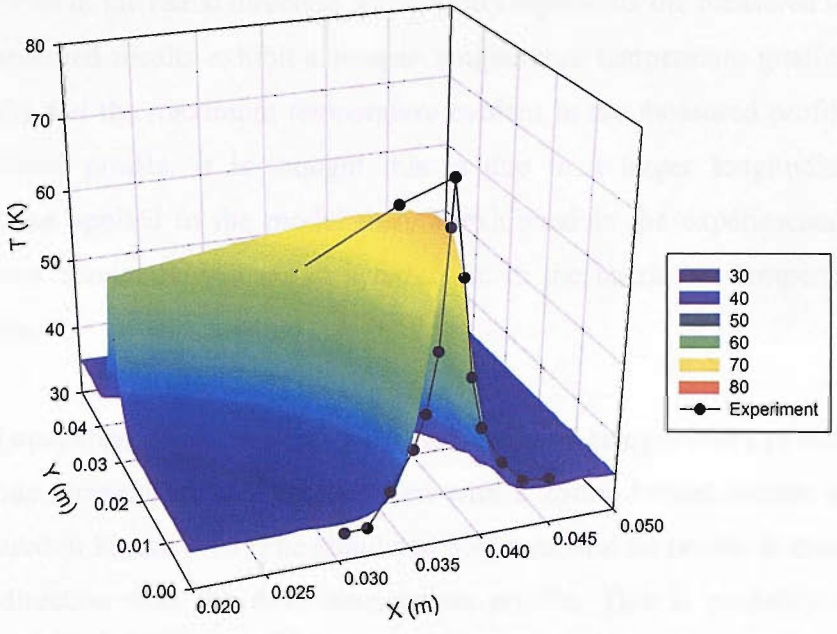

Figure 6.8: Temperature profile of the plateau section produced at 35K, 25mm disturbance length

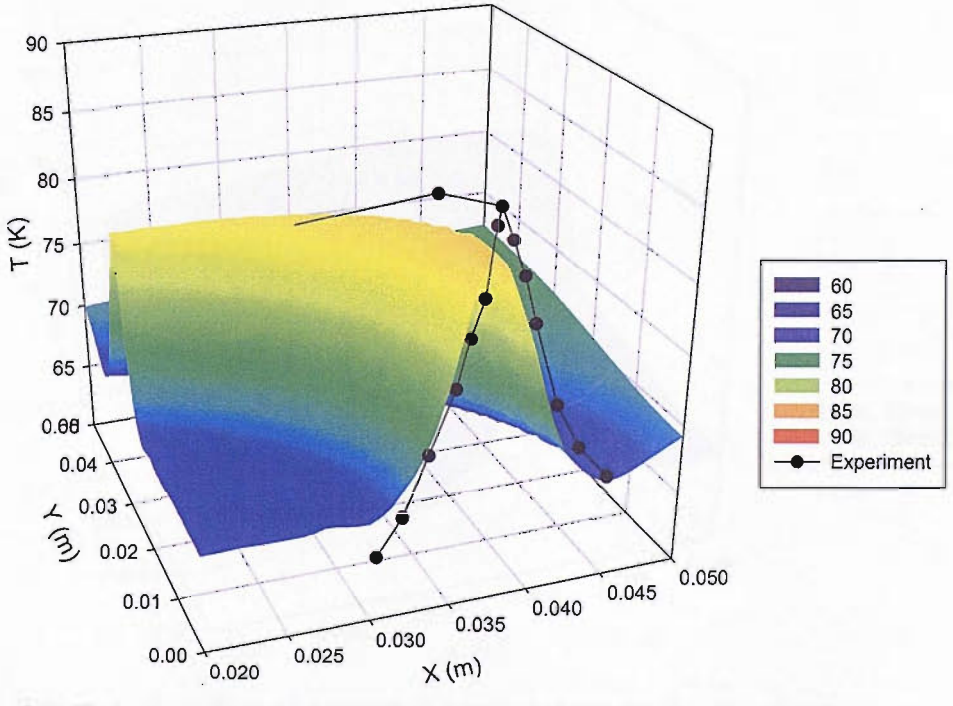

Figure 6.9: Temperature profile of the plateau section produced at 67K, 25mm disturbance length

It can be seen that at both operating temperatures the shape of the simulated normal zone temperature profile in the radial direction successfully represents the measured temperature profile. The measured results exhibit a steeper longitudinal temperature gradient than the simulated results and the maximum temperature evident in the measured profile is higher than the simulated profile. It is thought this is due to a larger longitudinal thermal conductivity value applied to the model than is exhibited in the experimental coil. The increased thermal conductivity leads to a reduction in the maximum temperature of the simulated results.

6.5.3 Effect of operating temperature on the normal zone temperature profiles

The normal zone temperature profiles obtained with a 25mm heated section at 35K and 67K are compared in Figure 6.10. The simulated 35K temperature profile is more localised in the radial direction than the 67K temperature profile. This is probably due to the decreased radial thermal conductivity of the coil composite at lower temperatures. At 67K a

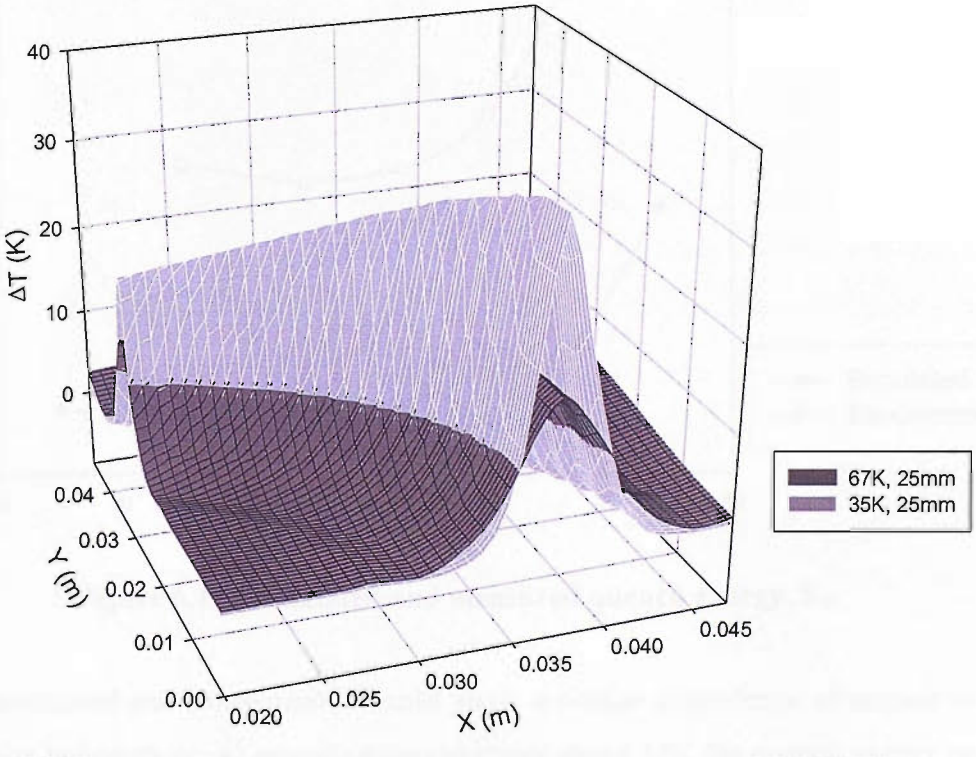

Figure 6.10: Effect of operating temperature on the temperature profile of the plateau

maximum temperature rise of 17K is obtained compared to a 36K temperature rise at 35K. A higher temperature can be maintained at 35K due to the increased cooling in the longitudinal direction balancing the higher volumetric heat generation.

6.6 Stability simulations

Separate quench events were simulated at a desired operating temperature to determine the quench energy, E_Q. The magnitude of the applied disturbance was successively increased until the quench energy was reached and subsequently it was identified from the simulations that a quench had been initiated. The temperature dependence of the quench energy was determined and the results are compared to experimental measurements in Figure 6.11. All quenches were initiated using a 2.5cm long heated section.

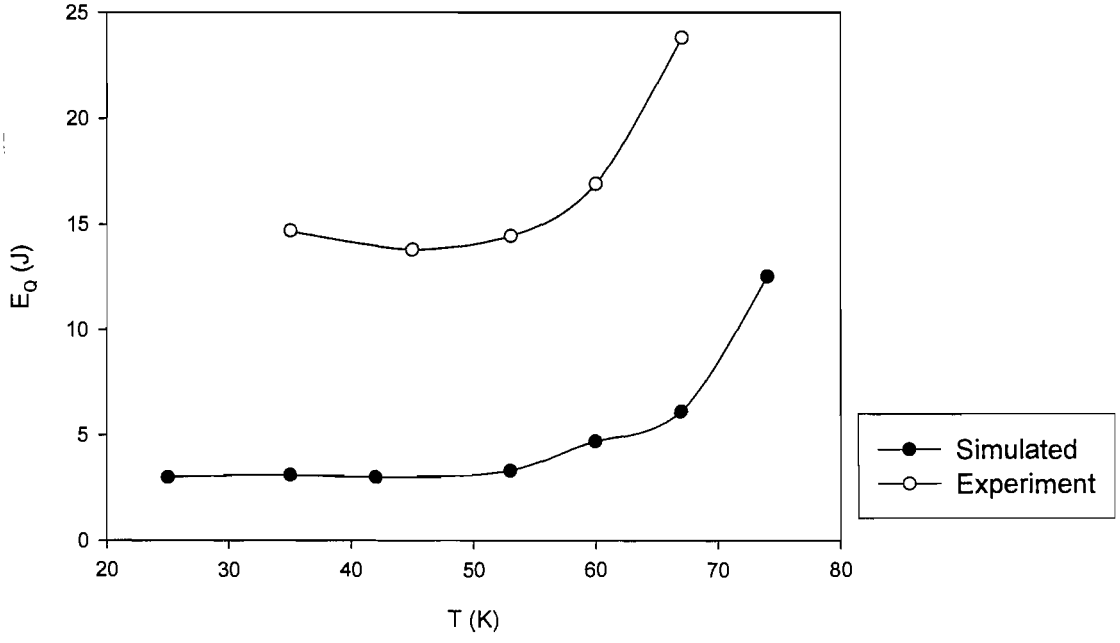

Figure 6.11: Simulated and measured quench energy, E_Q

Both the simulated and experimental results show a similar dependence of quench energy on operating temperature. At operating temperatures above 55K the quench energy rapidly increases as the operating temperature is increased. Below 55K the quench energy appears

to reach a constant value as operating temperature decreases. As detailed in Chapter 5 this is attributed to a sharp increase in Ag thermal conductivity below approximately 60K. This leads to a relatively constant quench energy before the rapid reduction of heat capacity at lower temperatures becomes dominant. The magnitude of the quench energy predicted by the model is different to the experimental measurements by a factor of between 3.6 and 4.7 over the entire temperature range. It is expected that the differences are due to inaccuracies in modelling the volumetric heat generation. The resistivity used in the calculations may be too high thereby increasing the heat generation and reducing the quench energy. In Figure 6.8 and Figure 6.9 the measured and simulated temperature profiles were compared and the simulated temperatures were shown to be lower than the measured temperatures. It is thought that the lower temperatures are produced by a combination of an increased heat generation offset by an increased cooling due to the artificially high longitudinal thermal conductivity.

6.7 Conclusion

A finite element model based on the continuum modelling approach has been constructed to predict the thermal stability of a pancake coil wound with (BiPb)2223 conductor. Simulated transient temperature traces and temperature profiles appear to predict the quench behaviour reasonably successfully. To improve the accuracy of the predictions the parameters of the heat generation calculation, such as the resistivity of the stabilizing sheath and n-value of the superconductor, should be modelled more accurately. The model can be used as a base for future work involving more demanding simulations. Such simulations could involve 3-dimensional thermal stability studies and using the ability of the ANSYS® program to couple thermal and electromagnetic problems so that current decay in the coil during a quench can be accounted for.

6.8 References

[1] Haid, B., Iwasa, Y., Bascunan, J., ***IEEE Transactions on Applied Superconductivity***, 2001, vol. 11, no. 1, pp. 1820-1823

[2] Kim S.B., Ueno, Y., Ishiyama, A., ***IEEE Transactions on*** **Magnetics**, 1996, vol. 32, no. 4, pp. 2822-2825

[3] Lehtonen, J., Mikkonen, R., Paasi, J., ***Superconductor Science and Technology***, 2000, vol. 13, pp. 251-258

[4] Hashin, Z., ***Analysis of Composite Materials - A Survey***, 1983, vol. 50, pp. 481-505

[5] Huang, T., Johnstone, A., Yang, Y., Friend, C., ***Proceedings of ASC 2004***, to be presented in IEEE Transactions on Applied Superconductivity

[6] Lee, Y.,Haji-Sheikh, A., Fletcher, A.S., Peterson, G.P., ***ASME Journal of heat transfer***, 1994, vol.116, p.17-27

[7]**CRC handbook of Chemistry and Physics**, 68th Ed.

[8]**CRC handbook of tables for engineering and applied science**, 2nd Ed.

[9] Bansal, N.P., **Handbook of glass properties**, Academic Press, 1986

[10] Hartwig, G., ***IEEE Transactions on*** **Magnetics**, 1975, vol. 11, no. 2, pp. 536-539

[11] Smith, D.R., Fickett, F.R., ***Journal of Research of the National Institute of Standards and Technology***, 1995, vol. 100, pp. 119

[12] Isaac, J., Philip, J., Sebastian, M.T., Damodaran, A,D., ***Physica C***, 1992, vol. 199, pp. 247-250

[13]Iwasa, Y., **Case studies in superconducting magnets, design and operational issues**, Plenum Press, 1994

[14]Vase, P., Flukiger, R., Leghissa, M., Glowacki, B., ***Superconductor Science and Technology***, 2000, vol. 13, pp. 71-84

[15] Lehtonen, J., Mikkonen, R., Perala, R., ***Proceedings of the International Cryogenic Materials Conference***, May 25-28, 2003, Enschede, Netherlands, 2004

Chapter 7 : Conclusions and further work

The formation and propagation of normal zones in a conduction cooled (BiPb)2223 Ag alloy sheathed pancake coil has been investigated both experimentally and through simulation. The work has relevance for the magnet designer when examining the thermal stability of HTS magnets and when designing the protection systems that should be implemented for safe operation of such magnets.

Apparatus was designed and manufactured to provide stable operating conditions for a HTS pancake coil over a wide temperature range. Both resistive and HTS current leads were used to supply current to the coil. To maintain the temperature of the pancake coil heat is removed from the coil boundaries to the coldhead of a cryocooler through conduction along thermal links. The apparatus was tested up to a maximum operating current of 300A at which only a 0.7K drift in the coldhead temperature was observed. A large temperature difference of between 11K and 18K was observed between the coil boundaries and coldhead dependent on operating temperature. It is thought that the bolted joints and the electrically isolated clamp caused the majority of the temperature drop. The minimum temperature achievable of 35K still allowed successful operation of the HTS pancake coil. This is because HTS can operate over a wide operating range and therefore conduction cooled HTS magnets exhibit a high tolerance to temperature differences that can occur across thermal links.

A conduction cooled pancake coil wound with a (BiPb)2223 tape conductor was manufactured using a vacuum impregnation process. Miniature copper cold fingers were soldered to the conductor during coil winding. Thermocouples could be soldered to the cold fingers after epoxy impregnation therefore simplifying coil fabrication and installation. The copper coldfingers introduce an additional thermal diffusion path between the conductor and point of measurement causing a slight delay in the dynamic response of the temperature measurement. Further work could build on the results already obtained and examine soldering the thermocouples directly to the coil to improve the dynamic response of the temperature measurement.

The highly instrumented coil was characterised by measuring the current-voltage curves and the overcurrent at which a quench occurs as a function of operating temperature. The critical current of the coil was determined from the measured current-voltage curves and a procedure presented to predict the critical current as a function of operating temperature. The work presented is of use to the HTS magnet designer when developing conduction cooled HTS magnets. When generating concepts for HTS magnets the critical current and quench current can be estimated before detailed design work commences.

One example of where a HTS coil may be subjected to an overcurrent is when used as a high field insert in a LTS magnet. When the less stable LTS sections quench the magnetic coupling between coils can induce overcurrents in both the LTS and HTS sections. The temperature and voltage distributions in the pancake coil were mapped during the evolution of a quench caused by an overcurrent. It was observed that the quench initially evolves due to a steady heating of the entire coil, although, localisation of the temperature distribution occurs as heating rates increase due to insufficient time for heat diffusion. A protection system for such an HTS coil would ideally detect the slow general voltage rise, perhaps using an active voltage detection system, and reduce the current in the coil before the rapid temperature rise occurred.

The quench energy of the pancake coil was measured as a function of operating temperature by applying transient disturbances of various lengths. It was observed that the quench energy remains relatively constant between 35K and 60K and that above 60K the quench energy rapidly increases. This was attributed to a sharp increase in Ag thermal conductivity below 60K that counteracts the effect of a decreasing heat capacity. In practical terms this means that the stability to transient disturbances is not affected by varying the temperature between 35K and 60K. It was predicted that at temperatures below 60K the maximum quench energy occurs at the temperature where the thermal conductivity is maximum. This occurs at approximately 25K for the coil tested. To verify the predictions further work should concentrate on measuring the quench energy of a similar coil at lower temperatures. This could be achieved by replacing the single stage cryocooler with a two stage cryocooler that can provide a minimum temperature of approximately 4K. Further

work could also examine using conductors with sheaths of various thermal conductivities to wind separate pancake coils. The temperature dependent quench energy of each coil could be determined and related to the thermal conductivity of the sheath material.

The large number of thermocouples and voltage taps applied to the coil allowed the temperature and voltage profiles to be mapped during the evolution of a quench. The temperature profiles of the normal zones that approximate the MPZ were measured as a function of both operating temperature and disturbance length. The temperature profiles demonstrate the spatial size and maximum temperature of disturbances to which the winding is stable which can then be used to predict the stability of the coil.

The effects of radial and longitudinal boundaries on the temperature profiles of a propagating normal zone were measured. When the normal zone was constrained in both radial and longitudinal directions it was observed that the quench progressed due to a global temperature rise. The NZP velocity was measured for cases in which the boundaries did not interact with the propagating normal zone. The slow NZP velocities measured, in the order of mm/s, present challenges when designing protection systems for HTS magnets. Due to the slowly propagating normal zone the voltages generated can be low and therefore sensitive detection circuits are needed for quench detection. If quench heaters are used to artificially propagate a quench the number of heaters, placement of heaters and heater input power must be carefully chosen so as not to produce temperature localisation around the quench heaters.

A finite element model based on the continuum modelling approach has been constructed to predict the thermal stability of a pancake coil wound with (BiPb)2223 conductor. Simulated transient temperature traces and temperature profiles appear to predict the experimentally measured quench behaviour reasonably successfully. To improve the accuracy of the predictions the resistivity of the stabilizing sheath should be modelled more accurately. Further work could extend the basic model by using the ability of the ANSYS® program to couple thermal and electromagnetic problems to model current decay in the coil.